

70156
20156
70156
70156

2156
2156
TR3156

Experiments on a natural circulation loop -
from void-fraction to coupled nuclear
thermal-hydraulic dynamics

H.V. Kok



The research described in this thesis has been performed at the Reactor Physics Department of the Interfaculty Reactor Institute (IRI), Delft University of Technology, Mekelweg 15, 2629 JB Delft, The Netherlands.

This research was supported by the PINK-2 program of the Ministry of Economic Affairs, by the European Union within its Euratom Research Framework Program 1994-1998 and by the GKN Nuclear Power Plant, P.O. Box 40, 6669 ZG Dodewaard, The Netherlands.

**Experiments on a natural circulation loop -
from void-fraction to coupled nuclear
thermal-hydraulic dynamics**

Proefschrift



ter verkrijging van de graad van doctor
aan de Technische Universiteit Delft,
op gezag van de Rector Magnificus prof. ir. K.F. Wakker,
in het openbaar te verdedigen ten overstaan van een commissie,
door het College voor Promoties aangewezen,

op dinsdag 16 juni 1998 te 10:30 uur
door

Haico Victor KOK

natuurkundig ingenieur
geboren te Beloit (Verenigde Staten van Amerika)

Dit proefschrift is goedgekeurd door de promotor:

Prof. dr. ir. H. van Dam

Samenstelling promotiecommissie:

Rector Magnificus, voorzitter

Prof. dr. ir. H. van Dam, Technische Universiteit Delft, promotor

Dr. ir. T.H.J.J. van der Hagen, Technische Universiteit Delft, toegevoegd promotor

Prof. dr. ir. H.E.A. van den Akker, Technische Universiteit Delft

Prof. dr. ir. A. van den Bos, Technische Universiteit Delft

Prof. ir. O.H. Bosgra, Technische Universiteit Delft

Dr. R.F. Mudde, Technische Universiteit Delft

Dr. F. Inada, Central Research Institute of Electric Power Industry, Japan

Published and distributed by:

Delft University Press

Mekelweg 4

2628 CD Delft

The Netherlands

Telephone: +31 15 2783254

TeleFax: +31 15 2781661

E-mail: DUP@DUP.TUDelft.NL

ISBN: 90-407-1711-7 / CIP

Copyright 1998 by Haico Victor Kok

All rights reserved. No part of the material protected by this copyright notice may be reproduced or utilized in any form or by any means, electronic or mechanical, including photocopying, recording or by any information storage and retrieval system, without written permission from the publisher: Delft University Press.

Printed in The Netherlands

Table of Contents

I.	Introduction	
1.1	The need for new reactor designs	1
1.2	Outline of this thesis	7
II.	The DESIRE facility	
2.1	The foundations of the DESIRE facility	9
2.2	Concepts of two-phase flow	10
2.3	Scaling analysis	13
2.4	Description of the DESIRE facility	17
2.5	Instrumentation	21
III.	Subchannel void-fraction measurements	
3.1	Measurement technique	23
3.2	The measurement set-up	31
3.3	Two-phase flow models	37
3.4	Void-fraction measurements in the assembly	40
3.5	Void-fraction measurements in riser and downcomer	51
3.6	Conclusions	53
IV.	Steady-state behavior of natural circulation	
4.1	Static flow model - overview	55
4.2	Static flow model - description	58
4.3	Comparison of model to measurements	67
4.4	Conclusions	70
V.	Modeling the dynamics	
5.1	Types of instability	71
5.2	Simplified analytical model of the dynamics	72
5.3	Feedback simulation in DESIRE	83
5.4	Conclusions	97
VI.	Experimental investigation of the dynamics	
6.1	Noise analysis	99
6.2	Measurements without feedback	101
6.3	Measurements with feedback	112
6.4	Discussion and recommendations for improvement	120
6.5	Conclusions	122

VII. General conclusions and discussion	
7.1 Conclusions from this work	125
7.2 Recommendations	127
7.3 Concluding remarks	128
Nomenclature	129
References	133
Appendix - Void fraction data	141
Summary	147
Samenvatting	149
Dankwoord	151
Curriculum vitae	153

Chapter 1

Introduction

1.1 The need for new reactor designs

1.1.1 Passive safety features in Nuclear Reactors

If nuclear energy is to be accepted by society then the generation of electricity and heat using nuclear reactors may not pose a risk to the environment. Currently, electricity is generated in large nuclear power plants whose design with respect to safety in the western countries is based on the *defense in depth* strategy. Defense in depth is a concept which builds on the application of several levels of protection, including a number of physical barriers preventing the release of radioactive material into the environment (IAEA, 1988). Examples of such barriers are the fuel material itself, the reactor vessel, the emergency core cooling systems and the containment. The reliability of the physical barriers can be enhanced by applying the concept of defense in depth to them in turn.

The number of barriers and safety systems can become quite large in such a concept, and this in itself becomes a problem. First of all, increasing the number of safety systems can become ineffective: the extra safety gained for any given investment in a safety system decreases with the absolute safety level of the plant. Secondly, more complex systems increase the likelihood of human error, effectively decreasing the safety gained by the extra system. And lastly, it can become impossible to prove that such complex systems actually achieve the safety standards they are designed for. Related to this is the difficulty to demonstrate to the public the safety of such a complex system, preventing public acceptance of nuclear energy.

It is therefore time to take a step backwards and scrutinize the basic design of nuclear reactors. The safety problem is easy to state: the temperature of the fuel must be kept below a certain

value at all times. If this can be achieved the fuel will always remain intact and no radioactive material will be released into the environment. The temperature of the fuel is determined by a heat balance. If the heat production rate in the reactor core is higher than the removal of heat from the core then the temperature of the core will rise. In a nuclear reactor there are two distinct ways this can happen; via a *reactivity excursion* or via a *loss of coolant*. This distinction is made because both types of accidents have different causes and different effects.

During a reactivity excursion accident the reactivity of the nuclear reactor is increased to such an extent that the power produced by the nuclear fission increases exceedingly in a short time period (in the order of seconds). This can severely damage the reactor and lead to a release of radioactive material into the environment. Fortunately, proper reactor design makes this kind of accident physically impossible by utilizing several intrinsic properties of materials. A well-known example is the Doppler-effect, which give the uranium-238 nuclei a higher probability of neutron-capture at higher temperatures removing the neutron from the nuclear chain reaction. In this way the strong increase of power in a reactivity excursion stops itself before any damage to the reactor core is done. Notably, the Chernobyl reactor was not well designed in this respect, which is one of the main causes for the accident (the Chernobyl accident was a reactivity type of accident).

This strategy to make reactivity accidents not just improbable, but to make them *impossible on physical grounds* is used in all western nuclear reactors. Historically a different strategy has been followed to prevent the second type of accident: the loss of cooling or coolant. This is the type of accident which in popular language leads to a 'melt down' of the reactor core. Key element in this type of accident is that even after the nuclear fission chain reaction has been stopped (the reactor is shut down) the nuclear fuel continues producing a large amount of heat caused by the radioactive decay of the fission products. Immediately after shut down of the reactor this so-called decay heat production rate equals approximately 6% of the power that was produced prior to the shutdown of the reactor. It quickly reduces to 1.2% after 1 hour and to 0.6% after 1 day. This decay heat must be removed from the reactor otherwise the temperature will become too high and the fuel will melt. A good rule of thumb is that it takes the evaporation of 1 cubic meter of water for every MWth of reactor power to remove the decay heat during the first week after shut down (so for a typical 3000 MWth reactor 3000 m³ is needed during the first week).

To ensure adequate decay heat removal every reactor has a variety of systems at its disposal, comprising of the primary cooling system, which is used to produce electricity during normal operation, and of a number of safety systems. A characteristic of all these systems is that they are active systems; they require power and/or operator action in order to operate. They can also fail when called upon. These systems require good design, good operator training and good maintenance. The safety level which can be reached this way is very high, but ultimately limited, and it might not be enough to allow nuclear energy to reach its full potential.

On reflection it seems that the strategy of using physical processes to prevent the criticality type of accident was forced upon the designers by the realization that it would be next to

impossible to ensure the safety of a nuclear reactor using other methods (actuators and controlling devices) because these are simply too slow. There were no such problems for the second type of accident, the loss of coolant, because the time scale of this type of accident is much larger (minutes to hours). Therefore other factors influenced the design of the reactors, of which the most important is the economics. Large units benefit from the economy of scale, so it was thought that reactors with a high power density would be the most cost-efficient. Unfortunately this just about excludes the possibility of using passive systems for decay heat removal from the core, which is why active systems were adopted. It is now realized that all these active safety systems have become so expensive that the original economic argument for cores with a high power density is not so clear-cut as it used to be. This has opened the way for research into new and innovative reactor designs.

In these new reactor designs a specific threat to the reactor is eliminated by choice of material and design. The so-called inherently safe characteristic makes it impossible for that specific threat to damage the reactor. To achieve an inherently safe characteristic passive components can be used. Passive components are components that do not need any form of external input (logic or power) in order to operate. Sometimes a system has both active and passive components. These systems can then be categorized in a scale ranging from active to passive. Generally the more passive a system is the safer it is.

A large number of different passive systems or processes are used in advanced and innovative new reactor designs. In the framework of the Dutch PINK¹ program a comparison was made between the various new advanced and innovative reactor designs (Bueno de Mesquita, 1991; Jehee, 1993). Examples of new designs are the SBWR which is a boiling water reactor (McCandless and Redding, 1989), the AP600 which is a pressurized water reactor (Vijuk and Bruschi, 1988), and various versions of the HTR, or High Temperature gas-cooled reactor. The SBWR (Simplified Boiling Water Reactor) design by General Electric uses natural circulation of the coolant water through the reactor core eliminating the dependence on circulation pumps and associated equipment (piping, valves, control systems etc.). High temperature gas-cooled reactors embed the uranium fuel in small coated particles (1 mm diameter) which can withstand high temperatures. In case of a loss of coolant in these HTR reactors the decay heat is transported largely by radiation to the reactor vessel wall, which in turn is cooled by natural convection of air along the outside of the reactor vessel. The reactor is designed in such a way that the maximum temperature in the core stays below the melting point of the fuel.

An interesting side-effect of the interest in inherent safe reactors is that there is more need for a good understanding of the physical processes involved, of which this thesis is an example. As we will see in the next section the work in this thesis is about *natural circulation*, a passive process which can be utilized in the design of inherently safe reactors.

¹ Programma Instandhouding Nucleaire Competentie (program for the preservation of nuclear competence)

1.1.2 *Natural circulation in boiling water reactors*

Of the new reactor designs currently being studied some require more changes in the nuclear infrastructure than others. For some designs new forms of uranium fuel must be developed and tested, or other fuel cycles such as the Thorium cycle. Such new reactor designs will not be available in the near future. Nevertheless, there is a need for safer and simpler reactors at this point in time because in the near future many existing reactors will come to the end of their life span and must be replaced. The present day Boiling Water Reactor (BWR) is in this sense interesting because it is suited to the new design philosophy of safe and simple while still building on existing technologies. General Electric has in 1982 started this route to new reactors with the design of the SBWR, or Simplified Boiling Water Reactor. This design has a number of features which justify the word simplified in the name. Most notable is the fact that the primary coolant flow is driven by natural circulation rather than by pumps. This eliminates the need for a lot of systems: coolant pumps, backup coolant pumps, piping, valves, power supply systems, backup power supply systems etc. Natural circulation of the coolant ensures adequate cooling of the reactor core in the short term. During this time the boiling of water removes the (decay) heat from the core. This boiled-off water in the reactor vessel must be replaced which is normally done by the feedwater pump, an active system. If this system fails, the core would eventually become uncovered. Therefore several additional safety systems are present in the design, such as the isolation condenser and the gravity driven emergency core cooling system. These are largely based on passive processes and can provide enough water for a period of 3 days. In 1996 GE abandoned the SBWR design in favor of a larger version of the reactor, the ESBWR, where the E stands for European (Arnold et al., 1996; Khorana et al., 1997). The ESBWR has a power of 1190 MWe, making it more economical compared to the 600 MWe SBWR.

As stated in the previous paragraph the adoption of natural circulation in a boiling water reactor can greatly simplify the design of the reactor, but the process itself is much more complex than forced circulation by pumps. The natural circulation flow rate is governed by physical processes in the reactor rather than being externally imposed on the system by the circulation pumps. To ensure adequate cooling of the reactor core at all times it must be known how the circulation flow behaves under a variety of conditions. Here lies the heart of the problem: how do you *prove* that the circulation flow rate will be sufficient under any given circumstance? All aspects of the application of natural circulation must be considered before it can truly be said that natural circulation systems are safer and as economical as forced circulation systems (Aritomi, 1990).

1.1.3 *Historical perspective on BWR stability research*

From the very beginning of BWR technology it was recognized that a boiling water reactor can become unstable under particular circumstances caused by a feedback between the thermal-hydraulics and the neutronics. This instability can result in oscillations of the power or of the flow rate. This realization led to extensive research in the field of BWR stability. Stability tests

were performed, among others at the Dresden reactor, where the response to oscillating control rod movements was measured across a range of frequencies (Beckjord, 1960). A comprehensive review of the current state of affairs with regard to BWR stability is given in an OECD-NEA report; *the State of the Art Report on Boiling Water Reactor Stability* (D'Auria et al., 1996). However, this report does not discuss stability of natural circulation cooled boiling water reactors.

Besides the tests being done on nuclear reactors, out-of-pile facilities were built in order to study in more detail the various phenomena thought to be important. One of the most prominent of these is the FRIGG loop which was built by ASEA and which has been in operation since 1966 (Nylund, 1969). This 8 MW water/steam loop has been fitted with a variety of fuel assembly designs. Among others, stability tests have been performed with this loop using a 36-rod fuel assembly. These measurements have been used to validate a variety of computer codes, for example RAMONA. The FRIGG loop is still in operation, and has been upgraded to a power of 15 MW.

Large full-scale test facilities like FRIGG are typically built and operated by reactor vendors, and the experimental results are not always available. Reduced scale facilities are much cheaper and have therefore found a widespread use. An example is the PIPER-ONE loop of the PISA University which has been in operation since 1985. It is a full-height (but reduced volume) loop that can be used for stability research although its more general purpose is to reproduce the BWR behaviour in thermal-hydraulic transients dominated by gravity forces (Bovalini et al., 1996; Billa et al., 1994). Maximum power was limited to 300 kW, 30% of the nominal power of the reference BWR. In this loop instabilities were observed.

One of the reasons that forced circulation BWRs were chosen over natural circulation BWRs is that analysis and experiments showed that an increase of the coolant flow rate has a stabilizing effect on BWRs. The knowledge gained by the experimental facilities helped to establish the BWR as a successful reactor type. The stability issues seemed to be solved. However, a number of stability incidents with reactors under non-normal operating conditions spurred new interest for this topic. The Caorso BWR in Italy became unstable during the start-up of the reactor in 1982 and 1984 (GE, 1983). At the La Salle 2 BWR in 1988 (IRS) the two recirculation pumps tripped and the reactor became unstable while in natural circulation mode. Now, of course, the renewed interest in natural circulation BWRs makes the stability issue even more important.

The reactor physics department of the IRI has had a long-time interest in this field, favored by the possibility of performing measurements at the natural circulation cooled Dodewaard nuclear reactor (see section 1.1.4) and the prospects of the new SBWR design. At first research was done on the development of measurement techniques such as noise analysis (Kleiss, 1983). These techniques were applied to measurements in the Dodewaard reactor of the response to control rod movements. Also attention was given to the measurement and monitoring of the stability of the Dodewaard BWR (Van der Hagen, 1989). For this purpose noise analysis techniques were again investigated and applied (Van der Hagen et al., 1988). To

gain a better physical understanding a simple theoretical model of the Dodewaard BWR was developed (Stekelenburg, 1994). This model is designed to simulate stationary conditions and slow transients. It was compared with measurements of the response to control rod and steam flow valve steps.

The research program concerning stability of natural circulation was extended with the completion of the DESIRE facility (see section 1.1.5). A new analytical model was developed which describes in much more detail the processes taking place inside the fuel channel and riser (Van Bragt and Van der Hagen, 1998a,b). In recent years an extensive set of measurements of the stability has been performed at Dodewaard. In these experiments the power and pressure were varied. The stability of the reactor during these experiments ranged from very stable to in one case unstable (Van der Hagen, 1997).

Worldwide, much work has been done on modeling of the BWR dynamics. In general these models provide us with a valuable understanding of the phenomena but, as the SOAR on BWR stability states: 'The range of phenomena predicted by codes can be found to be wider and denser than the one provided by observation of reality.' (SOAR, 1996). Thus there is a clear need for experimental data on these phenomena. However, the only system which comprises both the thermal-hydraulics and the neutronics of a BWR is the BWR itself. Experimental data from BWRs is limited and experiments on real BWRs are difficult and sometimes impossible.

Thermal-hydraulic facilities can be used to validate parts of the models, but these all lack the neutronic feedback. This can be remedied by implementing the facility with a simulated neutronic feedback, thus creating a hybrid system. Such hybrid systems have the advantage of combining the flexibility of simulations with the reality of a real physical system. DESIRE has been implemented with such a simulated feedback.

In DESIRE the thermal-hydraulics is real and the neutronics is simulated. The opposite has been done in a reactor where the neutronics was provided by a Triga research reactor and the thermal-hydraulics was simulated (Turso et al., 1994). The calculated reactivity effect of the thermal-hydraulics was realized by control rod movements. Since the thermal-hydraulics is far more difficult to model than the neutronics this seems a less fruitful approach. An approach similar to the one used in DESIRE was used in a low pressure water facility (Meftah and Ruggles, 1997). At the moment however, the power supplies in that facility are too slow to allow real investigation of the stability.

1.1.4 *An old modern reactor*

Although it is now receiving a lot of attention the concept of natural circulation in BWRs is not new. In the Netherlands a small (60 MWe) BWR using natural circulation has been in operation from 1968-1997: the Dodewaard BWR. Considering the renewed interest in natural circulation it is not surprising that this reactor has been studied extensively. A large series of measurements has been performed by the reactor physics group of the Interfaculty Reactor Institute, which is part of the Delft University of Technology in The Netherlands (Van der

Hagen et al., 1992, Van der Hagen et al., 1993). It is however difficult to perform measurements on a real nuclear reactor due to the limited number of sensors available and the restrictions on the operating conditions. For instance there are no flow meters installed in Dodewaard that measure the natural circulation flow rate. This clearly is a handicap when trying to study the natural circulation. Other limitations when measuring at Dodewaard are that it is not possible to measure the void-fraction (volumetric amount of steam) or the carry-under. Also it is not possible to perform measurements under extreme conditions, for example at very high power, or low pressure. Therefore it was decided that to complement the work done at the Dodewaard reactor an experimental facility would be built. This facility would be based on the Dodewaard reactor but would not have the restrictions mentioned above. The addition of a simulated void-reactivity feedback provides another advantage of the facility over the Dodewaard reactor. This makes it possible to study separately the thermal-hydraulic system and the coupled neutronic- thermal-hydraulic system. Although the link with the Dodewaard reactor is clearly present, the facility should also be focused on the new reactor designs.

1.1.5 The DESIRE experimental facility

The project to design and build the DESIRE facility was started in 1991. The facility was first called SIDAS, for *Simulated Dodewaard Assembly* but was later renamed to DESIRE, which stands for *Delft Simulated Reactor*. During 1991-1992 a scaling study was performed by Ruud van de Graaf, Tim van der Hagen and Rob Mudde (Van der Graaf et al., 1994a, 1994b, 1994c). On the basis of the obtained scaling rules the facility was designed and built between 1992 and 1994. It came into operation in 1994. In the following years some improvements and extensions were made such as the installment of a magnetically coupled feedwater pump, software for monitoring and control of the facility, a gamma-transmission void-fraction measurement set-up (chapter 3) and a void-reactivity feedback simulation (chapter 5).

1.2 Outline of this thesis

Chapter 2 starts with a short outline of the scaling laws that were used in the scaling of DESIRE. The result of the scaling analysis is a set of dimensionless numbers which must be equal for both the original and the scaled facility. Next the DESIRE loop is described, and the basic instrumentation present in DESIRE is listed.

One of the most important parameters affecting the natural circulation flow rate is the void-fraction. This is investigated in chapter 3, where a method is developed to measure the void-fraction in the fuel assembly on a subchannel basis using the γ -attenuation technique in combination with a tomographic reconstruction technique. Measurements are performed using this technique and a comparison is made with two-phase flow models.

In chapter 4 a model is developed which describes the various pressure drops and driving forces along the loop. This model can be used to predict the behaviour of DESIRE during

steady-state operation. The steady-state model is compared with measurements of the natural circulation flow rate as a function of various parameters.

In chapter 5 the attention is shifted from steady-state operation to the dynamics of the natural circulation loop. First some of the issues surrounding the dynamics are discussed. Next a model developed by Van Bragt is shortly outlined and applied to DESIRE. The design and implementation of a simulated void-reactivity feedback in DESIRE is described.

The measurements on the dynamics and stability of DESIRE with and without feedback are presented in chapter 6. The results are discussed and a comparison is made with the model of the dynamics. Also some suggestions for improvements to the simulated feedback are made. Finally, the general conclusions of this work are given in chapter 7.

Chapter 2

The DESIRE facility

2.1 *The foundations of the DESIRE facility*

The most important aspect of the thermal-hydraulics in a natural circulation reactor is the so-called void-fraction, which is the volume of vapour relative to the total volume. This is due to the dual role of the vapour in a natural circulation BWR: it transports the heat from the core to the turbines, and it provides the driving force for the coolant flow. Therefore major attention was paid to the void-fraction during the design of the facility. Also the need to measure the void-fraction was recognized.

Thermal-hydraulically a reactor core consists of many independent fuel assemblies. These are rectangular channels containing between 36 and 144 fuel rods. The coolant flows between the fuel rods through the assembly. The Dodewaard reactor contains 164 of these assemblies, which are 1.8 meters high and have a cross-section of 13 by 13 cm. Since the flow in one fuel assembly is mechanically separated from the flows in the other fuel assemblies it is useful to study in detail the flow in one fuel assembly separately.

Next important point is that one fuel assembly in the Dodewaard reactor produces on average 1.1 MW of heat. To produce this amount of heat in an electrically heated fuel assembly would be prohibitively expensive. Also the pressure (75 bars) and temperature (391 °C) are too high to be practical. These problems led to the adoption of a scaling liquid. The refrigerants are widely used as scaling liquid, for DESIRE it was decided to use Freon-12. In table 2.1 the properties of Freon-12 and water are given at the appropriate pressures.

	Water at 75.5 bar	Freon at 11.6 bar
saturation temperature (°C)	291	48
density liquid (kg/m ³)	731	1220
vapour (kg/m ³)	39.9	66.4
enthalpy liquid (kJ/kg)	1295	447.7
vapour (kJ/kg)	2764	571.7
specific heat of liquid (kJ/kg)	5.45	1.058
surface tension (N/m)	$17.6 \cdot 10^{-3}$	$5.85 \cdot 10^{-3}$
dynamic viscosity (Pa s)	$0.100 \cdot 10^{-3}$	$0.127 \cdot 10^{-3}$

Table 2.1 Thermodynamic properties of water and Freon-12 on the saturation line.

Thus DESIRE was designed around the following keystones:

- The basis is formed by one copy of a fuel assembly of the Dodewaard reactor;
- The fuel assembly is placed in a natural circulation loop;
- Freon-12 is used as a scaling liquid;
- Scaling laws are derived to determine the dimensions and operating points for the facility;
- The fuel assembly must be accessible for instrumentation and visual inspection.

These design criteria lead to a facility with which the following research areas can be addressed:

- Characteristics of two-phase flow: flow patterns, void-fraction distribution;
- Natural circulation as a function of operating parameters;
- Thermal-hydraulic dynamics;
- Coupled neutronic/thermal-hydraulic dynamics.

The resulting facility will be described in this chapter. Also some of the considerations which have led to a particular feature of the design are given. The scaling analysis is shortly outlined in section 2.3, which concludes with the main dimensions of the facility. A detailed description of DESIRE is then given in section 2.4, and the instrumentation is described in section 2.5.

2.2 Concepts of two-phase flow

Before we proceed with the scaling analysis it is necessary to introduce a number of concepts used in the field of two-phase flow. For this purpose a description will be given of a simple heated flow channel (figure 2.1).

The *thermodynamic equilibrium quality* of the flow is a dimensionless number which is defined as:

$$x_{eq}(z) \equiv \frac{h(z) - h_l^{sat}}{h_{ev}} \quad (2.1)$$

where $h(z)$ is the enthalpy of the flow at height z , h_l^{sat} is the enthalpy of the liquid at the saturation temperature and h_{ev} is the heat of evaporation. The thermodynamic equilibrium quality can in principle take on any value; it is smaller than zero if the enthalpy of the flow lies below the saturation enthalpy (temperature below boiling point) and it is larger than one in the case of superheated steam. This quality is called thermodynamic equilibrium quality because it is defined using the thermodynamic concept of the enthalpy of the flow. A second definition of quality is the *flow quality*, which is defined as:

$$x(z) \equiv \frac{\dot{m}_g(z)}{\dot{m}} \quad (2.2)$$

which is the vapour mass flow rate relative to the total mass flow rate. Note that $0 \leq x \leq 1$, which is not true for x_{eq} . For a two-phase flow at thermodynamic equilibrium it can be derived that $x_{eq} = x$.

----- Thermodynamic equilibrium quality
 — Flow quality

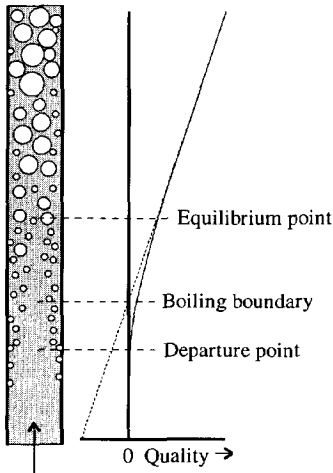


Figure 2.1 Development of the thermodynamic equilibrium quality and the flow quality in a simple heated flow channel with uniform heat flux.

The development of the two qualities along the heated channel is sketched in figure 2.1. The liquid enters the flow channel at the bottom at a temperature below the boiling point. This is called subcooled liquid, and $x_{eq} < 0$. The subcooling temperature is defined as:

$$T_{sub} \equiv T_{inl}^{sat} - T_{inl} \quad (2.3)$$

which is the difference between the saturation and liquid temperature at the inlet of the channel. The saturation temperature depends only on the pressure, which is a function of height, so the saturation temperature is also a function of height.

As the liquid near the wall starts to heat up small bubbles are formed. At a certain height these bubbles are large enough to escape from the rod wall into the bulk of the flow. The height at which this happens is called the *departure point*. Above the departure point the flow quality is larger than zero, while the thermodynamic

equilibrium quality is still smaller than zero. The next significant point is the point at which $x_{eq}=0$, sometimes called the (*bulk*) *boiling boundary*. Finally, at a certain height the flow reaches thermodynamic equilibrium at the *equilibrium point*, where $x_{eq}=x$.

The *volumetric* void-fraction α is defined by:

$$\alpha \equiv \frac{V_g}{V} \quad (2.4)$$

where V_g is the volume of the vapour in the total volume V . Another void-fraction is the *chordal* void-fraction, which is given by:

$$\alpha^* \equiv \frac{l_g}{l} \quad (2.5)$$

where l_g is the total length of the parts of a line passing through the vapour phase relative to the total line length l passing through the two-phase flow. Other definitions of the void-fraction are the area-averaged (cross-sectional) void-fraction and the local void-fraction. The latter is defined as the relative amount of time a point is occupied by vapour.

The flow quality and void-fraction are closely related. The simplest model which relates these two is the homogeneous equilibrium model (HEM). This model is valid for a flow at thermodynamic equilibrium where the two phases are mixed homogeneously and have the same velocity. The void-quality relation for the HEM is given by:

$$\alpha = \frac{x}{x + \frac{\rho_g}{\rho_l}(1-x)} \quad (2.6)$$

with ρ_g and ρ_l the densities of the vapour respectively the liquid phase.

A somewhat more sophisticated and widely used model is the *drift-flux* model (Zuber and Findlay, 1965). This is an one-dimensional model that describes the flow as an one-phase mixture just like the homogeneous model. However, two important effects can be accounted for in the drift-flux model: the different velocities of the two phases (via the local drift velocity) and the distribution of the two phases (via the distribution parameter). The local drift velocity and the distribution parameter must be supplied to the drift-flux model.

The void-quality relation for the drift-flux model is given by:

$$\alpha = \frac{x}{(x + \frac{\rho_g}{\rho_l}(1-x))(C_0 + \frac{v_{gj}}{\langle j \rangle})} \quad (2.7)$$

with C_0 the distribution parameter:

$$C_0 = \frac{\langle \alpha j \rangle}{\langle \alpha \rangle \langle j \rangle}, \quad (2.8)$$

v_{gj} the local drift velocity of the vapour:

$$v_{gj} = v_g - j, \quad (2.9)$$

and j the volumetric flux which is defined as:

$$j = v_l (1 - \alpha) + v_g \alpha \quad (2.10)$$

where v_l and v_g are the velocities of the liquid and gas phases. The angle brackets denote an averaging operation over the channel cross-section.

The drift-flux model is useful because it relates to physical phenomena. The distribution parameter can be easily understood to account for the effect of a non-uniform velocity profile across the flow channel. In a rod-bundle the velocity will be low near the rod walls and high in the center between the rods. If the vapour is concentrated near the rod walls, for example at or near the subcooled boiling region, the distribution parameter will be smaller than one. On the other hand if the vapour is concentrated at the center of the flow channels, which is the case for annular flow, the distribution parameter will be larger than one.

The local drift velocity is caused by the gravitational force on bubbles, it depends on the bubble size. For both the distribution parameter and the local drift velocity empirical correlations are available.

2.3 Scaling analysis

Scaling is a widely used technique for studying systems with flowing media. The idea behind scaling is to build a copy of the system at a reduced size. Some aspects of the flow in the scaled facility will be different from the original, while other aspects can remain equal. For example, in a full-height scaled facility the gravitational pressure drop can be equal for both the original and the scaled facility while frictional pressure drops might be different. Since it is never possible to design a scaled facility which will behave exactly like the full size facility it is necessary to identify the most relevant processes. The equations describing these processes are then used in the scaling analysis.

The choice of equations to be used in the scaling analysis is very important. Different sets of equations each lead to different scaling rules resulting in a different test facility. It is also important to keep this in mind when analyzing the measurements performed with the facility: only those phenomena which have been correctly scaled can be extrapolated to the full sized facility. Once the equations are chosen the scaling criteria are deduced from these equations. This is done by rewriting the equations in a non-dimensional form. The parameters in these

equations are dimensionless numbers which must have equal values for the scaled and full-size facility.

In the two-fluid formulation for a non-adiabatic two-phase flow there are six conservation equations: the mass, momentum and energy conservation equation for each phase. In addition so-called closure relationships are needed. These describe the interaction between the two phases, for example evaporation or condensation, where mass, momentum and energy can be transported from one phase to the other phase.

The empirical models used for the closure relationships rely on assumptions on the nature of the two-phase flow. Therefore a different set of equations can be derived for different flow patterns. Many different authors have derived different sets of scaling rules. There is no such thing as the 'best' set of scaling rules. Each set is usually derived with a particular application in mind and the scaling rules are appropriate for that particular application. This also means that for each new facility the scaling analysis should be done again. The literature can be used as a reference to what other researchers have found to be important scaling rules for particular applications (Kakac and Mayinger, 1977; Ishii and Jones, 1976).

Natural circulation systems have been scaled (Ishii and Kataoka, 1983). Symolon compared the scaling of a system very similar to DESIRE (Freon in a rod bundle) with numerical calculations using a two-fluid model (Symolon, 1990). He concluded that a half-scale Freon model accurately models the void-fraction for all flow regimes except for bubbly flow with a void-fraction below 10%.

2.3.1 Results of the scaling analysis

A full derivation of the scaling laws used and the dimensionless groups obtained is given in Van de Graaf (1994a, 1994b). This section gives a short overview of the results.

As stated in the introduction the void-fraction is one of the parameters which is very important in natural circulation. In the drift-flux model the void-fraction is determined by the quality, the drift velocity and the distribution parameter, so these three parameters need to be scaled correctly. Correct scaling of the thermodynamic equilibrium quality is achieved if the following two dimensionless groups are kept constant:

$$\begin{aligned} N_{pch} &= \frac{P}{\Phi h_{ev}} \frac{\Delta\rho}{\rho_g} \\ N_{sub} &= \frac{h_{inl}^{sat} - h_{inl}}{h_{ev}} \frac{\Delta\rho}{\rho_g} \end{aligned} \quad (2.11)$$

with N_{pch} the phase change number, N_{sub} the subcooling number, P the power, Φ the flow rate, $\Delta\rho$ the density difference between the liquid and vapour phases and ρ_g the density of the vapour phase. The phase change number is also sometimes called the Zuber number, N_{Zu} .

In the subcooled boiling region, between the departure point and the equilibrium point, the flow quality and the thermodynamic equilibrium quality are not equal to each other. The flow quality in this region is described with a profile-fit method. The fit that was used in the scaling of DESIRE is given by: (Lahey and Moody, 1993)

$$x(z) = x_{eq}(z) - x_{eq,d} \exp\left(\frac{x_{eq}(z) - x_{eq,d}}{x_{eq,d}}\right) \quad (2.12)$$

with x_{eq} the equilibrium quality and $x_{eq,d}$ the equilibrium quality at the departure point. Note that since $x_{eq,d}$ is negative $x > x_{eq}$. The development of the flow quality in the subcooled boiling region now depends only on $x_{eq,d}$. According to the model of Saha and Zuber (Saha and Zuber, 1974) the thermodynamic equilibrium quality at the departure point is proportional to N_{pch} as long as

$$N_{P\epsilon} = \frac{\dot{m}'' c_l D_h}{\lambda_l} > 7 \cdot 10^4 \quad (2.13)$$

with \dot{m}'' the mass flux, c_l the specific heat, D_h the hydraulic diameter and λ_l the thermal conductivity. For Dodewaard the Péclet number, $N_{P\epsilon}$, equals $1.6 \cdot 10^5$, therefore proper scaling of the flow quality in the subcooled boiling region is obtained by keeping the phase change number and the subcooling number constant.

Now that the flow quality is scaled correctly, the next step is to scale the void-fraction. Ishii et al. (1977) gave scaling criteria for two-phase flow loops derived from the conservation equations using the drift-flux model. Besides N_{pch} the following dimensionless numbers are important for the proper scaling of the void-fraction and void-distribution in a flow in thermal equilibrium:

$$\begin{aligned} N_\rho &= \frac{\rho_g}{\rho_l} \\ N_g &= \frac{D_h}{H} \\ N_{Fr} &= \frac{(\dot{m}'')^2}{\rho_l^2 H g} \\ N_d &= \frac{\rho_l (C_0 - 1) j}{\dot{m}''} + \rho_l \frac{v_{gj}}{\dot{m}''} \end{aligned} \quad (2.14)$$

with N_ρ the density ratio, N_g the geometry number, N_{Fr} the Froude number and N_d the drift-flux number. H is the height of the assembly and g the gravitational acceleration. The drift-flux number contains the parameters C_0 and v_{gj} which are flow regime dependent. For the churn-bubbly and slug flow regimes correlations for these parameters are available. Using these

correlations it is found that proper scaling is achieved if besides N_p and N_{Fr} the following dimensionless number is kept constant (Weber number):

$$N_{We} = \frac{\dot{m}'' D_h}{\rho_l \sigma} \tag{2.15}$$

with σ the surface tension. Unfortunately, for the bubbly flow regime, the drift velocity depends on the unknown and uncontrollable bubble size. Therefore the bubbly flow regime cannot be properly scaled.

Application of these dimensionless numbers for water to Freon-12 scaling leads to the values given in table 2.2 Notice that the size, pressure and power have to be reduced considerably when using Freon-12 instead of water.

System parameter	Determined by	Dodewaard value	DESIRE value
pressure (bar)	N_p	75.5	11.6
dimensions (mm)	$(N_{We} N_g)/N_{Fr}$		
length fuel rod		1800	830
diameter rod		13.5	6.23
area of assembly		130x130	60x60
riser length		2840	1310
mass flux ($\text{kg}\cdot\text{m}^{-2}\cdot\text{s}^{-1}$)	N_{Fr}	1006	1137
power (kW)	N_{pch}	1116	22.3
subcooling ($^{\circ}\text{C}$)	N_{sub}	5	2
inlet velocity (m/s)	\dot{m}'' / ρ_l	1.37	0.93
channel transit time (s)	$(H \rho_l) / \dot{m}''$	1.31	0.89

Table 2.2 Results of the scaling analysis. The first column gives the system parameter which is determined by the dimensionless number in the second column. The third and fourth column give the Dodewaard and DESIRE values of the parameter.

Flow quality and void-fraction are now properly scaled, the friction however is among others determined by viscous forces which are reflected in the Reynolds number. For Dodewaard the Reynolds number for a fuel assembly is about $2\cdot10^5$, while for DESIRE it is $4\cdot10^4$, a difference of a factor of five. The frictional pressure losses are therefore not properly scaled. This is one of the reasons why it was chosen to use a riser of variable length. The total frictional pressure drop over the circulation loop can be adjusted manually by means of a valve located just below the fuel assembly.

The water-to-Freon scaling analysis outlined above is based upon a simple drift-flux model. Verification of the scaling can be performed by comparing DESIRE and Dodewaard calculations using a more sophisticated model. This has been done using the commercial thermal-hydraulic code MONA, which contains an advanced seven-conservation equation,

two-fluid model (Scandpower): separate equations are used to describe the mass, energy and momentum of both the gas and the liquid film phases, with a final mass equation included to treat the droplets. Two MONA models were made: one using the DESIRE dimensions with Freon-12 as a coolant and the other using a fictitious full-scale DESIRE facility with water as the coolant (Adams, 1997). For both cases the axial void-fraction profile was calculated. The results are shown on the left of figure 2.2. Excellent agreement between the two cases is found at every position except for a small discrepancy between nodes 3 to 5 (each node corresponds to 6.285 cm in DESIRE and 13.6 cm in Dodewaard). This is the region of bubbly-flow, where proper scaling could not be achieved.

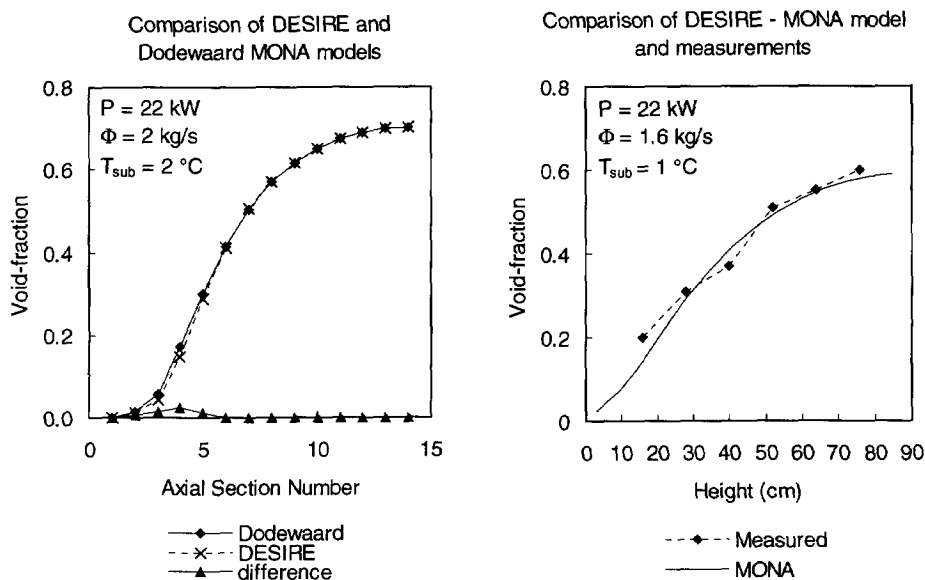


Figure 2.2 Comparison of the DESIRE and Dodewaard MONA models and the benchmarking of the DESIRE MONA model against measurements of the void-fraction.

The MONA model of DESIRE was also benchmarked against measurements of the void-fraction (see chapter 3). The measured and calculated void-fractions are shown on the right of figure 2.2. Again the agreement is good.

2.4 Description of the DESIRE facility

Based on the results of the scaling analysis the design of the facility was completed by Van de Graaf, Van der Hagen and Mudde. Figure 2.3 shows a schematic view of the DESIRE loop.

The primary loop consists of the fuel assembly, riser, downcomer and downcomer loops. The Freon-12 flows through this loop by natural convection. At the top of the riser separation of liquid and vapour takes place at the free surface. The liquid flows into the downcomer, while the vapour flows upwards into the secondary loop. There it first passes a pressure controlling valve (Refrigerating Specialties type A4A Range D). The setpoint of this valve determines the pressure in the primary loop (nominal pressure is 11.6 bar). The vapour is then condensed in the condenser. The pressure in the secondary loop is determined by the temperature of the condensed liquid, which depends on several factors, but is typically about 30 °C, corresponding to a pressure of about 8 bars. Before this liquid is pumped back into the primary loop it can be cooled to about -10 °C by a heat exchanger which is connected to a separate cooling system. The temperature and mass flow rate of the feedwater flow are important boundary conditions for the primary circuit. The liquid level in the primary circuit is controlled via the feedwater flow rate. The different components of the facility will now be examined in more detail.

2.4.1 Fuel assembly

The fuel assembly consists of the following parts: 35 fuel rods, 3 spacers, bottom nozzle, top nozzle and a dummy (instrumented) fuel rod all contained in the fuel assembly casing. The fuel rods are Incoloy 800 tubes with a wall thickness of 0.3 mm and are filled with boron nitride. A coiled resistance wire (80%Ni, 20%Cr) produces the heat in the center of the rod. The resistance of the resistance wire is $(159 \pm 3) \Omega$. The error reflects the variability of the resistance between individual fuel rods (one standard deviation). The maximum rated power for one fuel rod is 1613 Watts.

The pitch of the coils of the resistance wire is a function of the axial position in the rod, in such a way that the power profile of the fuel rods is a cosine plus offset (chopped cosine):

$$P'(z) = P \frac{(1 - \frac{2}{\pi} f_p) + (f_p - 1) \sin(z \frac{\pi}{H})}{H(1 - \frac{2}{\pi})} \quad (2.16)$$

where f_p is an axial peaking factor which has the value of 1.4 for DESIRE.

This chopped cosine axial power distribution corresponds to the fundamental mode of the neutron flux in a nuclear reactor. In a boiling water nuclear reactor this fundamental mode is perturbed by the varying density of the coolant along the height of the reactor core, by the burn-up of the fuel and by the insertion of control rods from the bottom of the core. Since these perturbations change during the operating cycle it is not possible to define one specific power profile for the reactor. Therefore the chopped cosine profile was adopted in DESIRE as representative of the power profile in BWRs. In principle rods with different power profiles can be loaded into the assembly.

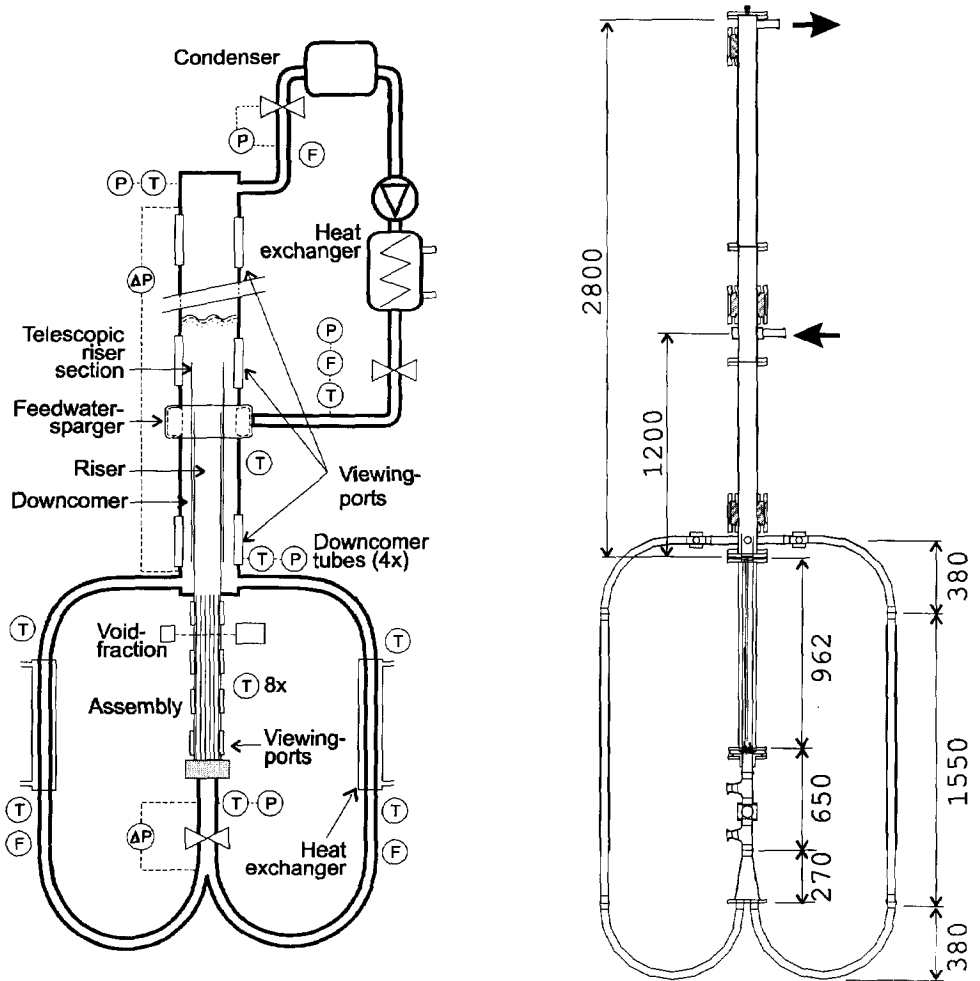


Figure 2.3 Overview of the DESIRE facility showing the instrumentation on the left (not to scale) and showing the dimensions on the right (to scale, measurements in mm). Only two of the four downcomer loops are shown. T=thermocouple, F=flowmeter, P=pressure sensor, ΔP =differential pressure sensor.

The fuel rods are arranged in a square 6x6 lattice with a pitch of 8.8 mm. One of the four central fuel rods is not a fuel rod but an unheated instrumentation rod with the same dimensions as a heated rod. This corresponds with one of the four central fuel rods in Dodewaard which does not contain any uranium but is filled with water. The purpose of this dummy rod in Dodewaard is to flatten the radial power profile by suppressing the power produced in the center of the assembly.

The fuel assembly is contained in a square stainless steel tube with an inner side of 54 mm and a wall thickness of 3 mm. Four pairs of viewing ports are located in the fuel assembly positioned at 70, 363, 602 and 892 mm from the bottom of the assembly. The diameter of the viewing ports is 44 mm. The glass is aligned flush with the inner surface of the fuel assembly casing.

The fuel rods are held in place by three spacers located at 251, 491 and 731 mm from the bottom of the assembly. The spacers are exact scaled copies of the spacers used in the Dodewaard reactor. The height of the spacers is 24 mm.

The bottom nozzle of the DESIRE fuel assembly is designed in such a way as to allow each fuel rod to be connected individually to one of six power supplies while retaining the shape of the Dodewaard bottom nozzle. In this way it is possible to create a variety of radial power profiles.

2.4.2 *Riser*

The riser consists of a fixed part and a telescopic part. The fixed part is a glass square tube with an inner dimension of 54 by 54 mm and a wall thickness of 3 mm. It has a length of 1000 mm and is mounted directly on top of the fuel assembly. The telescopic part also has a length of 1000 mm but has a larger inner dimension of 61 by 61 mm and walls of 3 mm. The telescopic section fits around the fixed section and can be moved up and down during operation, thus creating a variable riser length between approximately 1.1 and 1.9 meters. The riser was made of glass to allow visual inspection of the two-phase flow in the riser through viewing ports in the downcomer casing.

2.4.3 *Downcomer*

The downcomer tube is placed concentric around the riser. The downcomer does not extend to the bottom of the fuel assembly as in Dodewaard, but ends at the top of the fuel assembly, where the flow is diverted into four loops. The downcomer consists of three lengths of square stainless steel tubing with an inner dimension of 90 by 90 mm and walls of 3 mm. Total length of the tube is 2.8 meters, which leaves 0.9 to 1.7 meters above the riser exit. Viewing ports are located at 200 mm, 1300 mm and 2600 mm above the top of the fuel assembly. The viewing port at 1300 mm is located in the range of the riser exit, so the flow at this point can be inspected visually. The feedwater sparger is located 1200 mm above the top of the fuel

assembly. It injects the feedwater evenly from all sides into the downcomer flow through 36 holes of 2 mm diameter.

The downcomer loops divert the flow away from the fuel assembly. Each of the four loops consists of the following sections, from top to bottom (see figure 2.3)

- Horizontal straight section with a length of 380 mm, inner tube diameter 40 mm.
- 90 degrees curve with a radius of 380 mm, inner tube diameter 40 mm.
- A heat exchanger consisting of two concentric tubes of 1000 mm length. The inner tube has a diameter of 40 mm. The secondary side of the heat exchanger can be connected to the water mains. Approximately 2-3 kW of heat can be extracted from the primary loop, increasing the subcooling by some 2°C.
- Straight section for the flow meters: 550 mm of 30 mm tube.
- 180 degrees curve with a radius of 380 mm, inner tube diameter 40 mm.

The four loops are joined in a conical section with a length of 270 mm, a bottom diameter of 129 mm and top diameter of 50 mm.

Finally, above the conical section a section with two T-junctions and a valve, total length 650 mm, tube diameter 50 mm, connects the loop to the bottom of the fuel element.

The downcomer tubes were designed in such a way that the residence time in the downcomer relative to the total circulation time is the same in DESIRE as in Dodewaard. Another consideration was that the frictional pressure losses over the downcomer and downcomer tubes must be small compared with other pressure losses.

2.5 Instrumentation

Figure 2.3 also shows the approximate positions of the instrumentation in DESIRE. For the basic instrumentation we can identify thermocouples, flow meters, pressure sensors and differential pressure sensors. The void-fraction measuring device is described separately in chapter 3.

2.5.1 Thermocouples

All thermocouples used in DESIRE are chromel-alumel thermocouples with a diameter of 0.5 mm and a sensitivity of 40 $\mu\text{V}/^\circ\text{C}$.

Eight thermocouples are located in the fuel assembly. They are mounted in the instrumented fuel rod and extend into the bulk of the flow. The first one is placed 12 mm from the bottom of the fuel assembly, the rest at 100 mm intervals. Four thermocouples are placed at the bottom of the riser, just above the top nozzle. They are positioned above different subchannels. In the downcomer one thermocouple is located 150 mm from the bottom and one at 1050 mm from the bottom. The vapour temperature is measured at the very top of the downcomer tube, near

the vapour exit point. The feedwater temperature is measured by a thermocouple in the feedwater line, close to the feedwater sparger. In each downcomer loop one thermocouple is placed just before the heat exchanger and one just below the heat exchanger. Two thermocouples are located at the inlet 150 mm below the fuel assembly.

2.5.2 *Pressure sensors*

Four pressure sensors are located at the following positions:

- Pi At the inlet 210 mm below the fuel assembly
- Pd In the downcomer 150 mm from the bottom
- Pv At the top of the downcomer tube near the vapour exit ('steam dome')
- Pc In the feedwater line close to the feedwater sparger

These sensors measure the absolute pressure.

2.5.3 *Flow meters*

The main circulation flow rate is measured by four vortex flowmeters in the downcomer loops. (Endress+Hauser SwingWirl II DMV 6331 with an inner diameter of 26.6 mm.)

The feedwater flow rate and the vapour flow rate are both measured by vortex flowmeters. (Endress+Hauser SwingWirl II DMV 6331 with an inner diameter of 14 mm)

These flow meters work on the principle of vortex shedding. The frequency of the vortex shedding is determined by the flow velocity, and typically lies in the range of 10-20 Hz in DESIRE. This frequency is converted to a 4-20 mA current, which requires an averaging over time of the vortex frequency. The SwingWirl manual states that the time constant of this low-pass filter is 2 seconds. This means that these flow meters are too slow for dynamic measurements. It was found possible to experimentally determine the transfer function of the electronics in the flow meter which convert the vortex shedding frequency to the 4-20 mA current. Using this experimentally determined transfer function the dynamic measurements could be corrected for the low-pass filter and the flow rate variations up to 2 Hz could be handled.

2.5.4 *Differential pressure sensors*

Two differential pressure sensors are installed in DESIRE. One measures the pressure drop over the inlet valve. The other is connected between the bottom and top of the downcomer tube. This gives an indication of the collapsed liquid level in the downcomer, and thus of the collapsed liquid level above the riser exit.

Chapter 3

Subchannel void-fraction measurements

3.1 *Measurement technique*

The void-fraction and its distribution is essential for three important processes in a natural circulation BWR. These are:

Removal of heat from the fuel

The evaporation of liquid is a very efficient means of removing the heat produced by the fission in the reactor core. To ensure adequate cooling of the fuel rods they must be kept covered with liquid. If the vapour forms a vapour film on the fuel rod walls the temperature of the fuel will rise and damage may occur. This is called *dryout* and is a limiting factor in fuel performance. To maximize the fuel performance the vapour must be transported to the bulk of the flow, while liquid droplets in the bulk should be deposited back on the liquid film on the fuel rods. One way to achieve this is with new spacer designs (Yano et al., 1997). It is interesting to note that spacers can now be considered to improve fuel performance instead of only having the drawback of an increased pressure drop.

Providing the driving force for the natural circulation

To prevent dryout of the fuel the flow rate of the coolant through the core must be maintained at a sufficient level. In a natural circulation BWR this flow is driven by the density difference between the riser and downcomer. Only the average void-fraction is important for this density difference. The frictional and accelerational pressure drops of the flow also depend on the void-fraction.

Affecting the moderation of neutrons

The water in the reactor core acts as a moderator for the fast neutrons generated by the nuclear fission. The presence of vapour, or equivalently, the absence of water thus has a direct effect on the neutronics of the reactor. This is usually expressed in terms of the void-reactivity (see chapters 5 and 6). This reactivity effect depends not only on the average void-fraction but also on the axial distribution of the vapour.

For many purposes it is sufficient to know the cross-sectional averaged void-fraction as a function of the height. However, it is well known that the vapour is not distributed homogeneously throughout the fuel assembly (Lahey et al., 1971). These effects can influence the average void-fraction, so it was decided to make a more detailed study of the void-fraction in the fuel assembly. The following goals were set for the void-fraction measurements:

- Provide data to enable us to choose a model or correlation which correctly predicts the average void-fraction in DESIRE for the benefit of natural circulation models.
- Provide data for adjusting parameters in the chosen models or correlations.
- Give insight into the distribution of the vapour in the fuel assembly (flow patterns).

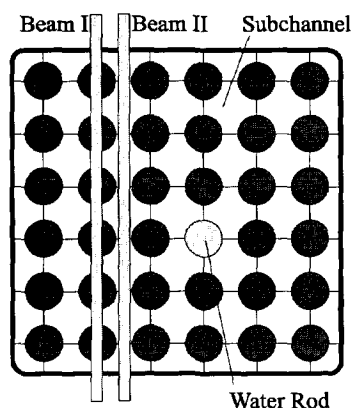


Figure 3.1 Cross-section of the DESIRE fuel assembly with 35 fuel rods and one water rod. The definition of the subchannel is shown as well.

In the study of two-phase flow through rod bundles an often applied concept is the *subchannel*. In a rectangular bundle geometry a subchannel is a region in the rod bundle surrounded by four fuel rods (see figure 3.1). If the pitch-to-diameter ratio of the fuel rods is relatively small the connection between individual subchannels is narrow and the flows in the subchannels will be independent of each other. If, on the other hand, the pitch-to-diameter ratio is large then mass and enthalpy transport can take place between different subchannels. In DESIRE the pitch-to-diameter ratio is 1.3.

The study of the two-phase flow through connected subchannels is referred to as subchannel analysis. Lahey (1990) gives an overview of the development of this field of research. Experiments with air-water systems in pipes have shown concentration of air near the pipe walls at low void-fraction but a concentration of air in the middle of the pipe at high void-fraction (Serizawa and Kataoka, 1987; Wang et al. 1987). However, steam-water systems can

behave differently, and the complex geometry of a BWR fuel assembly needs to be studied separately. Lahey (1972) performed measurements on a 3x3 rod fuel assembly, which contains all three types of subchannels (corner, wall and center) of a typical BWR assembly. The main conclusion from these measurements was that the corner and wall subchannels have a lower void-fraction than the center subchannels, even though the power-to-flow area ratio is higher in the corner and wall subchannels. Yadigaroglu (1995) investigated this phenomenon further by looking at the fully developed quality and mass distributions at the exit of a long adiabatic test section containing the three types of subchannel. Their results also show a smaller void-fraction for the corner and wall subchannels. Measurements on a full scale electrically heated assembly have been performed using X-ray tomography (Yagi et al. 1992; Inoue et al., 1995). For the first time this has provided a very detailed void-fraction distribution in a full-scale 8x8 fuel assembly. However, the tomography measurements could only be performed at the exit of the fuel assembly. At other heights along the assembly X-ray densitometers were used to measure only the average void-fraction.

It was decided to use the subchannel concept as the basis for the void-fraction measurements in DESIRE. That is, the void-fraction in each subchannel will be measured as a function of height. To achieve this a tomographic gamma-transmission technique is used.

3.1.1 Gamma-transmission technique

The gamma-transmission void-fraction measurement technique is a non-intrusive and accurate method of measuring void-fractions in two-phase flows (Schrock, 1969). In the most basic application of this technique a gamma-emitting radioactive source is placed on one side and a detector on the other side of the two-phase flow. To create a well-defined narrow beam a collimator is placed in front of the source and detector.

When a material with a linear attenuation coefficient μ is placed between the source and the detector the countrate I measured by the detector can be written as :

$$I = I_0 e^{-\mu d} \quad (3.1)$$

where I_0 is the countrate which is measured when nothing is placed between source and detector and d is the distance of the beam passing through the material. If the beam passes through several materials consecutively, for example through the liquid and vapour phases in a two phase flow we can write:

$$I = I_0 e^{-(\mu_m d_m)} e^{-(\mu_l d_l + \mu_g d_g)} \quad (3.2)$$

where we have separated the attenuation in the structural materials (μ_m) and the attenuation in the two phases of the flow. Next we define the countrate for the situation that the flow is single-phase liquid and single-phase vapour:

$$\begin{aligned} I_l &= I_0 e^{-(\mu_m d_m)} e^{-(\mu_l d)} \\ I_g &= I_0 e^{-(\mu_m d_m)} e^{-(\mu_g d)} \end{aligned} \quad (3.3)$$

Combining equations 3.2 and 3.3 we obtain:

$$\frac{\ln(I) - \ln(I_l)}{\ln(I_g) - \ln(I_l)} = \frac{d_g}{d} \equiv \alpha^* \quad (3.4)$$

with α^* the chordal void-fraction. The significance of equation 3.4 is that the chordal void-fraction determined in this way is independent of I_0 (which depends on the source strength, the distance between source and detector and the detector efficiency), independent of μ_l and μ_g (which depend on the pressure and temperature) and independent of the attenuation in structural materials (which includes the fuel assembly casing but also the fuel rods). This means that no calibration is necessary; the two measurements made with a full and an empty fuel assembly can be considered as the calibration.

A consequence of this method is that at every location at which we want to measure the chordal void-fraction three measurements must be performed: one with the assembly filled with liquid, one with the assembly filled with vapour and one during operation of the facility. It is essential that the source and detector are located at exactly the same position for each of these three measurements. This means that each time a measurement at a new position is made the facility has to be shut down, emptied of the liquid, filled and finally started back up again. This is a much too cumbersome method. It is much more practical to measure the count rates at all the desired positions once for an empty assembly and once for a full assembly. Then a series of measurements can be made consecutively under different operating conditions. As mentioned at the beginning of this paragraph this does require that the source and detector can be placed accurately at the same position each time. This can be achieved with an accurate mechanical positioning system. Instead of building such a system for DESIRE we designed a simple positioning system and used data pre-processing of the measurement data to remove the positioning errors.

3.1.2 Subchannel void-fraction measurement technique

The usual method with which tomographic reconstruction is performed is the filtered backprojection technique (Tanke et al., 1991, Natterer, 1982). This is in essence an inverted Fourier transform in two dimensions. This method will not work in our case because of the irregularly shaped 'nodes' caused by the presence of the fuel rods in the assembly. Therefore a direct inversion method was used, which is feasible because of the limited number of nodes (49, each subchannel is considered as one node) in the problem.

The method works as follows. A large number of chordal void-fraction measurements is made at different angles and positions through the assembly at a specific height. For each

measurement the length of the gamma beam traveled in each node is calculated. These form a matrix \mathbf{A} in which the element $A[i,j]$ is the normalized distance of beam i traveled through node j . For a specific beam equation 3.2 can be written as:

$$I = I_0 e^{-(\mu_m d_m)} e^{-\sum_j (\mu_l(1-\alpha_j)d_j + \mu_g \alpha_j d_j)} \quad (3.5)$$

with α_j the average void-fraction in node j and d_j the length of the part of the beam in node j . Combining equations 3.5 and 3.4 gives an expression for the chordal void-fraction along beam i :

$$\alpha_i^* = \sum_j \alpha_j \frac{d_j}{d} = \sum_j \alpha_j A[i,j] \quad (3.6)$$

which can be written as the matrix equation

$$\vec{\alpha}^* = \mathbf{A} \cdot \vec{\alpha} \quad (3.7)$$

where the elements of $\vec{\alpha}^*$ are the measured chordal void-fractions and the elements of $\vec{\alpha}$ the average void-fractions in each subchannel. To perform the tomographic reconstruction this equation is inverted in the least-squares sense:

$$\vec{\alpha} = (\mathbf{A}^T \mathbf{\Omega} \mathbf{A})^{-1} \mathbf{A}^T \mathbf{\Omega} \vec{\alpha}^* \quad (3.8)$$

where $\mathbf{\Omega}$ is a weighting matrix, which is best chosen as the inverted covariance matrix of the measurement errors. However, the covariance matrix of the measurement errors is generally not known. In that case the identity matrix is used as the weighting matrix, which amounts to uniform weighting.

For the reconstruction to be possible the matrix $\mathbf{A}^T \mathbf{A}$ must be invertible. This means that there must be at least as many linearly independent chordal void-fraction measurements as there are subchannels. It is always possible to add an independent set of measurements by performing a scan under a different angle from the previous measurements. There are many different ways to have exactly as many independent measurements as there are subchannels, however it is more convenient to have more than this minimum number of measurements available. The precision of the reconstruction can be expressed as the covariance matrix of $\vec{\alpha}$ which is given by:

$$\text{cov}(\vec{\alpha}, \vec{\alpha}) = (\mathbf{A}^T \mathbf{\Omega} \mathbf{A})^{-1} \mathbf{A}^T \mathbf{\Omega} \mathbf{V} \mathbf{\Omega} \mathbf{A} (\mathbf{A}^T \mathbf{\Omega} \mathbf{A})^{-1} \quad (3.9)$$

where \mathbf{V} is the covariance matrix of the errors in the measured data.

3.1.3 Data pre-processing

The tomographic reconstruction via equation 3.8 is the last step of the procedure which starts with measurement of the countrate by the detector. Before the tomographic reconstruction can be made some operations are carried out on the measured data. This data pre-processing takes place in two steps.

Data acquisition and pre-processing step 1

- Place source and detector at the desired angle.
- Set the stepping motor in motion. The source and detector now scan the assembly at a constant speed.
- Sample the countrate with a short period (e.g. 10 ms). This period is a compromise between two considerations, which stem from the fact that we must take the logarithm of the countrate (equation 3.4). The first consideration is that there must always be at least one count in every sample, because we cannot take the logarithm of zero. This places a minimum on the sample rate. The second consideration arises from the fact that the void-fraction fluctuates, and the average of the logarithm is not equal to the logarithm of the average. This means that the sample rate must be high enough to accommodate the void-fraction fluctuations.
- Stop the stepping motor.
- Correct the data for dead time of the detector and for the background.
- Calculate the logarithm of the sampled counts.
- Average the logarithms over a number of samples. The number of samples over which is averaged depends on the stepping motor speed and the sample frequency. The combination of stepping motor speed, sample frequency and number of averaging points gives the number of lines per millimeter. The goal of this averaging is to reduce the number of data points that needs to be stored.
- Correct for the decay of the gamma source and compare with a calibration measurement to calculate the relative logarithm of the countrate. All measurements are taken relative to a calibration measurement to eliminate changes in the source activity or any other long-term changes in for example the electronics. The calibration measurement is taken with the γ -beam passing through an iron plate of 1 cm thickness which is comparable to the beam passing through an empty fuel assembly. This is done each day. The decay of the gamma-source from the moment of calibration is calculated using the half-life found in the literature (27.7 days for the Cr-51 source, see section 3.2.1).

The result of the first pre-processing step is a signal of the relative logarithm of the countrate as a function of position. A few examples of such a signal are given in figure 3.2 for different angles of the gamma beam to the fuel assembly. If the gamma-beam is at right angles to the fuel assembly the six rows of fuel rods are clearly visible. From left to right we start outside the fuel assembly (countrate is constant). Next the gamma beam passes through the fuel assembly casing (minimum in countrate). Then the countrate rises again and then falls as the gamma

beam passes the first row of fuel rods. This is repeated for each row of fuel rods; with one row having a higher count rate than the rest. This is the row that contains the hollow water rod.

At other angles the fuel rods are not so clearly distinguishable. It is, however, always clear where the fuel assembly casing begins. This fact is used in the second step of the data pre-processing. The difference in the countrate for an assembly filled with liquid and an assembly filled with vapour shows where the fuel assembly casing stops and the flow begins. Another important conclusion from this figure is that the positioning system is not sufficiently accurate, since the two curves at angle 0 show a small horizontal offset (about 0.5 mm in this case). This small offset has a large effect on the difference between the two curves, which leads to a large error in the chordal void-fraction. It is the purpose of the second pre-processing step to eliminate this error.

Pre-processing step 2

- Locate the fuel assembly casing from the signal generated by pre-processing step 1. This is most easily accomplished by looking at the point where the signal passes below some value. This value should be chosen so that the location of the beam at this point lies well away from the location where the lines for the full and empty assembly start to diverge (say 0.5). The exact crossing point is interpolated from the surrounding data points. This is done for both sides of the fuel assembly
- Scale the signal using the crossing points. The resulting signal crosses the assembly casing at 0 mm on one side. On the other side it depends on the angle; for 0° the crossing point lies at 54 mm, for 15° at $54/\cos(15^\circ)$ mm, etc.
- Resample the signal between the two crossing points by interpolation to obtain a limited number of chordal void-fractions for the tomographic reconstruction. The distance between two samples should be small enough so that each subchannel is passed by several beams for each angle to achieve a good 'coverage' of the subchannel. This averages out the effect of a non-homogeneous void-fraction distribution in each subchannel. Since the γ -beam has a width of 2 mm it is not useful to sample the signal with a much smaller sample distance.
- Calculate the chordal void-fraction at the sampled points using equation 3.4.

The two pre-processing steps are carried out for all angles at which a measurement was performed. The results are combined in one file which contains a list of entries consisting of *[angle, position, void-fraction]*. This is the input file to the tomographic reconstruction procedure. This procedure can handle an arbitrary number of entries of the above form. There is no constraint on the number or order of the entries. This means that it is possible to perform the reconstruction even if some of the measurements turned out later not to be successful.

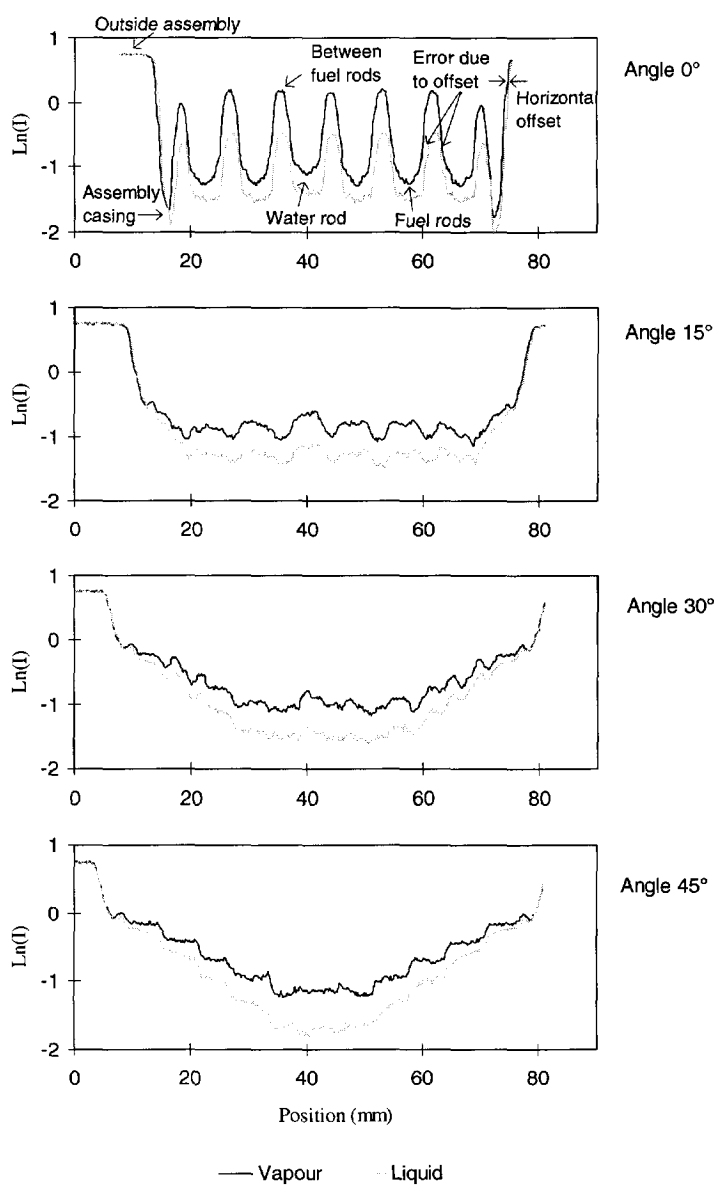


Figure 3.2 Signal traces from the gamma detector at different angles to the fuel assembly. Shown are the logarithm of the countrate as a function of the linear position for an assembly filled with liquid and an assembly filled with vapour. In the top figure the fuel rods are clearly visible.

3.1.4 Tomographic reconstruction

To perform the reconstruction we need to calculate the elements $A[i,j]$ which are the normalized distances of beam i traveled through node j . For this purpose the fuel assembly is modeled as a rectangular box of 54 by 54 mm containing the fuel rods with diameters of 6.35 mm at a pitch of 8.8 mm. Deviations of the real assembly from this model due to rod flexing are not accounted for; these deviations are much smaller than the size of the subchannels and can be neglected. The model of the fuel assembly is described by a collection of straight lines and circles in any order (these are called objects). The following steps are carried out for each beam:

- Calculate the intersection points of the beam with all objects. The result is a list of points.
- Sort the list of points in the x-coordinate or the y-coordinate. The result is a list of points lying sequentially on a straight line.
- Construct a line segment between each two adjacent points.
- Calculate the middle of each line segment.
- If the middle of the line segment lies inside a fuel rod or outside the fuel assembly it is rejected. Else the length of the line segment is calculated. It belongs to the subchannel j in which its middle is located.
- The normalized distances $A[i,j]$ are determined by dividing the line segment lengths by the total of the line segment lengths (excluding the rejected line segments).

Finally the void-fraction in the subchannels is calculated using equation 3.8.

3.2 The measurement set-up

3.2.1 The gamma source

The choice of the gamma source is mainly determined by the required energy of the gamma photons. This energy must be high enough so that the gammas penetrate the stainless steel casing but not so high that they are not attenuated in the Freon. The variance in the measured void-fraction is caused by the statistical nature of the radioactive decay of the gamma source. The number of counts measured in a time interval has a Poisson distribution, thus the variance of the countrate is given by:

$$\sigma_I^2 = \frac{I}{t} \quad (3.10)$$

with t the measuring time. If we consider only the error in I (I_g and I_l can be measured with longer measuring times, since this needs to be done only once) then the standard deviation in the chordal void-fraction follows from equation 3.4 and 3.10 as:

$$\sigma_{\alpha^*} = \frac{1}{\mu d \sqrt{I t}} \quad (3.11)$$

This equation shows that the error in the chordal void-fraction depends on the gamma energy (via the attenuation coefficient), on the length of the beam through the Freon and on the countrate. The countrate in turn is determined by the attenuation in the stainless steel casing, the Freon and the fuel rods; all of which are energy dependent.

In figure 3.3 the standard deviation of the void-fraction is shown for four cases as a function of the gamma energy, with $I_0=1000 \text{ s}^{-1}$ and a measuring time of 1 second. As can be seen there is a large difference for a gamma beam traveling between the fuel rods opposed to a beam going through the fuel rods. The void-fraction has a relatively smaller effect, but still clearly visible. The optimum gamma energy is different for all four cases, but it can be seen that the error is not very sensitive to an increase in gamma energy. The conclusion from this figure is that the optimal gamma energy lies around 300 keV. Higher energies will not have much impact on the precision, but it must be noted that for the shielding of the gamma-source low energies are desirable.

Two isotopes which emit gamma photons around 300 keV are Ba-133 (81, 303, 356 keV) and Cr-51 (320 keV). Besides the energy of the gamma photons other considerations which determine the choice of isotope are half-life and costs. The half-life of Ba-133 is 10.5 years, while for Cr-51 it is 27.7 days. Despite the shorter half-life it was decided to use Cr-51 because this isotope could be produced cheaply in our research reactor by irradiation of a piece of

Chromium. This 2 MWth reactor has several irradiation facilities. The one that was used has a thermal neutron flux of $6.5 \cdot 10^{12} \text{ s}^{-1} \text{ cm}^{-2}$. Irradiation of a piece of Chromium of $2 \times 8 \times 8$ mm during 10 reactor days produced an activity of 276 mCi. To allow for the decay of short-lived isotopes the piece is left to 'cool' down for two days. These short-lived isotopes are formed by activation of small quantities of impurities in the Chromium.

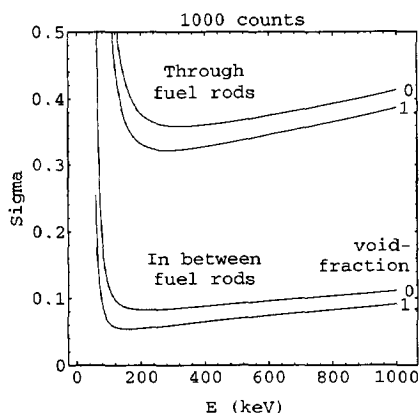


Figure 3.3 The standard deviation in the chordal void-fraction as a function of gamma photon energy, for void-fractions of 0% and 100%.

3.2.2 The set-up

The gamma source and detector are mounted on a translation table which is driven by a stepping motor. This translation table is mounted on a rotation table which can be rotated by hand (see figure 3.4). The whole

system can be moved up and down along the assembly.

The source is placed in the middle of a lead cylinder with a length of 10 cm and a diameter of 10 cm. A 5 cm long collimator with cross-section of 2 mm horizontal and 8 mm vertical can be rotated in front of the source. At the detector side a shorter collimator of 1 cm with the same cross-section is placed in front of the detector. These two collimators define a narrow beam of 2 by 8 mm.

The detector is a scintillation detector with a BGO (bismuth germanate, $\text{Bi}_4\text{Ge}_3\text{O}_{12}$) crystal as the scintillator. The light flashes from the scintillator are converted to a current and amplified in a photo-multiplier tube. The pulses from the photo-multiplier tube are amplified further, shaped and finally analyzed. The height of the pulses is a direct measure for the amount of energy that was deposited in the scintillator crystal by the gamma photon. If the interaction of the gamma photon takes place via the photo-electric effect all of its energy is deposited in the crystal. This results in the so-called photopeak in the pulse-height spectrum. On the other hand if the interaction takes place via Compton scattering only a portion of the energy is deposited. Since we only count the pulses in the photopeak these photons are lost to our measurement, increasing the statistical error in the void-fraction. More serious is the fact that Compton pulses from photons with a higher energy can fall inside the 320 keV photopeak. These higher energy photons are emitted by activated contaminations in the Chromium piece. Since the linear attenuation coefficient is different for these gammas this will result in a systematic error in the void-fraction measurement.

For this reason BGO was chosen as a scintillator. BGO has a high density (7.13 g/cm^3) making it a very efficient gamma-ray absorber. Due to the high Z value the ratio of photo-to-Compton absorption is very high. This means that this material has a high photopeak-efficiency, which is the content of the photo-peak relative to the total absorption. For 320 keV photons the photopeak efficiency for a BGO crystal of 38 mm height and 38 mm diameter is 70% (NaI, another popular scintillator only has a photopeak efficiency of 35% at this energy and crystal size).

The pulses from the amplifier are first passed through a spectrum stabilizer. This ensures that the photopeak does not drift as a result of drift in the electronics or in the high voltage for the photo-multiplier tube. A single channel analyzer converts the pulses that fall within a window placed around the photopeak to standard pulses which are counted by a data-acquisition board in a PC.

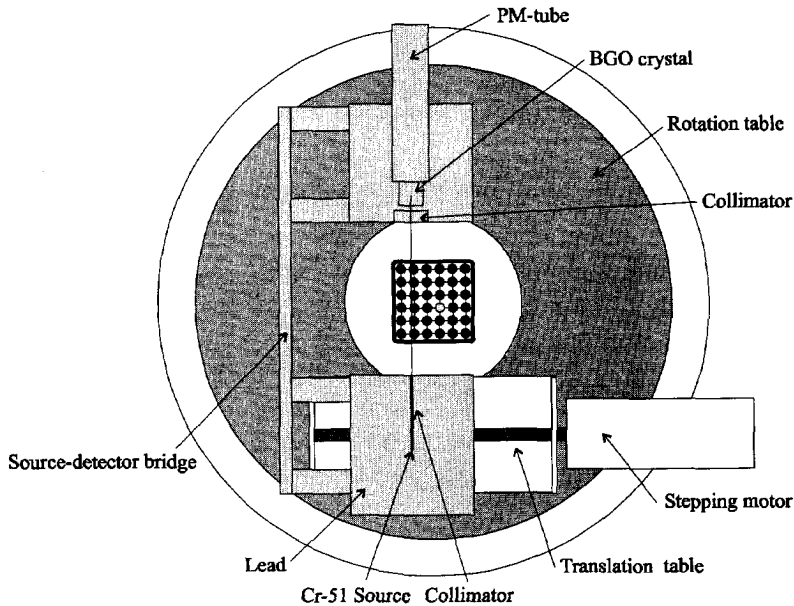


Figure 3.4 The gamma-transmission set-up. The rotation table can be moved by hand, the translation table is moved by a stepping motor.

3.2.3 Test measurements

To test the tomographic measurement procedure four test measurements were done in which different combinations of fuel rods were heated, while the rest was left unheated. This should produce locally a high void-fraction for the subchannels located next to the heated rods. The results can be seen in figure 3.5. The fuel rods which were heated are indicated in the figure. The void-fraction is indicated as a gray shade, from black for pure liquid to white for a void-fraction of 80%.

The void-fraction can be seen to be directly related to the number of heated fuel rods surrounding the subchannels. Since the measurements were done at the top of the fuel assembly some drift of vapour into adjacent subchannels, which do not have any heated fuel rods, is visible.

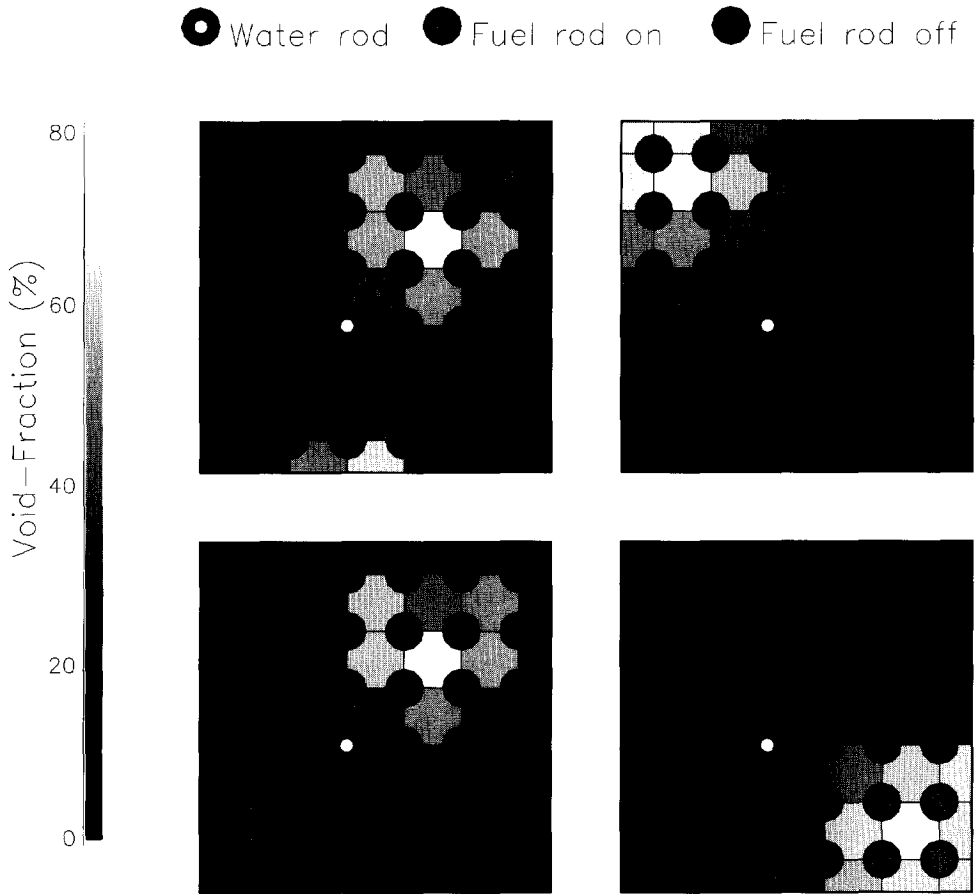


Figure 3.5 Void-fraction test measurements. Shown are four cases where some fuel rods were heated (gray rods in figure) and other rods were left unheated (black rods). The void-fraction is shown as a gray scale for each subchannel. The tomographic reconstruction gives the expected results: the more fuel rods surrounding a subchannel are heated the higher the void-fraction is.

3.2.4 Error analysis

There are many conceivable sources for error in the reconstructed void-fraction. Some of the errors can be corrected for, some can be calculated, but others can only be speculated upon without a detailed further study.

- a) Errors due to the Poisson statistics of the gamma source.

Equation 3.9 can be used to determine how the error in the measured chordal void-fraction affects the error in the reconstructed void-fraction. The error in the chordal void-fraction due to the Poisson statistics is determined by the number of counts, the void-fraction and the location of the gamma-beam (see figure 3.3). I_0 was typically 10.000. This leads to an error varying from 2% to 12 %. Using 12 angles and a total of more than 700 chordal void-fractions this gives an error in the order of 0.4% in the reconstructed void-fraction for the center subchannel, about 1 % in the wall subchannels and 2% in the corner subchannels (absolute errors).

- b) Errors due to counting of gamma photons of higher energy which give pulses in the 320 keV photo-peak via Compton interaction with BGO.

It was found that there were impurities in the Chromium which became activated when the piece was irradiated. As a result gamma photons of various energies were emitted. Since the attenuation coefficient is different for these gamma photons they must not be counted by the detector. This cannot be avoided for those gamma photons who undergo a Compton interaction in the scintillator crystal resulting in a pulse that falls in the 320 keV photopeak. This is the reason that BGO was chosen as a scintillator crystal; it has a very good photopeak efficiency. Also it was found that letting the Chromium cool off some extra few days after irradiation substantially reduced the problem.

- c) Background and detector dead time

The background countrate was measured and subtracted from the measurements. It has a typical value of about 50 counts per second. This relatively high value can be reduced by shielding the detector. The correction for the dead time of the detector was very small since the count rates were limited.

- d) Error in positioning of the source-detector

This problem was discussed in section 3.1.3. It has been solved using the data pre-processing.

e) Fuel rod bending

In the reconstruction procedure the lengths of the gamma rays passing through the subchannels is calculated. In this calculation the fuel rods are assumed to be at their correct position. It is however clear from visual inspection that the fuel rods are not perfectly straight, so that their position varies with height. If a fuel rod is displaced into a certain subchannel, then the void-fraction in that subchannel will be underpredicted. Fortunately, since this means that the fuel rod is displaced out of the subchannel opposite of this subchannel the void-fraction in this subchannel will be overpredicted. In general these errors will almost cancel, and the average void-fraction is not affected by fuel rod bending.

f) deviations of the real geometry from the assumed geometry

The walls of the fuel assembly casing are not exactly flat, due to the high pressure inside. Also the corners of the fuel assembly casing are rounded. These effects are not accounted for in the reconstruction procedure. Especially for the corner subchannels, which have a small area, this has a large effect. This in combination with the problem of measuring very close to the fuel assembly casing makes the measurement in the corner subchannels less reliable than in the other subchannels.

3.3 Two-phase flow models

In DESIRE four regions can be identified which all require a different treatment for the calculation of the flow quality and the void-fraction: the subcooled boiling region, the saturated flow region, the riser and the downcomer. In table 3.1 the steps needed to calculate the void-fraction in these four regions are given.

The thermodynamic equilibrium quality is straightforward to calculate in the assembly and riser:

$$x_{eq}(z) = -\frac{c_l T_{sub}}{h_{ev}} + \frac{1}{h_{ev} \Phi} \int_0^z P'(z) dz \quad (3.12)$$

with P' the power per unit length. In the downcomer the thermodynamic equilibrium quality depends on the carry-under. There is no straightforward way to calculate the carry-under. This subject is discussed in chapter 4.

Subcooled boiling region	Saturated flow region	Riser	Downcomer
<i>Operating conditions (power, subcooling, flow rate)</i>			
heat balance	heat balance	heat balance	carry-under
<i>Thermodynamic equilibrium quality (x_{eq})</i>			
subcooled boiling model	identity	identity	identity
<i>Flow quality (x)</i>			
drift-flux model Dix's correlation	drift-flux model Dix's correlation	drift-flux model fit to data	slip model fit to data
<i>Void-fraction (α)</i>			

Table 3.1 The path from operating conditions to void-fraction for the four different regions.

The step from thermodynamic equilibrium quality to flow quality is trivial in all regions except in the subcooled boiling region. In chapter 2, where the definitions of the two qualities were given, we already saw that the flow quality stays zero upto the departure point and becomes equal to the thermodynamic equilibrium quality at the equilibrium point (this point also demarks the boundary between the subcooled boiling region and the saturated flow region). In between these two points the flow quality is described using a profile-fit method. This fit gives the flow quality as a function of the equilibrium quality and the equilibrium quality at the departure point (equation 2.12). A correlation for the equilibrium quality at the departure point is given by (Saha and Zuber, 1974):

$$x_{eq,d} = -154 \frac{\dot{q}''}{\dot{m}'' h_{ev}} \quad \text{for } N_{Pe} > 7 \cdot 10^4 \quad (3.13)$$

with \dot{q}'' the wall heat flux. The Péclet number is given by equation 2.13, and is equal to about $150 \cdot 10^3$ under nominal conditions for DESIRE.

Relation 3.13 was derived using local hydrodynamic detachment considerations (Saha and Zuber, 1974). It is assumed that the rate of evaporation at the wall is proportional to the heat flux, whereas the rate of condensation is proportional to the subcooling. Also, at high mass-fluxes, the detachment of bubbles from the rod walls are hydrodynamically controlled. So the quality at the departure point depends only on local parameters, and the power profile is irrelevant. However, the actual position of the departure point does depend on the power profile, since the departure point is given as the point where the subcooling reaches some value. The actual height at which this happens depends on the development of the subcooling as a function of height. Although this height is not needed to calculate the void-fraction it is

important for the dynamics of the loop (chapter 5 and 6), so we will take the opportunity to determine it.

We rewrite equation 3.13 using equation 2.1 as:

$$T_{sat} - T(z) = 154 \frac{\dot{q}''(z)}{\dot{m}'' c_l} \quad (3.14)$$

where both the heat-flux and the temperature are a function of height. In figure 3.6 the left-hand and right-hand terms of this equation are plotted for nominal DESIRE conditions for three power profiles: flat, chopped cosine and cosine. The departure point is located at the crossing of the two lines. In the case of the flat power profile the two lines do not meet. This is because the subcooling predicted by the model at the departure point (5.4 °C) is larger than the subcooling at the inlet of the assembly (2 °C), so the boiling starts directly at the inlet of the assembly.

The situation is different for the cosine power profile. Here both the predicted subcooling at the departure point as well as the actual subcooling are a function of the height. They cross at a height of about 6 cm. It is also interesting to note that the position of the departure point is much less sensitive to the power or the subcooling than in the flat power profile case (if they were to cross with a higher subcooling). This is due to the large angle at which the two lines cross. This means that the boiling boundary dynamics are different for the flat power profile and the cosine power profile (see chapter 5).

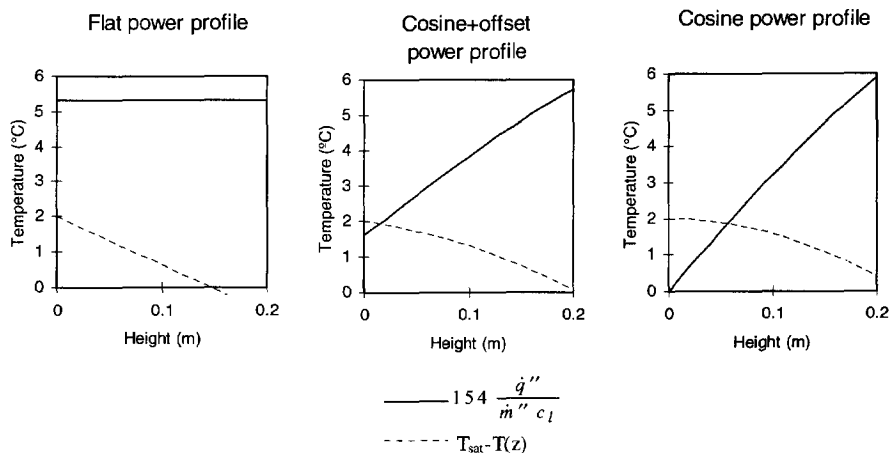


Figure 3.6 The left and right terms of equation 3.14 as a function of height for three power profiles. The departure point is located at the crossing point of the two lines. (power 22 kW, flow rate 2 kg/s, subcooling 2 °C)

In DESIRE the power profile is a combination of the flat and the cosine power profile. This means that it is possible for the boiling to start directly at the bottom as in the left of figure 3.6, but also that the boiling boundary dynamics is influenced by the slope of the power as in the right of figure 3.6.

The last step in table 3.1 is the step from flow quality to void-fraction. For this step a void-quality relation is used. The void-quality relations for the homogeneous equilibrium model and the drift-flux model were already given in chapter 2 (equations 2.6 and 2.7). The drift-flux model is used in all regions except in the downcomer. In the downcomer a slip model is used instead:

$$\alpha = \frac{x}{x + \frac{v_g}{v_l} \frac{\rho_g}{\rho_l} (1-x)} \quad (3.15)$$

where v_g/v_l is the slip ratio. The reason for using this model instead of the drift-flux model will be given in section 3.5.2.

The drift-flux model contains two parameters: the distribution parameter and the local drift flux. There are many correlations available which give these parameters (Maier and Coddington, 1997). Dix's model was developed for rod bundles and should be applicable to DESIRE. It is given by:

$$C_o = \frac{j_g}{j} \left(1 + \left(\frac{j}{j_g} - 1 \right) \left(\frac{\rho_g}{\rho_l} \right)^{0.1} \right) \quad (3.16)$$

$$v_{gj} = 2.9 \left(\frac{g \sigma \Delta \rho}{\rho_l^2} \right)^{1/4} \quad (3.17)$$

For a given pressure the local drift flux in this model is a constant. For nominal pressure in DESIRE its value is 0.24 m/s.

3.4 Void-fraction measurements in the assembly

A total of nine measurement runs were performed. During each run the subchannel void-fractions were measured at six heights along the assembly (at 16, 28, 40, 52, 64 and 76 cm). The spacers are located at 25, 49 and 73 cm, so the measurements were taken at least 3 cm downstream of the spacers. Local disturbances of the void-fraction due to the spacers are not to be expected at this distance. Takenaka used neutron radiography to measure the void-fraction in the region around the spacers. He found the void-fraction decreased by some 4

percentage points at the spacer itself, but the void-fraction downstream of the spacer returned to an equilibrium value within 1 cm (Takenaka et al. 1996).

Table 3.2 gives the operating conditions for the measurement runs. The pressure during all the runs was nominal (11.6 bar). The measurements are divided into three series (A, B and C in the table). The first series entailed a variation of the power at constant flow rate. The second series consists of one measurement at reduced flow rate. The third series is a variation of the power profile, going from flat to tilted.

Measurement Run	Power (kW)	Flow (kg/s)	Subcooling (°C)	Power profile
A1	15	1.6	0.5	flat
A2	30	1.6	0.8	flat
A3	40	1.6	1.0	flat
B	22	1.16	1.7	flat
C1	22	1.6	1.0	flat
C2	22	1.6	1.0	tilted (550-710) Watt/rod
C3	22	1.6	1.0	tilted (470-780) Watt/rod
C4	22	1.6	1.0	tilted (380-880) Watt/rod
C5	22	1.6	1.0	tilted (300-970) Watt/rod

Table 3.2. DESIRE operating conditions during the measurements

In figures 3.7 a and b the results are shown. The 35 fuel rods are shown as black circles and the water rod as a black circle with a white dot inside. Some general features apparent from these figures are the presence of the water rod, where the void-fraction is lower than average, and the effect at the walls of the fuel assembly, where the void-fraction also is lower than average. The exact numerical values of the measured void-fractions are given in the appendix.

3.4.1 The cross-sectional average void-fraction

Figure 3.8 shows the cross-sectional average void-fraction compared to two models: the homogeneous model without subcooled boiling and the drift-flux model with subcooled boiling using Dix's correlation. The agreement with the latter model is excellent. But it is instructive to give a qualitative comparison of the measurements with the homogeneous model.

At the lowest measuring point of 16 cm the measured void-fraction is much higher than the void-fraction according to the homogeneous model. This is caused by subcooled boiling. The thermodynamic equilibrium quality at this point is almost zero. Between 16 cm and 28 cm the thermodynamic equilibrium quality is positive. At some point thermodynamic equilibrium will be reached and the flow quality will be equal to the thermodynamic equilibrium quality.

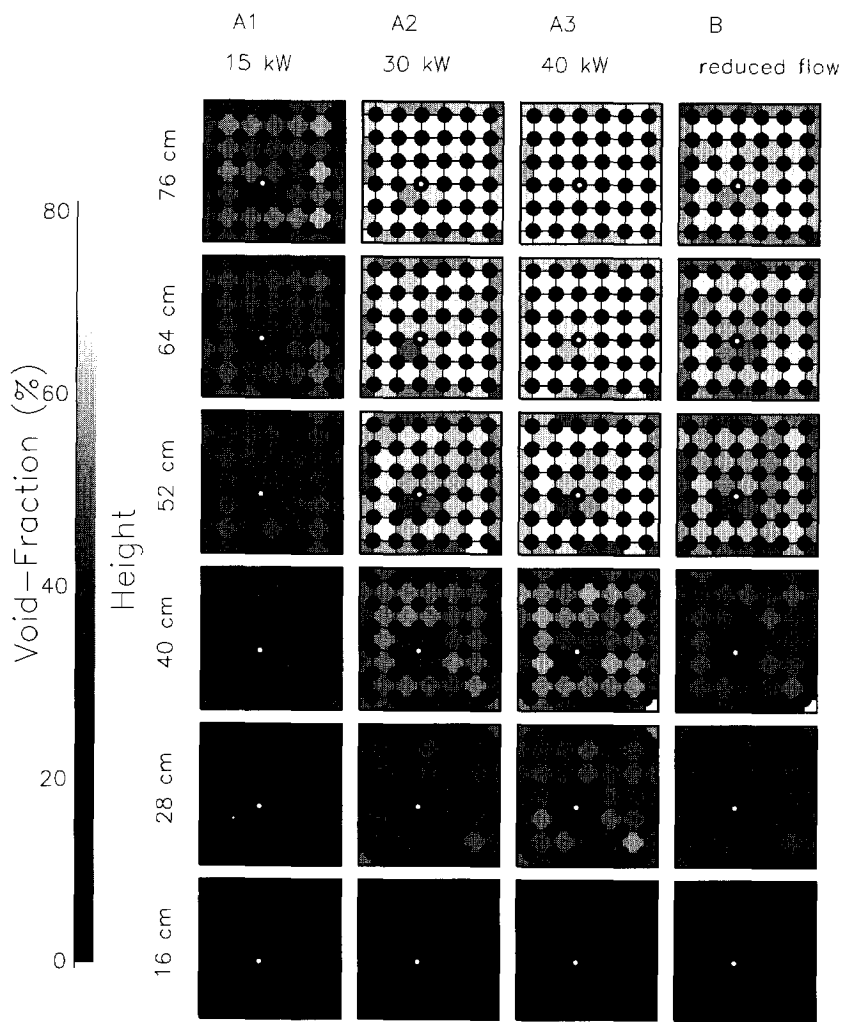


Figure 3.7 a Subchannel void-fractions at six heights for different measurement runs.

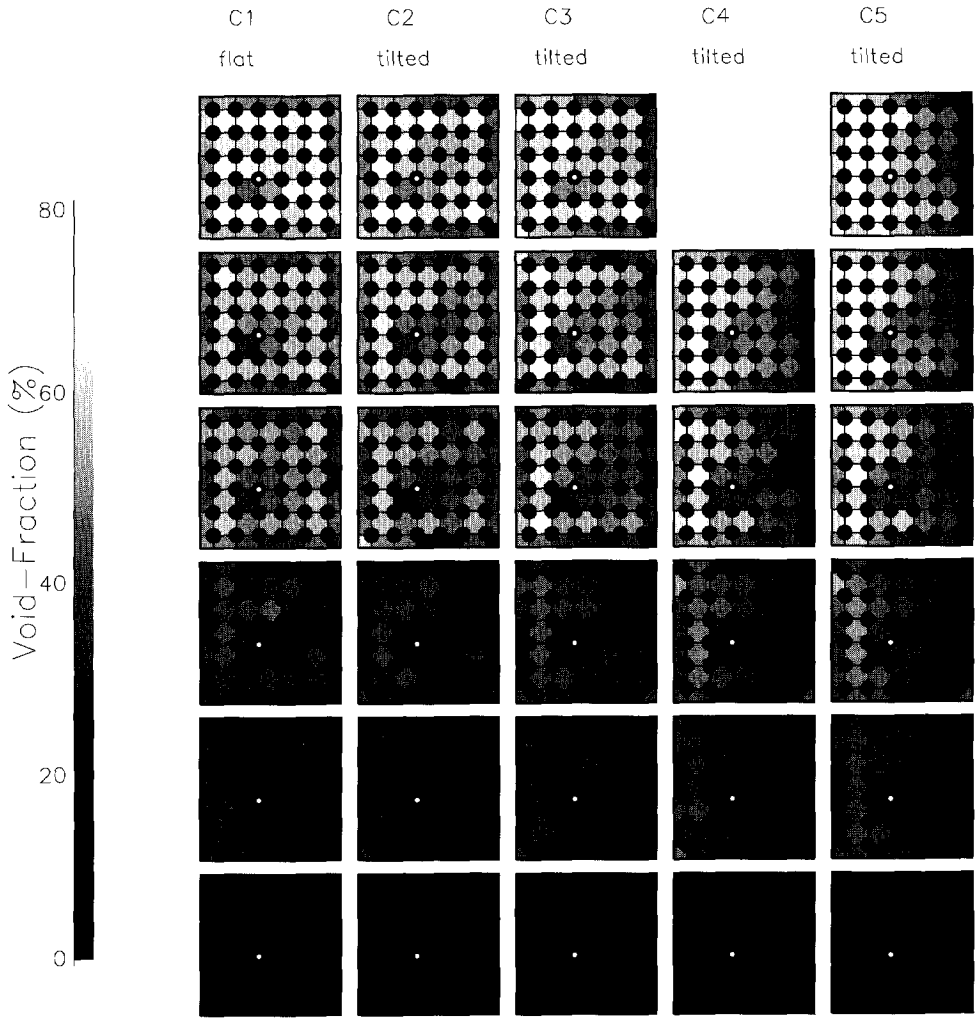


Figure 3.7 b Subchannel void-fractions at six heights for different measurement runs.

At the point where thermodynamic equilibrium is reached the vapour will still be concentrated near the rod walls. Since the velocity of the flow is lower at this location the distribution parameter will be smaller than 1. Also the bubbles will still be small and the local drift velocity will be small. In such a case the drift-flux model predicts a void-fraction which is higher than the void-fraction in the homogeneous model. This is the case between the first two measuring points. As the flow develops the bubbles move into the center of the subchannels. The distribution parameter becomes larger than 1 and the local drift velocity increases. These two effects cause the void-fraction to be lower than the void-fraction according to the homogeneous model.

In all measurements there is a dip in the void-fraction at the third measurement point at a height of 40 cm. The origin of this dip is unknown, but one of the following factors could play a role:

- *spacer effect:* The second and fourth measurements points lie just 3 cm above the first and second spacer respectively. If the spacer causes an increase in the void-fraction just downstream this would partly explain the dip in the third measurement point which does not lie in the neighborhood of a spacer.
- *Error in the calibration measurement:* For all the measurement series the same calibration measurements of I_l and I_g in equation 3.4 are used. Although these measurement were carried out with care a measurement error at the third measurement height would effect all measurement series in the same way.
- *Flow pattern transition:* A transition from bubbly flow to a churn or annular like flow would decrease the void-fraction after the transition. The maximum possible void-fraction for a bubbly flow lies at about 30 %. This could explain the dip in most measurements. However, this hypothetical flow pattern transition takes place between the second and third measurement point in all measurements, irrespective of the void-fraction in this region which varies from ± 25 % to ± 40 %. This makes the flow pattern transition as an explanation for the dip not fully convincing. Still, there is evidence of a flow pattern transition from measurements of the void-fraction distribution within the subchannels (see section 3.4.4). This transition also occurs at a height between 30 and 40 cm, irrespective of the void-fraction.

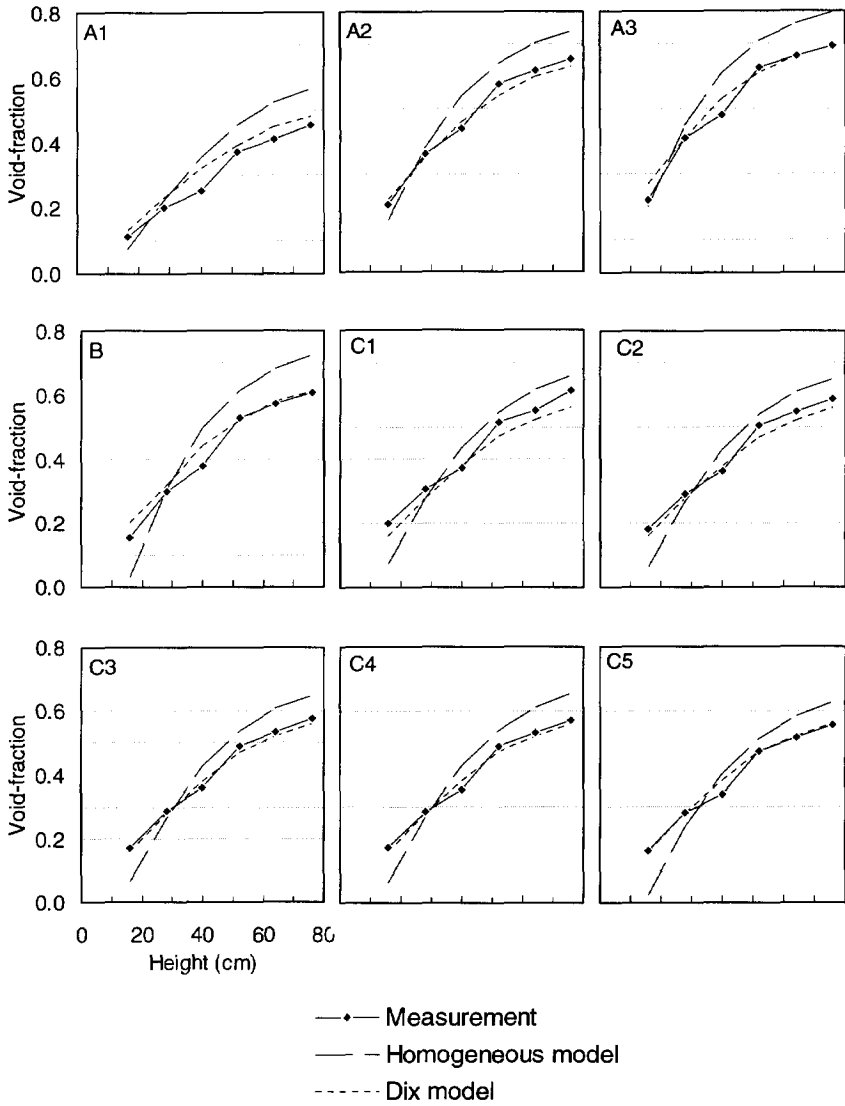


Figure 3.8 Average void-fraction as a function of height for all measurement runs compared with the homogeneous model and the drift-flux model using Dix's correlation.

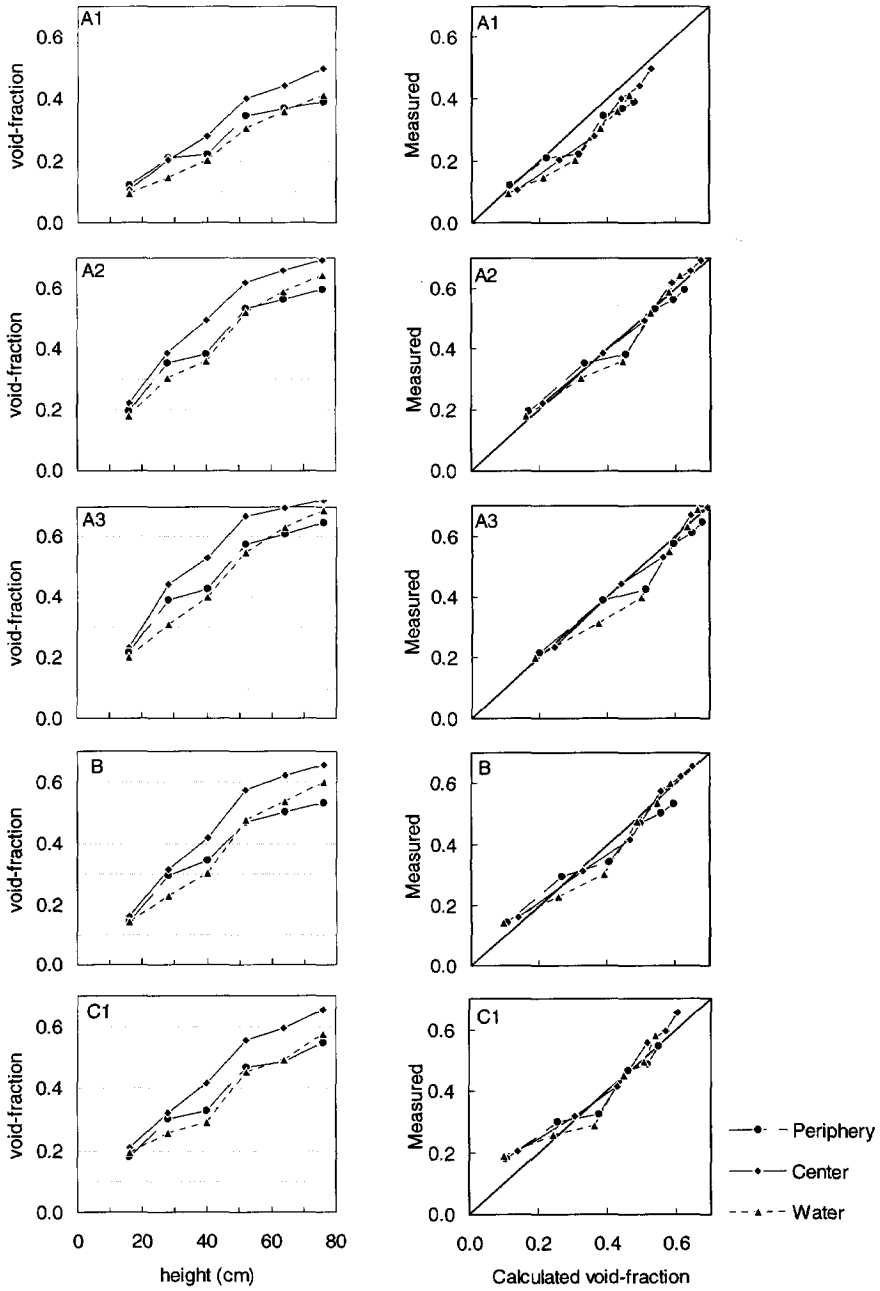


Figure 3.9 Void-fraction in the different subchannels types as a function of height (left) and compared with the drift-flux model in a scatter plot (right).

3.4.2 *The void-fraction in different subchannels*

There are several types of subchannel in the fuel assembly. We can identify subchannels at the corner, at the wall and center subchannels. These all have a different geometry. Among the center subchannels there are four subchannels next to the water rod. The void-fraction development in these different types of subchannel is shown in figure 3.9, where the corner and wall subchannels have been grouped into 1 group (called the periphery).

In the left column of figure 3.9 the development of these void-fractions along the height of the subchannel is shown. This must be compared with the power that goes into each channel. It is assumed that one-quarter of the power produced by each fuel rod surrounding the subchannel goes into that subchannel. The power/flow-area ratio of the peripheral subchannels is 82% of the power/flow-area ratio of the center subchannels. One striking fact is that at the bottom of the assembly the void-fractions in the center and peripheral subchannels are about equal, despite the different power/flow-area ratios. It may be that the flow rate in the peripheral subchannels is smaller. Above 40 cm height the void-fraction in the peripheral subchannels is smaller than in the center subchannels.

To determine if void transport between the subchannel takes place we apply the drift-flux model to each subchannel individually. These calculated results are compared with the measurement results in a scatter plot in the right column of figure 3.9. If there were void transport taking place the lines in this scatter plot would diverge for the different types of subchannel. In all plots a slight divergence can be seen at higher void-fractions. The measured void-fraction for the periphery consistently lies below the line for the center subchannels which indicates transport of void from the periphery to the center. The differences however are quite small. Another indication of void transport from the periphery to the center is that the void-fraction of the center subchannels adjacent to the wall subchannels is larger than the void-fraction in the other center subchannels (see figure 3.7 and the curve for C1 in figure 3.10, which has a maximum at the second and sixth row).

Unlike the peripheral subchannels the subchannels next to the water rod have the same geometry as the other center subchannels. The lines for the center and water subchannels in the scatter plots do not diverge. Even at higher void-fractions the two lines lie close to each other. Thus there seems to be little transport of vapour from the center into the water subchannels.

3.4.3 *Void-fraction with a tilted power profile*

Net lateral void transport, if it were to occur, should also be visible in the measurement with the tilted power profile. In figure 3.10 the void-fraction averaged over subchannels of equal power (again it is assumed that one-fourth of the power of each fuel rod forming the subchannel is put into that subchannel) is shown at the six measuring heights. In figure 3.11 a scatter plot is shown comparing the measured void-fraction to the calculated void-fraction using the drift-flux model and the assumption of no vapour transport between subchannels. As can be seen the agreement between the two is good.

If vapour is transported from subchannels with a higher void-fraction to subchannels with a lower void-fraction this would have an equalizing effect on the measured void-fraction. The slope of the lines in figure 3.11 connecting all measurement points at the same height will then decrease. This is not the case, so it is concluded that on an assembly-wide basis the void-fraction follows the power profile.

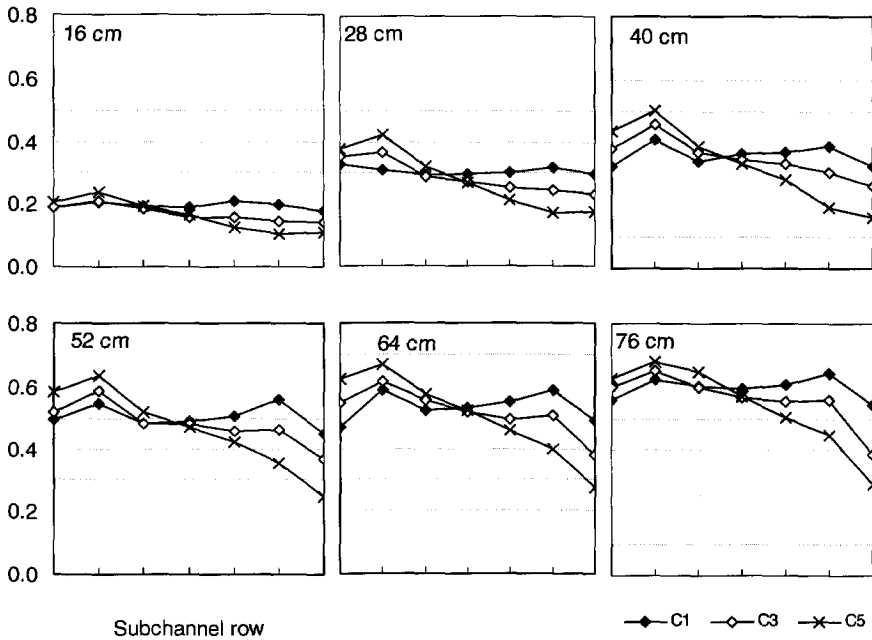


Figure 3.10 The effect of the tilted power profile on the lateral void-fraction distribution. Shown is the void-fraction for each subchannel row (on the x-axis, averaged over the 7 subchannels in each row); all the subchannels in each row receive an equal amount of heat from the fuel rods. The power decreases linearly from left to right.

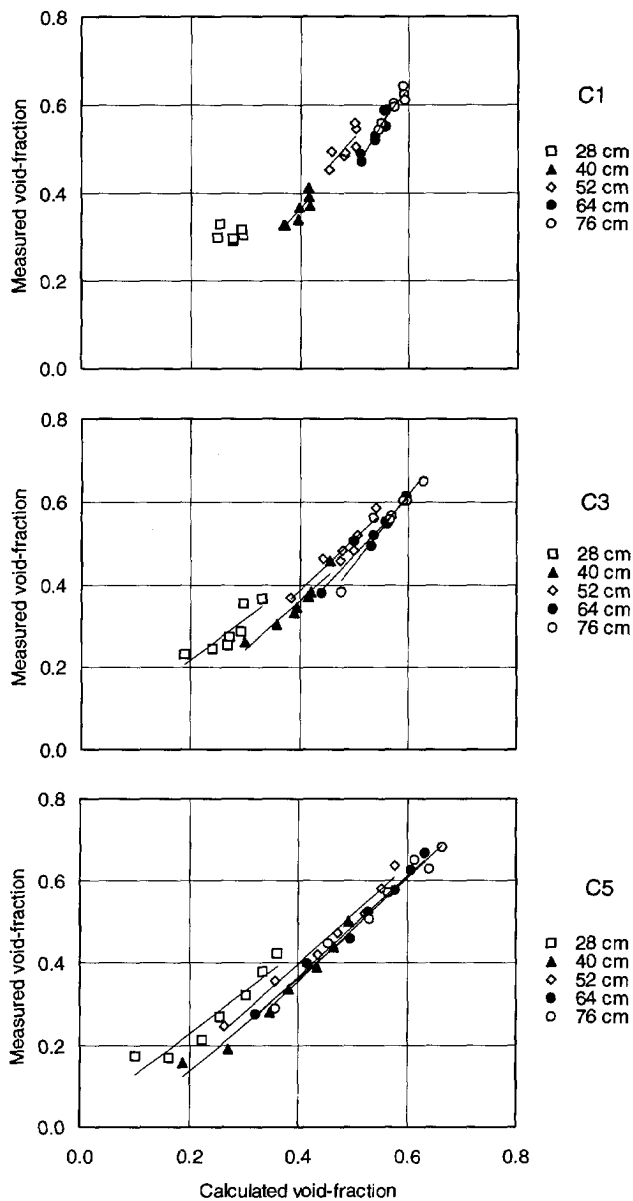


Figure 3.11 Scatter plot of measured versus calculated void-fractions using the drift-flux model and Dix's correlation.

3.4.4 Void-fraction distribution within the subchannels

All the results presented up to this point were based on the tomographic reconstruction of the void-fraction in the subchannels. In this reconstruction it is assumed that the void-fraction in each subchannel is distributed homogeneously. This is obviously a wrong assumption, since the bubbles at the bottom are created at the rod walls while in a developed flow the vapour is concentrated in the center. Since each subchannel is traversed by many gamma beams at different angles and positions all points within each subchannel are equally 'sampled', so the effect of the non-homogeneous distribution is averaged out in the result.

Still, by examining the signal from the detector more closely, signs of this non-homogeneous distribution could be found. This is most clearly illustrated by performing a simple comparison between the chordal void-fraction as measured exactly between the fuel rods or as measured exactly through the fuel rods (see figure 3.1). One of these lines probes only the gap region between the rods. The other probes both the gap and the center region of the subchannels. The difference between these two reflects the difference of void-fraction in the bulk of the flow in the center of the subchannel and in the flow close to the fuel rods. The results are shown in figure 3.12. A clear transition can be seen in the figure, where the void-fraction in the bulk of the flow increases more rapidly than the void-fraction near the fuel rods. This is indicative of a transition from bubbly flow to annular flow in each subchannel. As discussed in section 3.4.1 this transition could be the reason for the dip in the average void-fraction at the third measuring point at a height of 40 cm in figure 3.8.

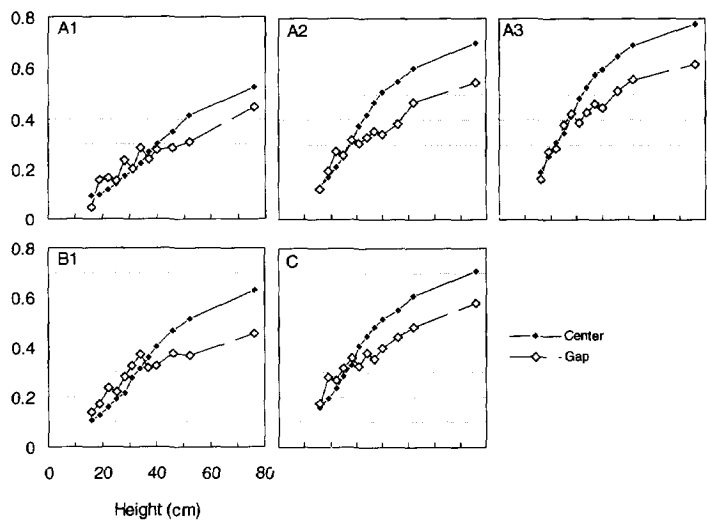


Figure 3.12 Chordal void-fraction along the two beams shown in figure 3.1 as a function of the height.

3.5 Void-fraction measurements in riser and downcomer

Besides the void-fraction measurements in the fuel assembly some measurements in the riser and in the downcomer were performed. These measurements are important for the model of the natural circulation to be presented in chapter 4. They were performed with a gamma-transmission set-up using an Am-241 source. The source was collimated with a circular collimator with a diameter of 10 mm. Measurements were done with different power and flow rates and compared with two-phase flow models.

3.5.1 Void-fraction in the riser

In figure 3.13 the results of the measurement of the void-fraction in the riser are shown. The power and flow rate at which the measurements were performed are shown on the left. On the right the measured void-fraction is compared with the void-fraction calculated using the drift-flux model and Dix's correlation. The agreement between the two is reasonable, although the void-fraction is underpredicted at higher void-fraction. A direct fit of C_o and v_{gj} gives better results. The values found for C_o and v_{gj} are $C_o = 1.06$ and $v_{gj} = 0.14$ m/s. It is not surprising that Dix's correlation performs better in the fuel assembly than in the riser since this correlation was derived specifically from rod-bundle data.

A comparison is also made with the Chexal-Lellouche correlation which is a recent correlation designed to cover a large range of operating conditions (Chexal-Lellouche, 1992). It is also capable of handling different fluid types such as the refrigerants. From the comparison it can be seen that there is a linear relationship with offset between the Chexal-Lellouche model and the measurements. The cause for this offset is unknown, although it is possible that it is caused by a measurement error in either I_t or I_g . The measurement of the void-fraction in the riser was more difficult to perform than the measurement of the void-fraction in the assembly because the gamma beam also passes through the flow in the downcomer which can influence the measurements. Also only the chordal void-fraction was measured, which can be biased compared to the cross-sectional void-fraction.

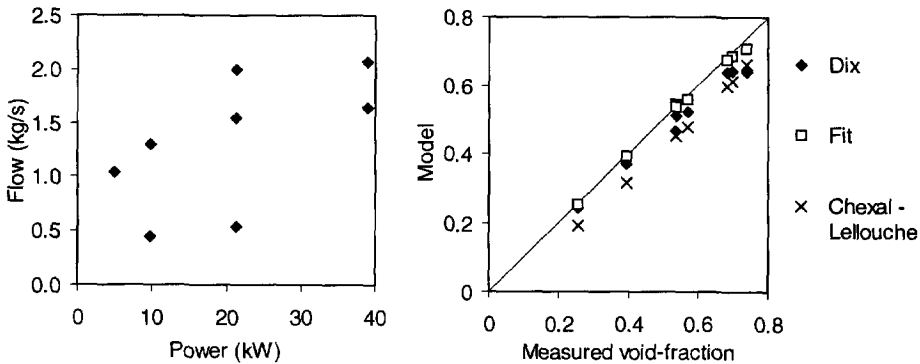


Figure 3.13 Void-fraction in the riser under various operating conditions. The left figure is a scatter plot of the measurement points in the power/flow plane. The right figure compares the measured values with calculated values using the drift-flux model and Dix's and Chexal-Lellouche's correlations and a drift-flux model with v_{gj} and C_o fitted to the data.

3.5.2 Void-fraction in the downcomer

The void-fraction in the downcomer was measured in the same way as the void-fraction in the riser. The flow quality in the downcomer depends on the carry-under. It can be calculated from flow rate and temperature measurements in DESIRE using the static flow model to be presented in chapter 4. The two-phase flow in the downcomer is different from the other regions in the loop because the liquid flows downwards instead of upwards. In principle the drift-flux model can also be used in co-current downward flow. The local drift velocity then becomes negative. A result of this is that equation 2.7 can become singular at a sufficiently low volumetric flux. This occurs when the rise velocity of the bubbles becomes as large as the downward flow velocity. The bubbles will have a zero net velocity, thus the flow quality will be zero while the void-fraction can be quite large. If the volumetric flux is even lower then no vapour will be dragged into the downcomer and the carry-under will be zero.

While this may be physically realistic it leads to wildly fluctuating predictions of the void-fraction in the downcomer whenever the flow velocity approaches the bubble rise velocity. Instead of the drift-flux model a slip model is used to calculate the void-fraction (equation 3.15).

Figure 3.14 shows the quality-void relation of the measured data, for the homogeneous flow model (slip ratio =1) and for the slip model with a fitted slip ratio of 0.5. The global agreement between measured data and the slip model is quite good, although there is some scatter and the model overestimates the void-fraction at low qualities. Actually the measurement points seem

to cross the x-axis at a positive quality. Since this is physically impossible it indicates there is a small measurement error. The most probable cause for this error are the thermocouples which are used to calculate the quality in the downcomer. An error of $0.5\text{ }^{\circ}\text{C}$ corresponds roughly to a quality difference of 0.004 which is about the point where the measurements cross the x-axis.

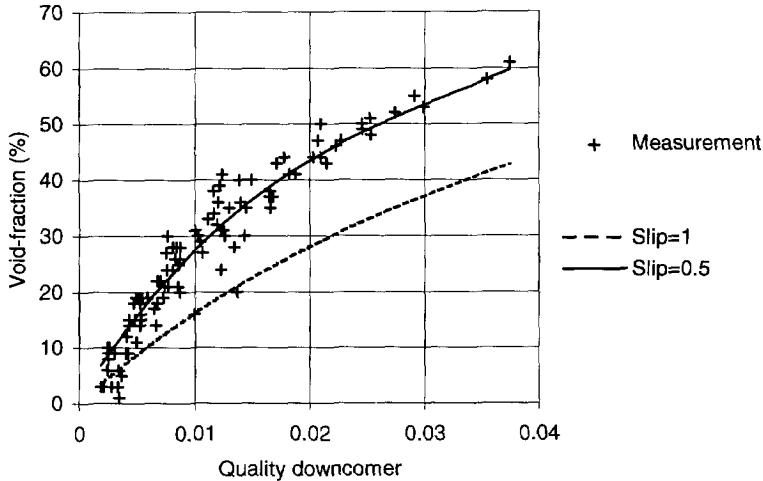


Figure 3.14 Measured void-quality relation in the downcomer above the feedwater sparger compared with the homogeneous model (slip=1) and a void-slip model with slip=0.5.

3.6 Conclusions

A measurement technique was developed for the measurement of the void-fraction on a subchannel basis. The technique is based on the γ -attenuation technique and uses a tomographic reconstruction procedure to calculate the void-fraction in the subchannels from the measured chordal void-fractions. The mechanical design of the system is fairly simple. Errors in the positioning of the gamma beam are removed by pre-processing of the measured signals.

The results are compared to the homogeneous equilibrium model and a combination of a subcooled boiling model and the drift-flux model using Dix's correlation for the distribution parameter and the local drift velocity. The agreement of the measured data with this second model is good.

The void-fraction in the peripheral subchannels and water subchannels is lower than the other subchannels. To investigate whether void-drift phenomena were responsible for this effect the drift-flux model was applied to each subchannel separately. Void-drift should give increasing deviations of the real void-fraction from this model. These deviations should grow with the height. Only very small deviations were observed, so it can be concluded that void-drift does not play a significant role in the distribution of the vapour between the subchannels. The same can be concluded from a comparison of the void-fraction distribution with a tilted power profile.

Comparison of the chordal void-fraction for a gamma beam passing through the fuel rods and a gamma beam passing in between the fuel rods clearly shows a transition taking place at a height between 30 and 40 cm. The transition corresponds to a flow pattern change from bubbly to annular flow.

The void-fraction in the riser was measured and compared with the drift-flux model and Dix's correlation. The agreement was reasonable, although the model tended to underpredict the void-fraction. A direct fit of the distribution parameter and the local drift velocity gave better results.

In the downcomer the drift-flux model gives unreliable results because the local drift velocity is negative. The void-quality relation for the drift-flux model can become singular. Physically this means that the relative rise velocity of the bubbles is as large as the downwards flow velocity. A slip model gives better results in the downcomer. A fit with the data yields a slip ratio of 0.5.

Chapter 4

Steady-state behaviour of natural circulation

In this chapter a model for the steady-state behaviour of DESIRE will be derived. This will be done in two steps. First the sets of independent variables which define the state of the system will be identified. This can be done by considering the mass and energy balances over the natural circulation loop. Next the change of the dependent variables as a function of the independent variables will be studied. This will require a model which accounts for physical processes such as vapour formation, friction and carry-under.

4.1 Static flow model - overview

In order to be able to calculate the natural circulation flow rate we need to consider in detail the various phenomena which affect the natural circulation flow. This section gives an overview of the quantities which are important. Also it is indicated where problems occur and what methods are used to deal with these problems.

In a natural circulation loop the flow rate Φ can be described by the loop momentum equation (Todreas and Kazimi, 1990):

$$\frac{d\Phi(t)}{dt} = \frac{\Delta p_{driv}(t) - \Delta p_{loss}(t)}{\sum_i \frac{l_i}{A_i}} \quad (4.1)$$

with Δp_{driv} the driving force of the flow and Δp_{loss} the pressure losses. The summation in the denominator runs over the length-to-area ratios of all the sections of the loop, and accounts for the inertia of the flow.

The driving force is caused by the density difference between the assembly plus riser and the downcomer, which in turn is caused by the presence of vapour in the assembly and riser. The pressure losses Δp_{loss} can be divided into frictional pressure losses of the one-phase flow, frictional pressure losses of the two-phase flow and into accelerational pressure losses. The last two pressure losses depend on the void-fraction.

So the natural circulation depends primarily on the void-fraction, and the void-fraction depends on the power, the flow rate and the subcooling. In a natural circulation loop these quantities all depend on each other. Figure 4.1 tries to clarify this intricate web of relationships for a system with a constant pressure. This flow chart starts with the three independent variables (see section 4.2.1) at the top and ends with the terms in the momentum equation and the flow at the bottom of the figure. In between these two levels some of the dominant quantities are indicated.

The figure contains the following quantities:

- *Feedwater flow:* The feedwater flow rate is controlled by the feedwater pump. To maintain the liquid level the feedwater flow rate is regulated by a controller which takes the vapour flow rate, feedwater flow rate, liquid level and liquid level setpoint as input parameters. In a steady state situation the feedwater flow rate equals the vapour flow rate.
- *Subcooling:* The subcooling follows in a straightforward way from the condensate temperature, feedwater flow rate, circulation flow rate and carry-under (see section 4.2.1, equations 4.4 and 4.5). When studying the details of the two-phase flow in the fuel assembly it can be chosen as an independent variable instead of the condensate temperature.
- *Thermodynamic equilibrium quality:* see section 2.1 and equation 2.1.
- *Flow quality:* see section 2.1 and equation 2.2.
- *Void fraction in the assembly and riser:* The average void-fraction depends primarily on the flow quality. Two-phase flow models are used to make the connection between the two.
- *Carry-under:* Carry-under refers to the entrainment of vapour by the flow going into the downcomer at the riser exit. The quality of the flow in the riser and the flow velocity are the dominant factors determining the carry-under. No general model is available to predict the carry-under because of the complicated nature of the two-phase flow in the turning region at the riser exit and in the downcomer. In section 4.2.2 a model is formulated on the basis of measurements.

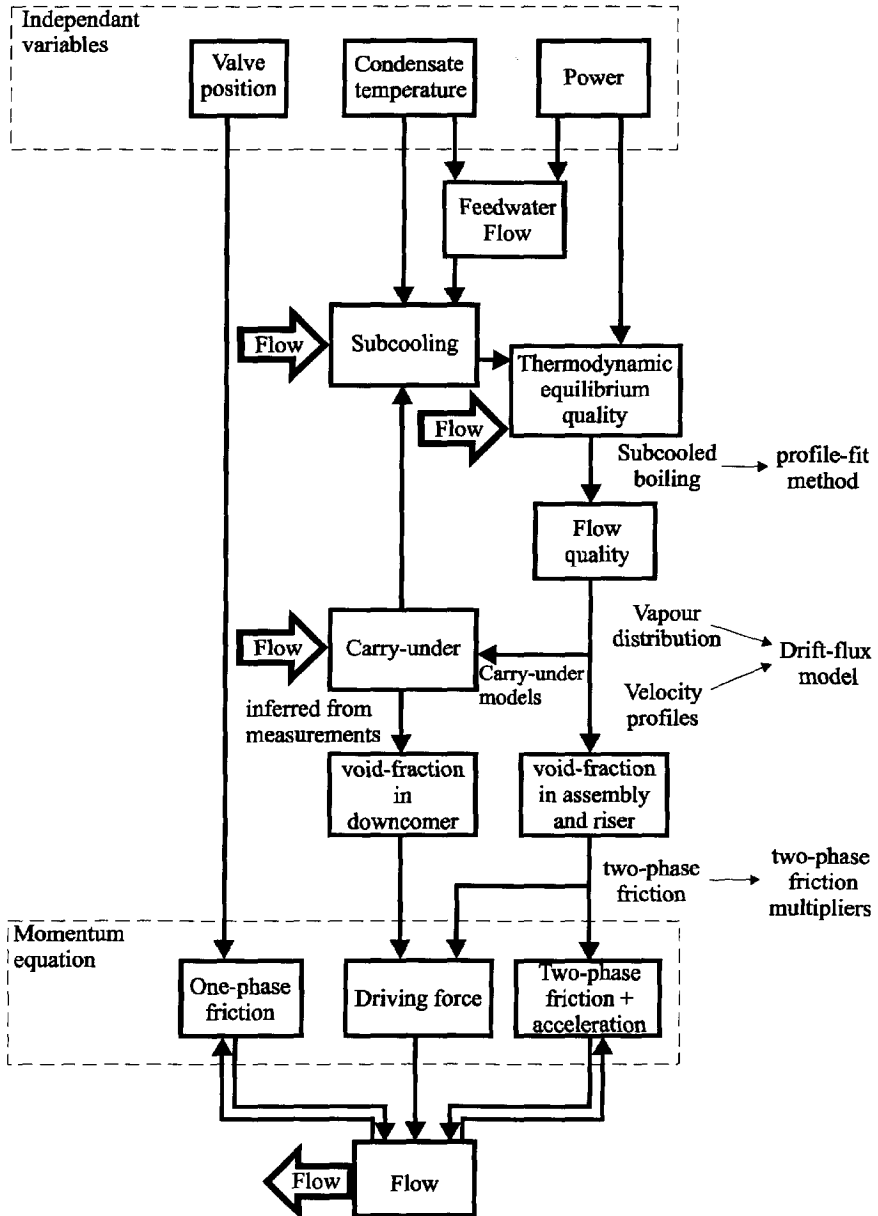


Figure 4.1 Flow chart showing the relationships between the independent variables of the DESIRE facility at the top and the various dependent variables such as the subcooling, carry-under, void-fraction and natural circulation flow rate.

- *Void-fraction in the downcomer:* Between the riser exit and the feedwater sparger there is vapour present which is caused by the carry-under. A void-slip model was found to give a reasonably good relation between the quality and the void-fraction in this region (see section 3.5.2).
- *Driving force:* The driving force of the two phase flow is given by the density difference between the fluid in the assembly + riser and the downcomer.

$$\frac{\Delta p_{driv}}{g} = \int_{\text{downcomer}} \rho_l dz - \int_{\text{riser+assembly}} (1-\alpha(z)) \rho_l + \alpha(z) \rho_g dz - \int_{\text{carry-under region}} \alpha(z) \Delta \rho dz \quad (4.2)$$

- *Two-phase friction:* The frictional pressure drop in the assembly is a very important component of the total frictional pressure drop. It is also important for the flow dynamics (see chapter 5). Unfortunately this pressure drop is very difficult to calculate. It is usually handled using a homogeneous flow model and applying a two-phase friction multiplier. For this two-phase multiplier correlations are available for different flow regimes.
- *One-phase friction:* This is the pressure drop in the one-phase flow region of the circulation loop. This friction can be influenced by the valve located just below the assembly.
- *Accelerational pressure drop:* The velocity of the two-phase flow increases in the assembly as vapour is formed. This causes an accelerational pressure drop over the assembly. The accelerational pressure drop over the riser equals zero (neglecting evaporation due to the pressure drop over the riser).

4.2 Static flow model - description

In this section a comprehensive static flow model of the natural circulation loop is developed. The development of the model starts with some basic considerations on mass and enthalpy balances around the loop. It is found that the carry-under flow rate must be specified to completely define the state of the system (section 4.2.1). For this purpose an empirical model of the carry-under is derived from measurements (section 4.2.2). Finally, detailed analysis of the driving and frictional forces around the loop gives us the value of the natural circulation flow rate (sections 4.2.3). The resulting model takes just three input parameters, (power, friction valve coefficient and condensate temperature) and calculates the natural circulation flow rate, subcooling, carry-under and other dependent quantities.

4.2.1 Relations derived from mass and energy balance

Mass and energy balance

The natural circulation loop can be viewed as a nodal scheme shown in figure 4.2. The enthalpies in this figure are all given relative to the enthalpy of the liquid at saturation temperature.

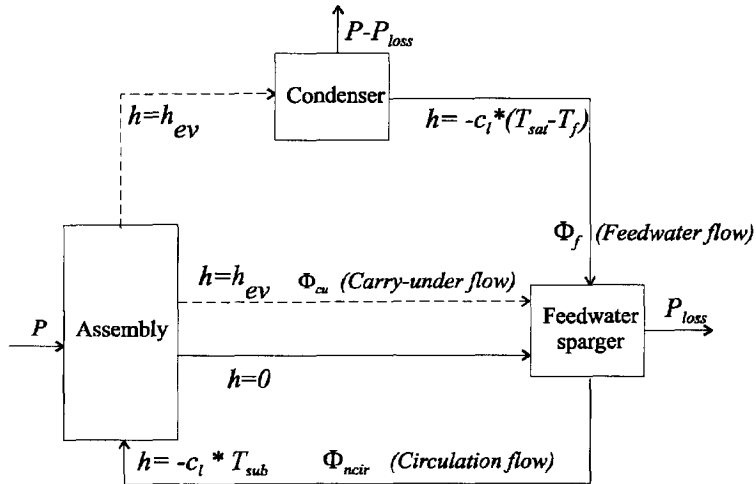


Figure 4.2 Nodal scheme of the natural circulation loop. Solid lines indicate liquid flows and dashed lines indicate vapour flows. For each flow the enthalpy relative to the liquid saturation enthalpy is given.

Liquid enters the fuel assembly subcooled, its enthalpy is lower than zero. In the assembly heat (power P) is added to the flow. Part of the liquid is turned into vapour, so two flows can be identified leaving the assembly. One is the vapour flow, with a relative enthalpy equal to the evaporation enthalpy, and the other is the liquid flow, which is now at saturation temperature so the relative enthalpy equals zero. The liquid flows to the feedwater sparger. The vapour takes two paths, part of the vapour also flows directly to the feedwater sparger (carry-under), the rest flows to the condenser. Here heat is extracted from the flow. At the feedwater sparger all the flows meet again. The carry-under is condensed by the cold feedwater flow.

The P_{loss} term is used to account for the heat lost from the facility, both in the heat exchangers in the downcomer loops and by the heat loss to the environment.

It is assumed that all the carry-under is condensed by the cold feedwater flow. If this is not the case the subcooling temperature will be zero, but the quality of the flow entering the assembly can be larger than zero. It is not possible to measure this quality, so the model cannot be used

unless all the carry-under is condensed. The presence of vapour in the downcomer below the feedwater sparger can be visually inspected through viewing ports.

A mass and enthalpy balance over the 3 nodes gives:

$$\begin{aligned} -c_l T_{sub} \Phi_{ncir} - h_{ev} (\Phi_f + \Phi_{cu}) &= -P \\ (h_{ev} + c_l (T_{sat} - T_f)) \Phi_f &= P - P_{loss} \\ h_{ev} \Phi_{cu} - c_l (T_{sat} - T_f) \Phi_f + c_l T_{sub} \Phi_{ncir} &= P_{loss} \end{aligned} \quad (4.3)$$

From this system one equation can be eliminated leaving a system of two equations which contains six variables (Φ_f , Φ_{cu} , Φ_{ncir} , P , T_{sub} and T_f). Thus four variables are needed to characterize the system. From these six variables three are controllable (P , Φ_{ncir} and T_f) and five are measureable (all except Φ_{cu}).

Summarizing, four variables are needed to define the state of the system, but only three variables are controllable. This means we cannot bring the system into any state we want. Basically this is caused by our inability to control the carry-under. We should add another equation to the three enthalpy balances which gives the carry-under as a function of the other variables. To do this we need a model which describes carry-under.

We can rewrite equations 4.3 to express the non-controllable parameters in terms of the controllable parameters and the carry-under. This gives:

$$\Phi_f = \frac{P - P_{loss}}{h_{ev} + c_l (T_{sat} - T_f)} \quad (4.4)$$

and

$$T_{sub} = \frac{-h_{ev} \Phi_{cu} + c_l (T_{sat} - T_f) \Phi_f}{c_l \Phi_{ncir}} + \frac{P_{loss}}{c_l \Phi_{ncir}} \quad (4.5)$$

4.2.2 Carry-under

Figure 4.3 shows the section of the loop at the riser exit. This flow in the downcomer partly consists of entrapped vapour, the carry-under. At the feedwater sparger the cold feedwater is injected. Here the carry-under is condensed.

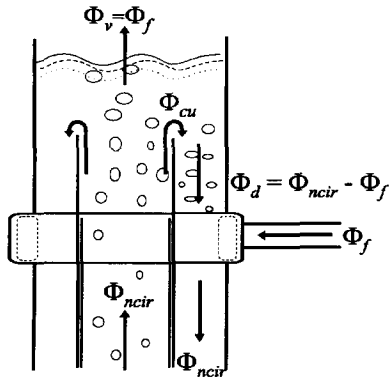


Figure 4.3 The region around the riser exit.

It is not feasible to calculate the carry-under from first principles. Basically the carry-under is determined by the behaviour of the downward two-phase flow between the riser exit and the feedwater sparger. Lützow performed theoretical and experimental work on the carry-under in boiling water reactors (Lützow and Wegner, 1990; Lützow and Stäck, 1987; Lützow and Wegner, 1987). In his model the bubbles near the center of the riser are assumed to escape while bubbles near the riser wall are assumed to be dragged into the downcomer. An imaginary surface which separates these two regions is defined. The carry-under then depends on the position of this surface and on the radial void-fraction profile.

This view is not consistent with our observations that the flow in this region is highly turbulent. It is visually apparent that bubbles often can escape to the surface from positions well down into the downcomer. These bubbles are aided in their escape by flow oscillations and the presence of circulatory flow structures. Other measurements are reported by Hidaka and Suzuki (1990). They did not measure the carry-under but the void-fraction in the downcomer. The void-fraction in their experiments depended on the axial position in the riser. Near the riser exit the void-fraction in the downcomer is largest. Going downwards the void-fraction decreases until a constant value is reached. This is consistent with our own observations that bubbles present in the downcomer can still escape to the surface.

All of these experiments were performed with air-water systems and with a different geometry from DESIRE, so the results cannot be applied to DESIRE. We will develop our own correlation for the carry-under in DESIRE.

Carry-under as a function of quality and flow rate

The carry-under flow rate can be written as the product of the downcomer flow rate and the downcomer quality:

$$\Phi_{cu} = \Phi_d x_d = \Phi_d x_r \Psi \quad (4.6)$$

where Ψ is the entrainment ratio which is defined as the ratio of the quality in the downcomer to the quality in the riser. The simplest model of carry-under assumes that the entrainment ratio is independent of the flow rate or the quality. For the Dodewaard reactor the entrainment ratio was determined as a function of water level (Wouters et al., 1992a, 1992b) and as a function of the pressure (Van der Hagen et al., 1993). In these measurements the entrainment ratio ranged from about 13% to about 21% with the latter value corresponding to the nominal pressure case.

During steady-state operation the carry-under in DESIRE can be determined using a mass and heat balance over the feedwater sparger node. Equation 4.5 can be used with P_{loss} set to zero and T_{sub} determined not from the assembly inlet but from the thermocouple placed downstream of the feedwater sparger.

Measurement of the carry-under in DESIRE was done for different values of the flow rate and quality. The flow-quality plane coverage is shown in figure 4.4a. For each measurement point in figure 4.4a the carry-under is calculated using the constant entrainment ration model and plotted against the measured carry-under. The result can be seen in figure 4.4b. It is clear that this model cannot adequately describe the measurements. It was observed during the experiments that the carry-under would become negligible when the flow rate was less than 0.5 kg/s. At this low flow rate the velocity in the downcomer is smaller than the bubble rise velocity and almost all bubbles escape. We can improve the correlation by considering this as an offset to the flow rate. The result is the scatter plot in figure 4.4c. There is an improvement for low carry-under but the correlation is still poor. It seems necessary to abandon the concept of entrainment ratio, the carry-under depends more strongly on the flow rate than this model permits. In figure 4.4d an optimal fit is shown with the flow rate raised to a higher power. This gives a much better fit which is given by

$$\Phi_{cu} = 0.18 x_r (\Phi_{ncir} - \Phi_f - 0.5)^{2.5} \quad (4.7)$$

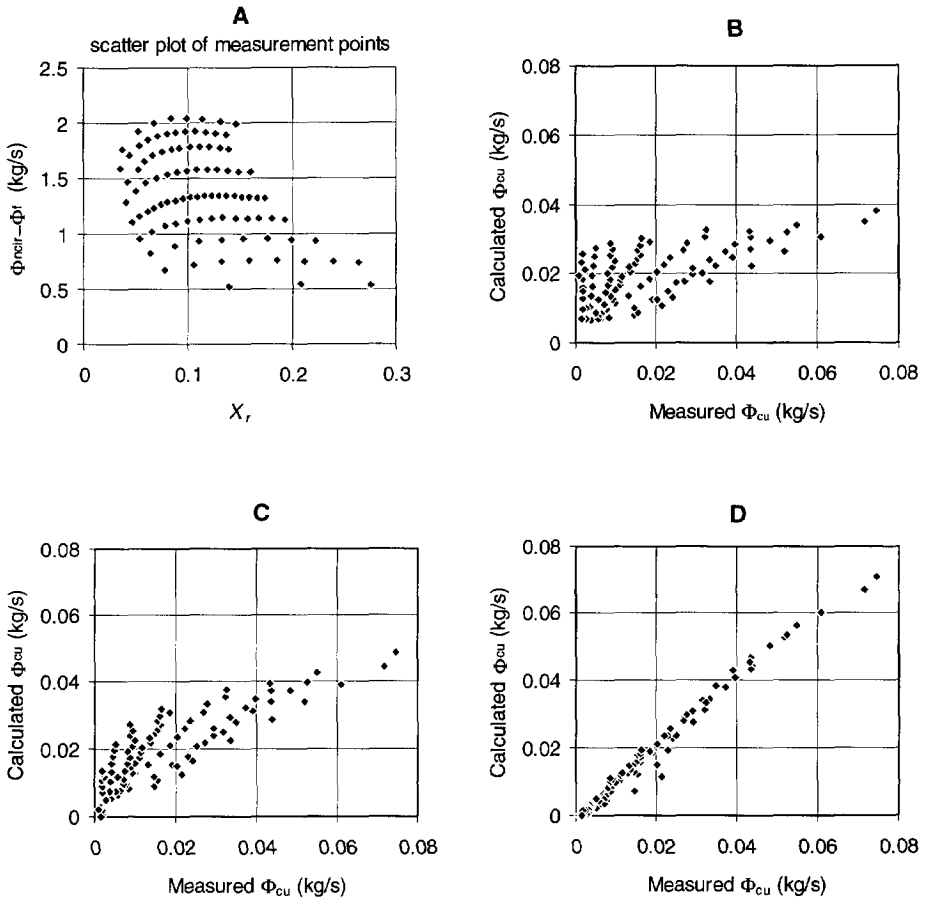


Figure 4.4 Modeling of carry-under.

A Location of the measurement points in the flow-quality plane.

B Comparison of the measurement with the constant entrainment-ratio model.

$$\Phi_{cu} = 0.13 X_r (\Phi_{ncir} - \Phi_f)$$

C Same as B with threshold in the flow rate.

$$\Phi_{cu} = 0.22 X_r (\Phi_{ncir} - \Phi_f - 0.5)$$

D Optimal fit:

$$\Phi_{cu} = 0.18 X_r (\Phi_{ncir} - \Phi_f - 0.5)^{2.5}$$

4.2.3 Momentum equation

We will now look in more detail at the phenomena determining the magnitude of the natural circulation flow. To calculate the driving force of the natural circulation flow rate we need to know the void-fraction (equation 4.2). This was covered in chapter 3. In this section we will consider the various pressure losses in the loop.

inlet friction

This term contains two parts: the friction at the inlet of the fuel assembly and the friction due to the controlling valve. The frictional pressure drop is given by:

$$\Delta P = (K_{in} + K_{valve}) \frac{\Phi^2}{A_{as}^2 2 \rho_l} \quad (4.8)$$

The friction factor of the inlet of the core (K_{in}) is used as a tuning parameter. It is determined as follows. A measurement is performed at nominal operating conditions. The measured values of the flow rate, power, pressure drop over the valve and feedwater temperature are inserted into the model. Then K_{in} is set so that the total pressure drop over the loop equals zero. This results in $K_{in}=3$. This value is used in all subsequent calculations, also for non-nominal operating conditions.

friction in fuel assembly

The friction in the fuel assembly is divided into an one-phase pressure drop and a two phase pressure drop. The one-phase pressure drop is given by:

$$\Delta P_{1\phi} = z_{bb} \frac{f \Phi^2}{2 D_h A_{as}^2 \rho_l} \quad (4.9)$$

where z_{bb} is the boiling boundary (the height at which the thermodynamic equilibrium quality becomes zero) and f the friction factor which depends on the Reynolds number Re as (Todreas and Kazimi, 1990):

$$\begin{aligned} f &= 0.316 \cdot Re^{-0.25} & \text{if } Re < 3 \cdot 10^4 \\ f &= 0.184 \cdot Re^{-0.2} & \text{if } Re > 3 \cdot 10^4 \end{aligned} \quad (4.10)$$

As an alternative to the boiling boundary the departure point could be considered as a more realistic point where the transition from single-phase to two-phase flow takes place. However, the two-phase friction multipliers that are used to calculate the frictional pressure drop in the two-phase flow are only valid for flows in thermodynamic equilibrium. Either way one makes an error when trying to calculate the pressure drop between the departure point and the boiling

boundary, but the difference between the two approaches will be small compared to other uncertainties in the pressure drop of the two-phase flow.

The expression for two-phase pressure drop is similar to the expression for the one-phase pressure drop except for the presence of a two-phase multiplier:

$$\Delta P_{2\phi} = (H - z_{bb}) \frac{f \Phi^2}{2 D_h A_{as}^2 \rho_l} \phi(x) \quad (4.11)$$

The two-phase multiplier ϕ is a function of the flow quality:

$$\phi = 1 + \left(\frac{\rho_l}{\rho_g} - 1 \right) x \quad (4.12)$$

Since the quality is a function of the height the two-phase multiplier is also a function of the height. But because ϕ is linear in x we can use a constant multiplier based on the average quality in the two-phase region.

accelerational pressure drop

Because the flow in the fuel assembly speeds up as vapour is produced there is a pressure drop due to the acceleration of the flow. This pressure drop is easily calculated by considering the momentum of the flow entering and leaving the assembly. This gives:

$$\Delta P_{acc} = \frac{(x \Phi)^2}{\alpha \rho_g A_{as}^2} + \frac{((1-x) \Phi)^2}{(1-\alpha) \rho_l A_{as}^2} - \frac{\Phi^2}{\rho_l A_{as}^2} \quad (4.13)$$

where the quality and void-fraction are the values at the exit of the assembly.

friction at assembly exit

The two phase friction at the assembly exit is treated like the one-phase friction with a two-phase multiplier

$$\Delta P_{ex} = (K_{ex}) \frac{\Phi^2}{A_{as}^2 2 \rho_l} \phi_R \quad (4.14)$$

where the Romie multiplier ϕ_R is given as:

$$\phi_R = \frac{(1-x)^2}{1-\alpha} + \frac{\rho_l}{\rho_g} \frac{x^2}{\alpha} \quad (4.15)$$

The pressure drops over the three spacers are discounted for in K_{ex} . The friction factor K_{ex} is given by Dodewaard as 3.024.

pressure drop in riser

The pressure drop in the riser is only the frictional pressure drop. Since the effects of the pressure change on the vapour and liquid densities and on the saturation temperature are neglected, there is no phase change in the riser and thus no accelerational pressure drop.

$$\Delta P_r = L_r \frac{f \Phi^2}{2 D_h A_r^2 \rho_l} \phi(x) \quad (4.16)$$

friction at riser exit

At the riser exit the flow makes a 180° turn from the riser into the downcomer. The pressure drop resulting from this is calculated by:

$$\Delta P_{re} = (K_{re}) \frac{\Phi^2}{A_r^2 2 \rho_l} \phi_R \quad (4.17)$$

The value of the friction coefficient K_{re} is taken rather arbitrarily as 1. It is not to be expected that this pressure drop can adequately be described by equation 4.17. It will depend on such things as the carry-under and the liquid level above the riser exit.

friction in downcomer and downcomer loops

The frictional pressure drop of the one-phase flow in the downcomer and the downcomer loops is treated by a single friction factor. This friction factor is determined by summation of the friction factors of all the different components in the downcomer. This gives a value of 3.5 for the total friction factor for the downcomer and downcomer loops. The frictional pressure drop is then given by

$$\Delta P_d = (K_d) \frac{\Phi^2}{A_d^2 2 \rho_l} \quad (4.18)$$

These are two additional pressure drops in the downcomer: the acceleration pressure drop due to the condensation of the carry-under and the pressure drop due to the acceleration of the feedwater flow (which is injected horizontally). Because the velocity in the downcomer is relatively small both these pressure drops can be neglected.

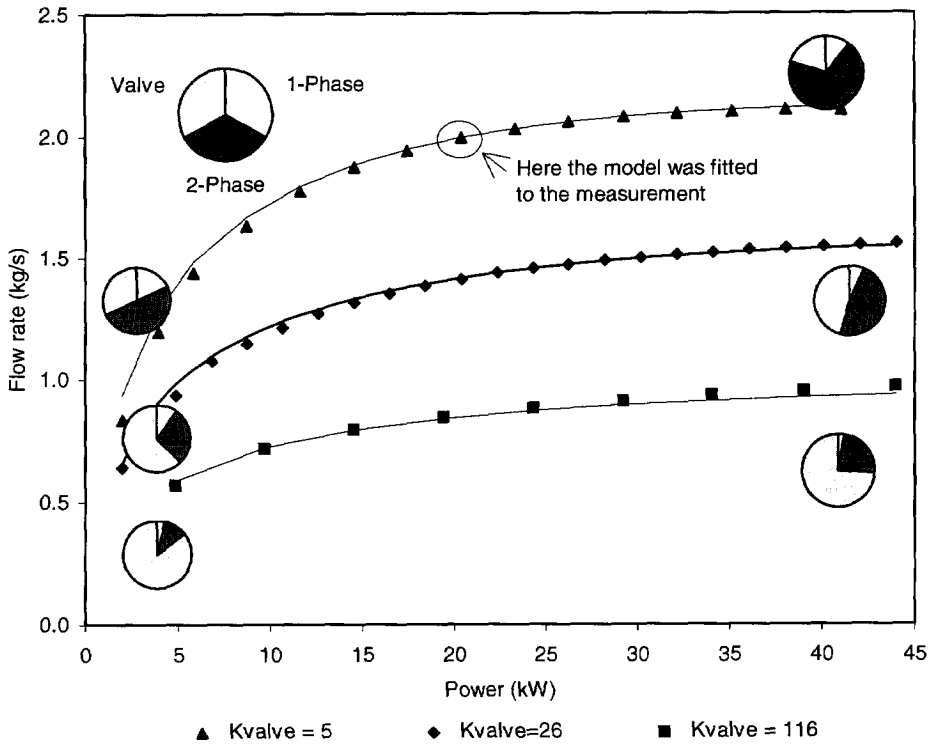


Figure 4.5 Comparison of measured flows (symbols) with the calculation (lines) for three values of the inlet valve friction coefficient. The pie charts give a breakdown of the total pressure drop over the pressure drop in the single-phase region, in the two-phase region and the pressure drop over the inlet valve.

4.3 Comparison of model to measurements

4.3.1 Flow rate as a function of power

In figure 4.5 the results of a measurement of the circulation flow rate as a function of the power are shown for three valve positions and a feedwater temperature of $-5\text{ }^{\circ}\text{C}$. The agreement is excellent except at very low power, where the flow rate is overpredicted. The model was adjusted to the measurement by tuning K_{in} at a power of 22 kW and a flow rate of 2 kg/s ($K_{valve}=5$).

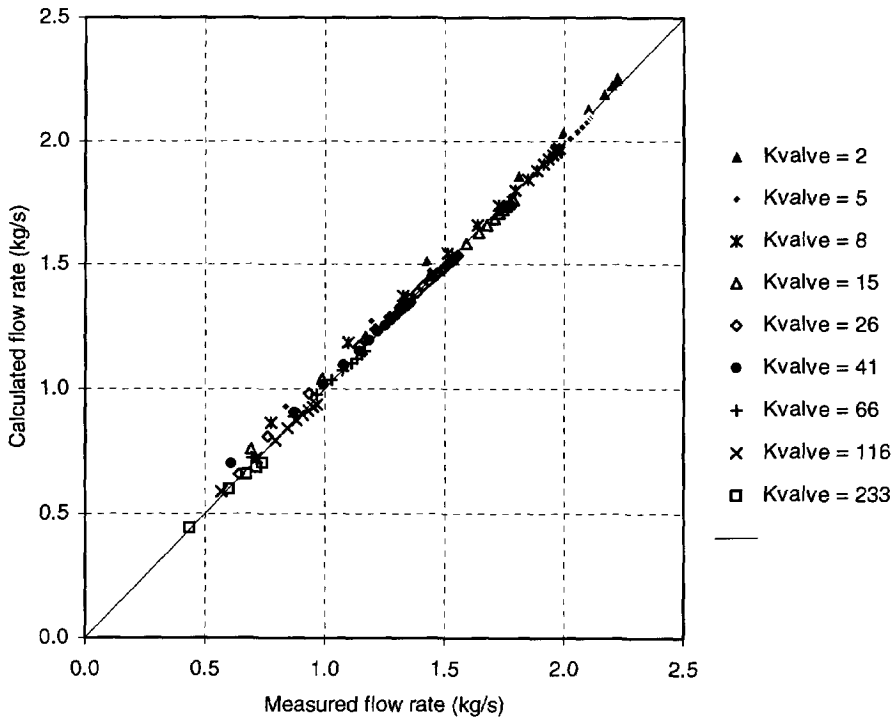


Figure 4.6 Scatter plot comparing measured flow rate to calculated flow rate for a large range of values of the inlet valve friction coefficient and of the power.

The relative pressure drops in the single-phase region, the two-phase region and over the inlet valve are shown as pie charts in the figure. The distribution of these pressure drops is important for the dynamics of the loop, as will be seen in chapter 5.

The same results are shown in figure 4.6 as a scatter plot comparing measured to predicted values for a wider range of friction factors (2-316) and powers (2-45 kW). The significance of this result is that the model predicts the flow rate correctly for a wide range of circumstances with the adjustment of only one parameter (K_{in}). This strongly suggests that the model contains all the relevant physics of the system.

4.3.2 Flow rate as a function of condensate temperature

Of the three independent parameters determining the flow rate in DESIRE (power, friction valve and condensate temperature) the previous section compared the effect of the first two on the flow rate. In figure 4.7 the effect of the condensate temperature is shown. The effect of the condensate temperature is quite small. In this figure it is the slope of the lines which is important, not the offset between the measurement and model because this can be caused by

small measurement errors in the friction coefficient of the inlet valve. Looking at the left figure we see that the slope at low power is somewhat smaller than the model predicts. The difference is larger at 22 kW. At 30 kW the measurement even shows a negative slope while the model still predicts a positive slope.

The difference between model and measurement seems to depend on the power. One phenomenon which could be the cause of this, and which is not taken into account in the model, is the speed of condensation of the carry-under below the feedwater sparger. The model assumes that the carry-under is condensed immediately (the cold feedwater is injected through 36 holes of 2 mm diameter with a velocity of almost 1 m/s, so the mixing is quite good), but in reality the vapour will travel some distance downwards before it is all condensed. It can be expected that a higher feedwater temperature will slow down the condensation process, in which case the carry-under will penetrate deeper into the downcomer thus decreasing the driving force and the flow rate. It can also be expected that this will be more important if the carry-under is larger.

This view is consistent with figure 4.7. At high power the carry-under is higher so the effect is large. We would expect this effect to disappear when the carry-under becomes very small. This is indeed what happens as can be seen in the middle figure, where a measurement is shown at a reduced flow rate (so the carry-under is small). The slope of the two lines are equal to within 10%. If we plot the ratios of the slopes (measured and model) against the carry-under we find that a linear fit through these points almost exactly crosses the y-axis at one, which is another strong indication that the condensation process of the carry-under is the source for the differences.

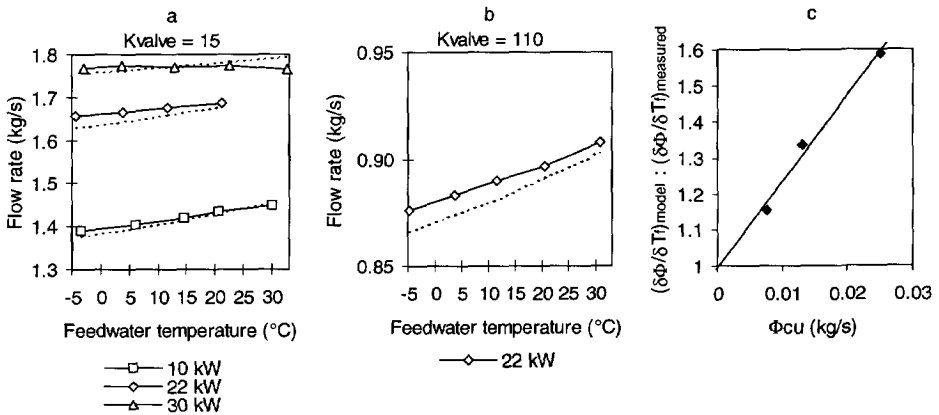


Figure 4.7 a,b Flow rate as a function of the feedwater temperature, measured (solid lines) and calculated (dotted lines). There is a slight difference in the slope of the lines.

- c. The ratio of the slopes of the measured and calculated curves is a linear function of the carry-under.

4.4 *Conclusions*

In this chapter a static flow model was developed. The important processes that determine the natural circulation flow rate were identified and modeled. The void-fraction is calculated using the models derived in chapter 3. A correlation for the carry-under was derived on the basis of measurements.

The model is in excellent agreement with measurements of the natural circulation flow rate over a wide range of operating conditions (at nominal pressure). This suggests that all the relevant physics are contained in the model. The model has become a very useful tool for the experimenter. Examples for its use are for predicting the effect of feedwater temperature changes on the subcooling and the natural circulation flow rate, or the effect of the heat exchangers in the downcomer on the subcooling. Without such a model these effects are very difficult to predict because a change in one variable will change all the other variables.

The most important conclusion we can make from the success of the model is that distribution of the friction factors between the one-phase region and the two-phase region is modeled correctly. This is of vital importance for the dynamics of the natural circulation flow. These friction factors will be needed when we develop a model of the dynamics in chapter 5. What we are not able to deduce from the measurements is exactly where the two-phase pressure drop takes place: in the fuel assembly, at the spacers, at the assembly exit or at the riser exit. For this is necessary to install differential pressure sensors at all these locations. However, it is not clear at this point in time whether such detailed information is essential for the model of the dynamics.

Chapter 5

Modeling the dynamics

5.1 *Types of instability*

There are many types of thermal-hydraulic instabilities in BWRs which can be classified in various ways (d'Auria et al., 1996). A first distinction can be made between 'static' and 'dynamic' instabilities. Static instabilities follow from the steady-state behaviour of the system. Examples are flow excursion (Ledinegg) instability, flow regime transitions and geysering (Lahey and Moody, 1991). Dynamic instabilities on the other hand depend on the time dependent equations describing the system. This class of instabilities is much more varied and complex than the static instabilities.

Of the various types of dynamic instabilities the so-called "density-wave" instability is the dominant one in BWRs. As its name suggests, in this type of instability a variation of the density (or void-fraction) of the two-phase liquid is carried through the reactor by the flow. The reason that this type of instability is of particular importance in a nuclear reactor is that the reactivity of the reactor depends on the density of the moderator in the core. Thus a density-wave through the reactor has a direct effect on the power produced in the reactor, which in turn affects the density of the flow through the core. However, it is important to realize that this nuclear coupled feedback is not necessary for instabilities to occur. Purely thermal-hydraulic instabilities are possible, including the density-wave instability.

We will look somewhat closer at the physical mechanism behind density-wave oscillations. Consider a boiling flow channel with only an inlet and an exit flow restriction. The total pressure drop over the channel is assumed to be constant (which is the case when there are many parallel channels). The following sequence of events then occurs during a density-wave oscillation. Suppose that there is a small positive perturbation in the inlet velocity. This will

result in a smaller void-fraction in the channel and thus a higher density of the mixture. This high-density perturbation is carried upwards with the flow. When the high-density wave perturbation reaches the exit of the channel the pressure drop over the exit will increase. Since the total pressure drop over the channel is assumed to be constant this causes an instantaneous decrease of the pressure drop over the inlet. This can only be accommodated by a decrease of the inlet velocity. The whole cycle then repeats itself, but now with a low-density wave. Based on this qualitative picture, the time constant of the oscillation is estimated at twice the flow transit time through the channel (Bouré et al., 1973).

This has been the conventional explanation of the mechanism of density-wave oscillations. This model is based on the effect of density on the two-phase pressure drop. Rizwan-uddin performed numerical calculations on a boiling channel and concluded that the velocity variations are more important than the density variations (Rizwan-uddin, 1994). He also showed that traveling density-waves do not play an important role during the oscillations. Finally, it turned out that the oscillation period typically lies between three to four times the channel transit time. So it seems that the name density-wave oscillations is a misnomer. Of course density and velocity in a two-phase flow are closely linked, and which of the two is the dominant cause of the oscillations depends on the details of the parameters of the model (power, subcooling, flow rate and pressure drop distribution in the channel). The calculations Rizwan-uddin performed were at high subcooling ($N_{sub}=10$, $N_{Zu}=16.85$). The flow rate evolved to a large-amplitude limit cycle, with a strong non-sinusoidal shape, indicating the importance of non-linear effects.

Two modes of density-wave oscillations can be distinguished: the single channel and the parallel channel modes. In the parallel channel mode two or more channels are connected at the bottom and at the top (the discussion in the previous two paragraphs considered the parallel channel mode). It is then possible for the flow rate in one channel to increase while the flow rate in the other decreases, keeping the total flow rate constant. Since the inertia of the liquid in the rest of the loop does not suppress the oscillations in this case the parallel channel oscillations may be less stable than the single channel oscillation. Translated to a boiling water reactor core the two modes are recognized as core wide oscillations (called in-phase oscillations) and regional oscillations (called out-of-phase oscillations). In this case the subcriticality of the out-of-phase neutronic mode serves to attenuate the out-of-phase oscillations, and the in-phase mode usually dominates. However, out-of-phase modes have also been observed in large boiling water reactors, where the neutronic coupling between two regions of the core (i.e. the subcriticality) becomes small.

5.2 *Simplified analytical model of dynamics*

In this section a model developed at IRI for the description of instabilities in a natural circulation system will be presented (Van Bragt and Van der Hagen, 1998a). The purpose of this model is to gain an understanding of the processes which are important for the stability of the natural circulation loop.

5.2.1 Short description of model

Figure 5.1 shows the general structure of the frequency domain version of the model. From this structure it can be seen that the transfer function from heat flux to void-fraction is quite complicated. Three parameters play an important role in this transfer function: the boiling boundary, the mass flux density and the void-fraction. The exact forms of the various transfer functions will not be given here (see Van Bragt, 1995). Instead the assumptions on which each transfer function was derived will be listed.

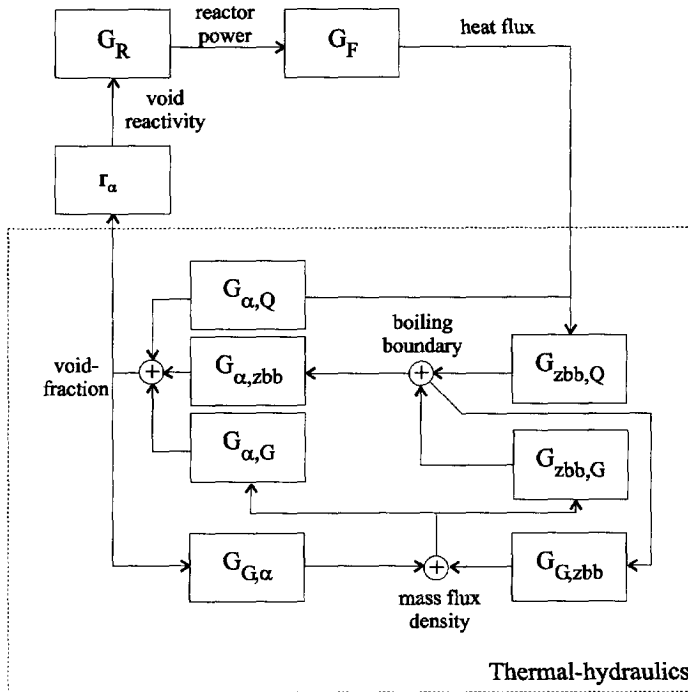


Figure 5.1 Structure of the model describing the dynamics of the natural circulation loop with neutronic feedback.

G_R Reactor transfer function

The power of the reactor is described using the point kinetics equations with one group of delayed neutrons (Hetrick, 1971):

$$\frac{dn(t)}{dt} = \frac{\rho - \beta}{\Lambda} n(t) + \lambda c(t) \quad (5.1)$$

$$\frac{dc(t)}{dt} = \frac{\beta}{\Lambda} n(t) - \lambda c(t) \quad (5.2)$$

with n the number of neutrons, ρ the reactivity, β the delayed neutron fraction, λ the decay rate of the neutron precursors, c the number of neutron precursors and Λ the neutron generation time.

Because we are only interested in relatively low frequency oscillations (in the order of 1 Hz) we can apply the prompt-jump approximation by neglecting the dn/dt term in equation 5.1. To obtain the transfer function the resulting equations are linearized, second order terms in the perturbations are neglected and the Laplace transform is applied. The average reactivity is assumed to be zero (the reactor is critical). This results in the zero-power reactor transfer function (Hetrick, 1971):

$$G_R = \frac{\delta \hat{n} / n_0}{\delta \hat{\rho}} = \frac{s + \lambda}{\beta s} \quad (5.3)$$

where the caret signifies the Laplace transformed variable and n_0 is the steady-state number of neutrons. This transfer function is called the zero-power reactor transfer function because temperature effects are not taken into account.

G_F *Fuel transfer function*

This transfer function will be needed for the simulation in DESIRE. The power produced in the fuel is transferred to the two-phase flow. This is described as a first order process. The transfer function of this process is given by

$$G_F = \frac{1}{1 + s \tau_f} \quad (5.4)$$

where τ_f is the fuel time constant. For the Dodewaard reactor this fuel time constant varies from 4.6 seconds at the beginning of cycle to 6.5 seconds at the end of cycle (Van Engen and Nissen, 1981; Fenech, 1981). However, Van der Hagen showed that the fuel dynamics cannot be accurately represented with a single fuel time constant. The fuel time constants mentioned above are only valid for low frequency oscillations. For higher frequencies a shorter effective fuel time constant should be used. Experimental data and numerical calculations suggest an effective fuel time constant of approximately 2 seconds (Van der Hagen, 1988).

$G_{zbb,Q}$ *Heat flux to boiling boundary transfer function*

The boiling boundary is a function of power, flow rate and subcooling. For a steady-state system its value can easily be found using a thermal balance (equation 3.12). For the dynamics the thermal balance has the form of a partial differential equation. To simplify the analysis this equation is integrated over the spatial variable, resulting in an ordinary differential equation.

This is a quasi-static approximation, which neglects wave-like phenomena. Subcooled boiling is not taken into account. The power profile has an important effect on the boiling boundary dynamics and is included in the model.

$G_{zbb,G}$ *Mass flux density to boiling boundary transfer function*

This transfer function is very similar to $G_{zbb,Q}$. It describes the effect of the mass flux density on the boiling boundary. The same equations and approximations as in $G_{zbb,Q}$ are used.

$G_{w,Q}$, $G_{w,zbb}$, $G_{w,G}$

These transfer functions determine how the void-fraction changes in response to heat flux, boiling boundary and mass flux density fluctuations. Again a quasi-static approximation is used (see section 5.2.2). The Bankoff void model is used to relate the quality in equation 5.7 to the void-fraction in equation 5.6 (Bankoff, 1960; the Bankoff void model is obtained by setting $v_{gj}=0$ in the drift-flux model). The void-fraction in the riser is expressed directly as a function of the void-fraction at the assembly exit and of transit time through the riser.

$G_{G,w}$, $G_{G,zbb}$ *Void-fraction and boiling boundary to mass flux density transfer function*

These transfer functions describes how the circulation flow rate responds to the change in void-fraction and boiling boundary perturbations. It is derived from the loop momentum equation (equation 4.1). The expressions for the various terms (pressure drops etc.) in this equation are mostly the same as those used in the static flow model in chapter 4, so the same friction coefficients for the various sections of the loop can be used.

r_α *void-reactivity coefficient*

The void-reactivity follows from the void-reactivity coefficient and the void-fraction as follows:

$$\rho_\alpha = r_\alpha \Delta\alpha \quad (5.5)$$

where $\Delta\alpha$ is the deviation of the void-fraction from the steady-state value, averaged over the volume of the fuel assembly.

5.2.2 Limitations of the model

The model is mainly focused on the dynamics of the fuel assembly and riser. Therefore the following phenomena are not modeled:

- feedwater dynamics
- carry-under effects
- nuclear Doppler effect

To greatly simplify the analysis also not modeled are:

- subcooled boiling
- pressure dependent material properties (density etc.)
- void propagation (wave-like phenomena) in the assembly

This last point needs some clarification. Consider a step in the power or in the flow rate. The quality in the assembly will change, but a new equilibrium value will not be reached until the liquid that was at the bottom of the assembly at the time of the step has reached the top of the assembly. Thus the response of the quality at the upper end of the assembly is delayed. To simplify the analysis the model applies a quasi-static approach (Hashimoto, 1993) by integration over the spatial variable in the partial differential equation. The quality profile over the two-phase region is assumed to react equally over the total length to a perturbation:

$$x(z, t) = \frac{z - z_{bb}}{H - z_{bb}} x(z = H, t) \quad (5.6)$$

where the power profile over the two-phase region is approximated by a linear function. The quality at the assembly exit in equation 5.6 relaxes to the new equilibrium value with a characteristic time constant which replaces the transit time that was lost in the integration. This is a good approximation if the transit time through the assembly is short compared to the time constant of the quality oscillations. Still, in section 5.2.3 it is shown that the quasi-static approximation can have quite a large effect on the dynamics.

In the riser section the flow is adiabatic. In that case it is not necessary to use the quasi-static approximation. This is very fortunate since the transit time through the riser is typically two to three times the transit time through the assembly.

5.2.3 General trends predicted by the model

The closed loop transfer function of the natural circulation loop with feedback can be written as:

$$G(s) = \frac{G_R}{1 - r_\alpha G_F(s) G_{TH}(s)} \quad (5.7)$$

with $G(s)$ the closed loop transfer function from reactivity to power. The stability of this system depends on the roots of the denominator of the transfer function, which are called the poles of the transfer function. A pole at complex frequency s (actually a conjugate pair of poles) gives a solution in the form of:

$$x(t) \equiv \sin(\omega t) e^{\sigma t} \quad (5.8)$$

where ω and σ are related to s by:

$$s = \sigma \pm i \omega \quad (5.9)$$

Thus $x(t)$ is an exponentially decreasing (or increasing) sinusoidal function. The ratio between two consecutive maxima of this function is called the decay ratio (DR) and follows from by:

$$DR = e^{-2\pi\sigma/\omega} \quad (5.10)$$

If the poles all lie in the left-hand plane the system is stable, else it is unstable.

Because the thermal-hydraulic transfer function is very complicated it is not feasible to find the poles analytically. They have to be found numerically by selecting a starting point in the s -plane and using a numerical search method. If there is more than one pole present it depends on the starting point in the s -plane to which pole the numerical algorithm converges. In order to be able to choose the correct starting point it is necessary to have an idea of the value of the transfer function in the whole s -plane. This is done by plotting the magnitude of the denominator of the transfer function in the s -plane. This value becomes zero where there is a pole present. The parameters used in these calculations are given in table 5.1.

P	22 kW
Φ	1.8 kg/s
T_{sub}	2 °C
Pressure	11.6 bar
λ	0.0767 s ⁻¹
β	0.0065
τ_f	0.5 s (unless specified otherwise)
r_a	-0.04 (unless specified otherwise)
power profile	chopped cosine, peaking factor 1.4

Table 5.1 Parameters used in the calculations

Figure 5.2 shows two cases as a contour plot: on the left is the case without a riser present and on the right the case with a riser present. The importance of the riser is apparent. Without a riser there is only one pole present. The frequency of this pole is 0.57 Hz. The transit time through assembly is 0.65 seconds, which gives $f=1/(2.7\tau)$. This value lies in between the value expected in the conventional view of the density-wave mechanism and the value proposed by Rizwan-uddin. The fact that there is only one pole is a result of the neglecting of wave-like phenomena in the assembly.

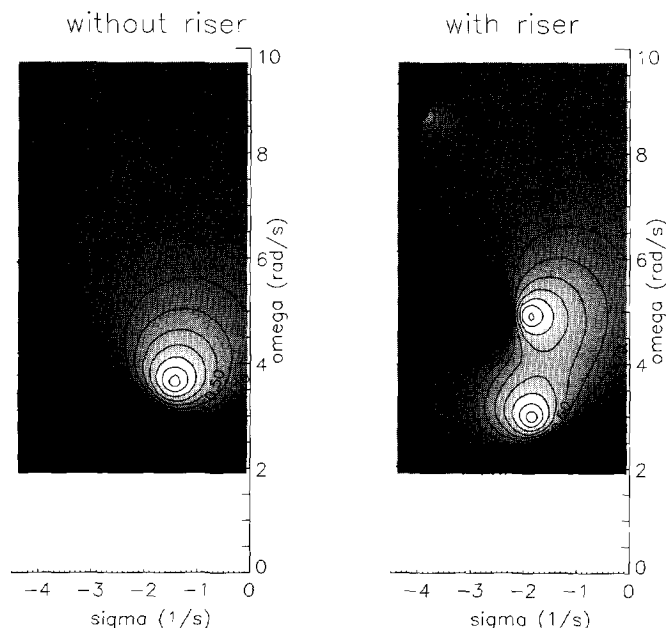


Figure 5.2 Magnitude of the denominator of the closed loop transfer function in the s -plane, for a system without a riser (left figure) and with a riser (right figure).

The transfer function changes when we add a riser to the system. The flow in the riser is modeled as a transport delay. Since the phase lag of a transport delay increases linearly with the frequency there are an infinite number of poles. These poles at higher frequencies are generally suppressed by the low-pass filter effects of the fuel heat transfer and the inertia of the liquid in the circulation loop. In the right figure of figure 5.2 three poles are visible.

We can better understand the origin of the poles by looking how they move in the s -plane when for example the feedback coefficient is varied. This is shown in figure 5.3 where the contour plots are drawn for three values of the feedback coefficient r_a : -0.01, -0.05 and -0.09. With a feedback coefficient of -0.01 the three poles are clearly separated. The lowest pole lies at a frequency of 0.35 Hz. The transit time through the riser is 1.27 seconds, so $f = 1/(2.2\tau_r)$. The second pole lies at 0.77 Hz. As the feedback coefficient rises the first pole moves to the left and the second pole moves to the right. Thus the nuclear feedback has a stabilizing effect on low-frequency oscillations. This is of course caused by the negative feedback coefficient: any deviation of the void-fraction causes an opposite effect on the power which drives the void-fraction back to the equilibrium value. In the right figure, with a feedback coefficient of -0.09 these trends continue.

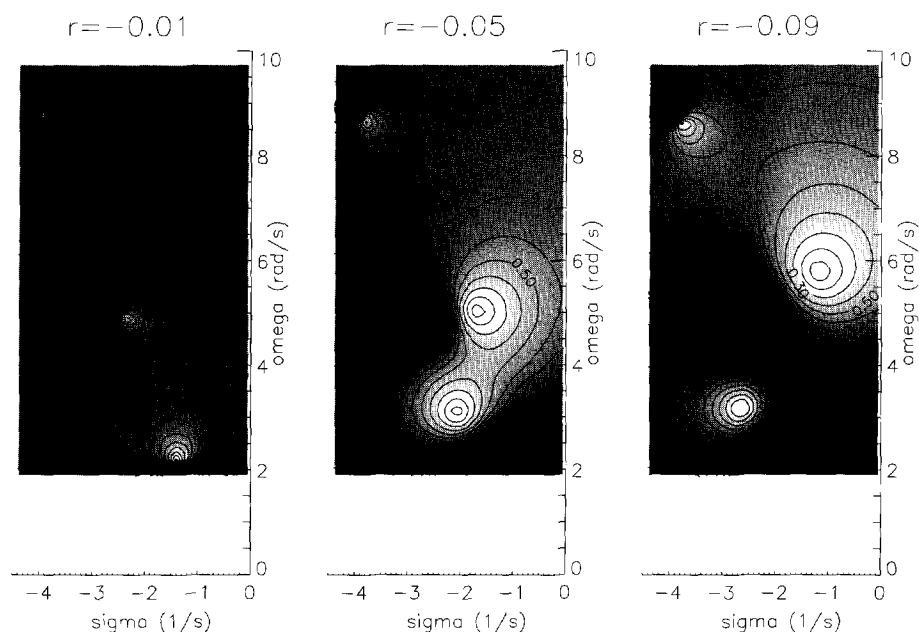


Figure 5.3 The effect of the feedback coefficient on the magnitude of the denominator of the transfer function.

The fuel time constant is another key parameter for the stability of a BWR. It plays a dual role of providing additional phase shift between power and heat transfer to the coolant and of attenuating higher frequency oscillations. At a certain fuel time constant the system is the least stable. Fuel with a smaller time constant will not provide enough phase shift between power and heat flux. For slower fuel the frequencies at which oscillations can occur are attenuated by the fuel. These effects can be seen in figure 5.4. The leftmost figure shows a system with very fast fuel ($\tau_f=0.1$ s). When the fuel time constant is increased to 0.5 s both the first and the second pole move to the right becoming less stable. This is caused by the additional phase shift that the fuel now provides. At an even higher fuel time constant the first pole continues moving to the right slightly, but the second pole moves back to the left.

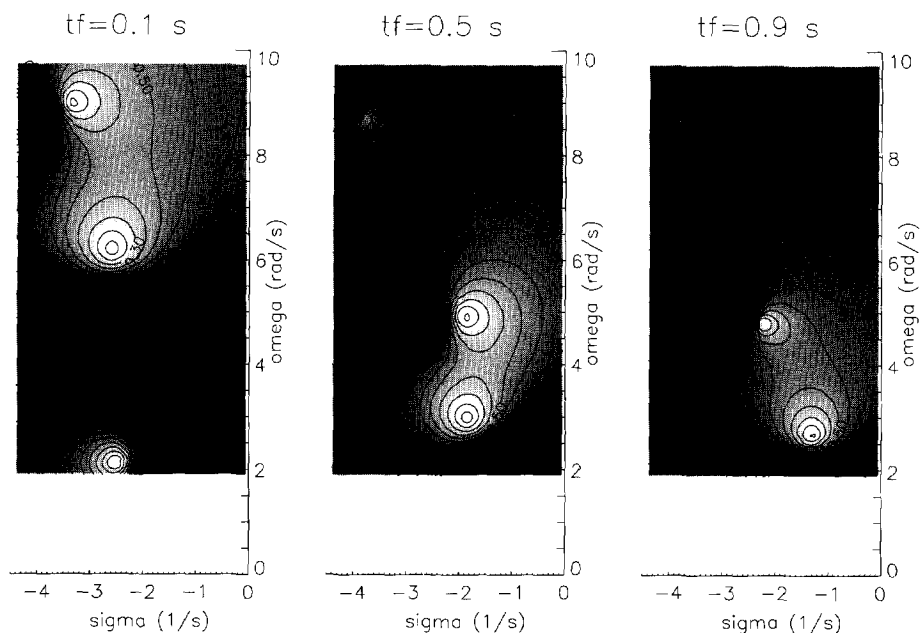


Figure 5.4 The effect of the fuel time constant on the magnitude of the denominator of the transfer function.

The dominating pole is the pole that is the least stable. Which of the poles is the least stable depends on many variables. In figure 5.5 root-loci diagrams are shown in the s -plane and in the corresponding frequency/decay-ratio plane. In the left two figures the void-reactivity coefficient was varied from -0.001 to -0.1. The first pole reaches a maximum in the decay-ratio for a void-reactivity coefficient of about -0.03, it is always more stable than the second pole, which becomes less stable as the void-reactivity coefficient increases. The third pole is hardly influenced by the void-reactivity coefficient.

The two figures in on the right of figure 5.5 show the paths of the poles as the fuel time constant is increased from 0.1 seconds to 1 second. The decay-ratio of the first pole keeps increasing as the fuel time constant increases. The second pole reaches a maximum for a fuel time constant of 0.25 seconds, while the third pole becomes more stable as the fuel time constant increases. It is interesting to see that at a fuel time constant of 0.1 seconds the third pole is the dominating one, at 0.15 s the second pole becomes dominating and at approximately 0.9 s the first pole is the least stable one.

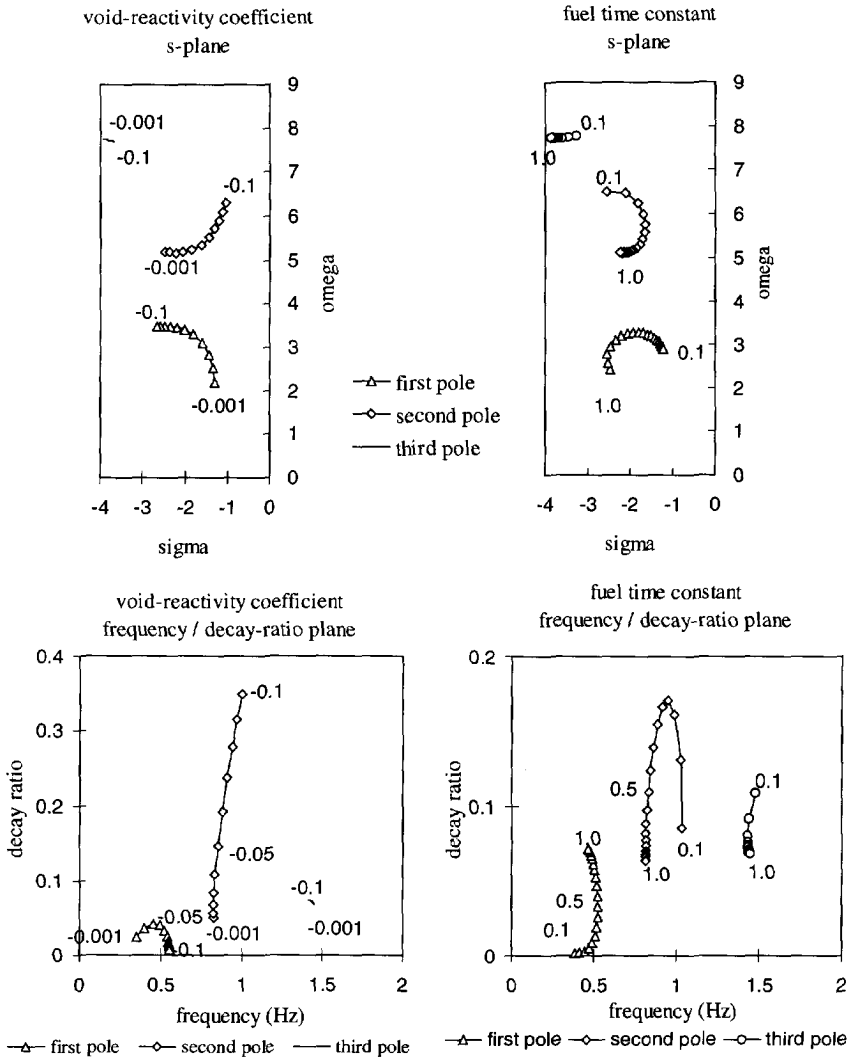


Figure 5.5 Root-loci diagrams of the closed loop transfer function for a variation in the void-reactivity coefficient and the fuel time constants in the s-plane and the frequency/decay-ratio plane.

Many thermal-hydraulic parameters, such as power, flow rate, subcooling and pressure have an effect on the stability. It proves to be useful to write the equations of the stability model in a non-dimensional form. For a natural circulation system and assuming a homogeneous flow model only two dimensionless numbers are needed to characterize the thermal-hydraulics (Van Bragt and Van der Hagen, 1998). These are the Zuber number and the subcooling number, see

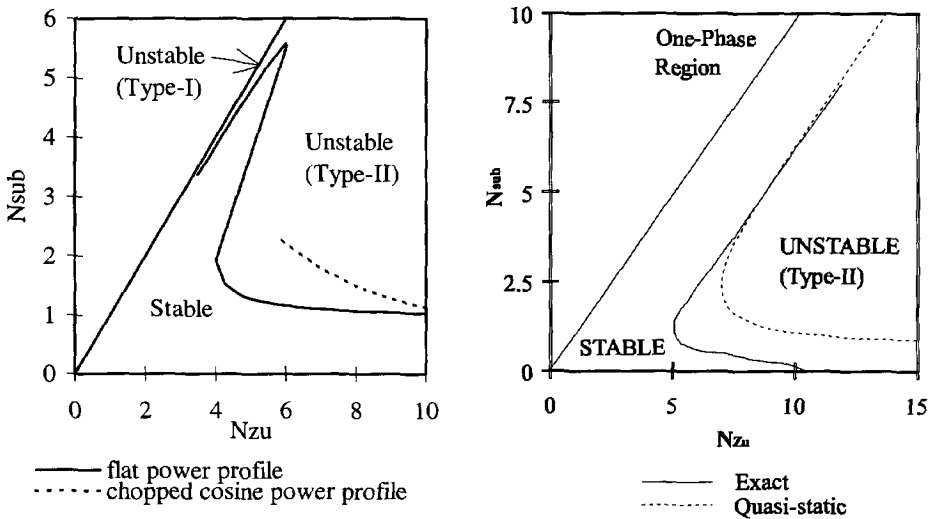


Figure 5.6 Typical stability map of a natural circulation boiling channel with a riser. The stability boundary is shown for a flat power profile and for a chopped cosine power profile in the left figure. In the right figure the effect of the quasi-static approximations used in equation 5.6 can be seen (Van Bragt, 1997).

equation 2.11. In the Zuber-subcooling plane the stability boundary is insensitive to the pressure of the system.

A typical example of a stability boundary is shown on the left of figure 5.6. Two regions of instability are identified: Type I and Type II oscillations (Fukuda and Kobori, 1979).

The quasi-static approximation used in equation 5.6 have a profound effect on the stability boundary, as can be seen on the right of figure 5.6. One particular effect of the neglecting of wave-like phenomena in the model is that the model is always stable for zero subcooling. That is, the boiling boundary dynamics are necessary to provide additional phase shift in the loop transfer function. It must be noted that a second approximation in the model, the neglecting of subcooled boiling can partly compensate for the increased stability due to the quasi-static approximation, as it is believed that the presence of subcooled boiling works stabilizing (Van Bragt, personal communication).

Increasing the Zuber number always has a destabilizing effect on the Type II oscillations. The effect of the subcooling is more complicated. At low subcooling increasing the subcooling number is destabilizing. However, at very high subcooling number the flow in the channel is mostly one-phase and increasing the subcooling further can be stabilizing.

The Type I oscillation only occurs in the presence of a riser. These oscillations are caused by gravitational pressure drop in the riser and occur only at low exit qualities (Zuber number only

slightly larger than subcooling number). Although the physical mechanism for the two types of oscillations are different (friction in assembly versus gravity in riser) the model predicts a gradual change from one type to the other type. For Type I oscillations the first pole in figures 5.3 becomes dominating, while for the Type II oscillations it is the second pole that dominates.

Both types of instability are thermal-hydraulic in nature, they are also present without the void-reactivity feedback. However, the void-reactivity feedback has a large effect on the position of the stability boundary. In general the Type I (low frequency) oscillations are stabilized by the void-reactivity feedback, while the Type II (high frequency) oscillations are destabilized (see figure 5.5). Both types of oscillations have been observed in the Dodewaard BWR (Van der Hagen et al., 1997).

The general shape of the stability boundary shown in figure 5.6 has been extensively reported in the literature (Rizwan-uddin and Dorning, 1986; Lin and Pan, 1994; Lee and Lee, 1991; Wang, Hu and Pan, 1994, Van Bragt and Van der Hagen, 1998). Also experimental work has been done on boiling channels (without feedback) where the same kind of channel instability is present (Saha, et al., 1976; Rizwan-uddin and Dorning, 1986; Furuya, et al., 1997). However, experimental work on the combined thermal-hydraulic and nuclear systems is very limited, for obvious reasons. A solution to this problem is to extend thermal-hydraulic facilities with simulation of the neutronics. Such a hybrid approach can provide a link to the extensive theoretical work on coupled systems and the experimental work on purely thermal-hydraulic systems. DESIRE was fitted with a simulated void-reactivity feedback to create such a hybrid system.

5.3 *Feedback simulation in DESIRE*

5.3.1 *Overview and scaling of the nuclear feedback*

A crucial assumption for the feedback simulation is that the thermal-hydraulics in the real reactor and in DESIRE can be assumed to be the same providing we account for the thermal-hydraulic scaling. In that case we can duplicate the void-reactivity feedback as present in a reactor in DESIRE by the addition of several transfer functions.

At the top of figure 5.7 the void-reactivity loop for a reactor is shown. The hybrid system using DESIRE is shown in the middle. Notice that this hybrid system contains several blocks which are not present in the real reactor, notably the void-fraction sensor (G_m) and the power supplies (G_{ps}). These two systems are inherent to the system and cannot be removed. Therefore the simulation must eliminate the effects of these by including the inverse transfer function of both. Another difference between the hybrid system and the reactor are the fuel rods. The time constant of the DESIRE rods is different from the time constant of the reactor fuel rods. Thus to fully account for the fuel heat transfer an additional block is added to the simulation. All the transfer function used in the simulation are shown in the bottom of figure 5.7.

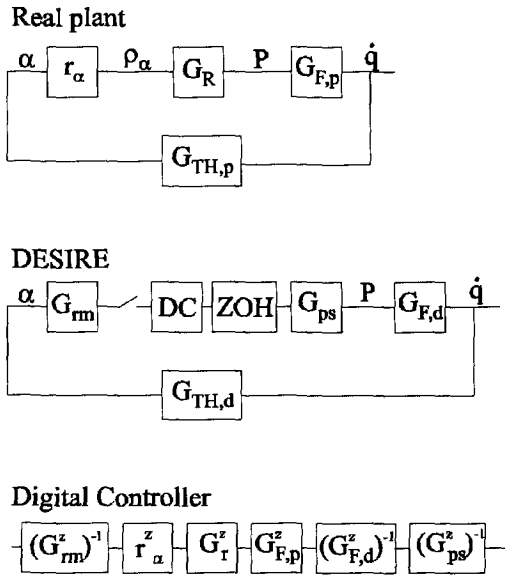


Figure 5.7 Void-reactivity feedback loops for the real plant compared to the DESIRE facility and the Digital Controller. G_x are transfer functions in continuous time, G_x^z are transfer function in discrete time.

Signals	
α	void-fraction
ρ_α	void-reactivity
P	Power
\dot{q}	Heat flux from fuel to coolant
Transfer functions	
r_α	void-reactivity coefficient
G_R	Zero-power reactivity to power
$G_{F,p}$	Power-heat flux of plant
$G_{TH,p}$	Thermal-hydraulics of plant
G_{rm}	Ratemeter
DC	Digital Controller
ZOH	Zero-Order Hold circuit
G_{ps}	DESIRE power supplies
$G_{F,d}$	Power-heat flux of DESIRE
$G_{TH,d}$	Thermal-hydraulics of DESIRE

Table 5.2 Meaning of signals

The different transfer functions in figure 5.7 will now be discussed:

Void-to-reactivity transfer function (r_a)

This is a simple multiplication of the void-fraction with the void-reactivity coefficient. The void-reactivity coefficient can be input by the user to any value. Since the void-fraction is properly scaled 1:1 between DESIRE and Dodewaard the void-to-reactivity transfer function is also scaled 1:1. So the void-reactivity coefficient has the same numerical value in DESIRE as in Dodewaard.

Zero-power reactor transfer function (G_R)

The reactor transfer function is treated differently in the simulation than in the model. In the model the point kinetics equations were linearized to obtain a transfer function. In the simulation this approximation is not necessary. The point kinetics equations can be simulated directly.

The starting point for the reactor simulation are the point kinetics equations 5.1 and 5.2. Next the prompt-jump approximation is applied. This is a valid approximation for the low frequencies considered here. However, the reactivity must not exceed the delayed neutron fraction. Thus the magnitude of the void-fraction fluctuations limits the maximum void-reactivity coefficient which is valid. Values for the delayed-neutron fraction and decay constant of this group can be input by the user.

In the prompt jump approximation the dn/dt term in equation 5.1 can be neglected. This results in:

$$n(t) = \frac{\Lambda}{\beta - \rho(t)} \lambda c(t) \quad (5.11)$$

$$\frac{dc(t)}{dt} = \frac{\beta}{\Lambda} n(t) - \lambda c(t) \quad (5.12)$$

Note that these equations are not dependent on the absolute value of neutron and neutron precursor concentrations. Both can be multiplied by a constant without changing the equations. This means that the scaling of the power from Dodewaard to DESIRE has no effect on the equations. However, the time variable does have an important consequence. As shown in section 2.3.1 and table 2.2 the channel transit time in DESIRE is smaller than in Dodewaard by a factor of 0.68. This channel transit time is considered as the characteristic time in DESIRE because it plays an important role in the density wave oscillations. To account for this difference in time we must apply a scaling procedure to the point kinetics equations.

First we substitute equation 5.11 in equation 5.12, which gives

$$\frac{dc(t)}{dt} = \lambda c(t) \left[\frac{\rho(t)}{\beta - \rho(t)} \right] \quad (5.13)$$

To non-dimensionalize this equation with respect to time we divide by λ . This gives the following non-dimensional group:

$$N_t = \lambda t \quad (5.14)$$

where we have replaced dt by the more general term t . Proper scaling is now achieved by using a λ in the simulation that is 1.47 as large as the λ for Dodewaard.

To implement these equations on a computer they must be discretized. The void-fraction is sampled with a sample time of Δt by the analog-digital converter. We define the quantities t_n , ρ_n and c_n as the time, reactivity and delayed-neutron precursor concentration for the n^{th} sample. The reactivity is taken to be constant between two samples:

$$\rho(t_{n-1} < t < t_n) = \rho_n \quad (5.15)$$

The delayed-neutron precursor concentration is linearly interpolated between two samples:

$$c(t_{n-1} + t) = c_{n-1} + \frac{c_n - c_{n-1}}{\Delta t} t \quad \text{for } 0 < t < \Delta t \quad (5.16)$$

We can now integrate equation 5.13 between two samples:

$$\int_{t_{n-1}}^{t_n} \frac{dc(t)}{dt} dt = \int_{t_{n-1}}^{t_n} \lambda c(t) \left[\frac{\rho_n}{\beta - \rho_n} \right] dt \quad (5.17)$$

which gives

$$c_n - c_{n-1} = \frac{\lambda \rho_n}{\beta - \rho_n} \frac{c_n + c_{n-1}}{2} \Delta t \quad (5.18)$$

or after rearranging

$$c_n = c_{n-1} \frac{1 + a_n}{1 - a_n} \quad (5.19)$$

$$a_n = \frac{\frac{1}{2} \lambda \Delta t \rho_n}{\beta - \rho_n}$$

These equation can be implemented very efficiently on a computer. The power can be calculated directly from the delayed neutron precursor concentration using equation 5.11.

Power-to-heat flux transfer function of the plant ($G_{F,p}$)

The transfer function of the power to the heat flux is represented as a simple first order system (equation 5.4). The fuel time constant can be input by the user. Scaling of this equation with respect to time is straightforward and leads to a fuel time constant for the DESIRE fuel rods that is smaller than the fuel time constant of Dodewaard by a factor of 0.68.

Heat-flux to void-fraction transfer function ($G_{TH,p}$)

This transfer function is very complicated. It contains the interaction of the void-fraction with the natural circulation flow and the dynamics of the boiling boundary. It is assumed that this transfer function is the same in the real plant (Dodewaard) as in the scaled assembly (DESIRE).

Ratemeter transfer function (G_m)

The void-fraction is measured using the gamma-transmission technique. The counts coming from the detector are converted to a continuous signal using a ratemeter. This ratemeter averages the counts over a time interval, which can be set to different values. This has the effect of a low-pass filter. The transfer function of the ratemeter has been determined experimentally.

Power supply transfer function (G_{ps})

The transfer function of the power supply was determined experimentally. This was done by connecting a white noise source to the input of the digital controller and bypassing all calculations. Thus the transfer function of the digital controller was $G=1$. Only the zero-order hold circuit and the power supply contributed to the transfer function between the white noise signal and the measured voltage. The gain and phase of the measured transfer function is shown in figure 5.8. The transfer function of the power supplies was not dependent on the average power.

It can be seen from the phase behaviour that the power supply is not a simple first order system. Time series analysis was used to fit an ARMA (Priestley, 1981) model to the measured data. In order to be able to use this model it had to be invertible (the inverse model must be stable). The best model which satisfies this requirement is an ARMA(2,2) model. The use of the inverse of this model in the digital simulation is also shown in figure 5.8. As can be seen there is a definite improvement, the transfer function is reasonably flat up to 2 Hz.

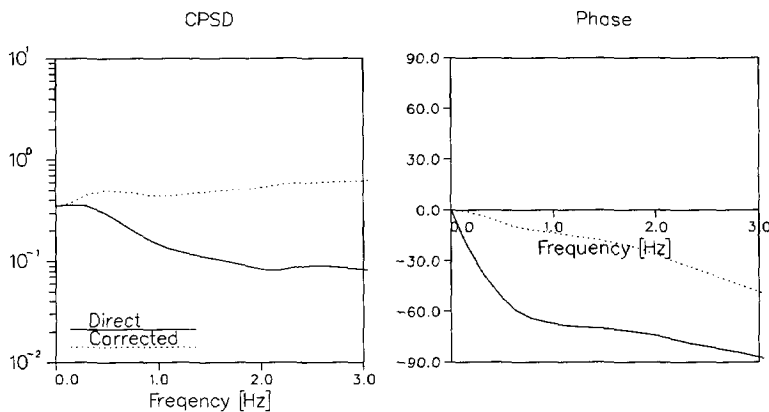


Figure 5.8 Transfer function of the power supplies with and without correction from the digital controller.

Power-to-heat flux transfer of the DESIRE fuel rods ($G_{F,d}$)

This is basically the same transfer function as the power-to-heat flux transfer function in the real reactor. Only the time constants are different. The time constant of the DESIRE fuel rods are not exactly known, but calculations using the material properties and some assumptions on the boundary layer thickness of the coolant flow give a value of about 0.5 seconds. This value is supported by measurement of the power to void-fraction transfer function in DESIRE (see section 6.2.3). As stated in section 5.2.1 the effective fuel time constant for the Dodewaard reactor is about 2 seconds. Since the time is scaled by a factor of 0.68 this is equivalent to 1.36 seconds in DESIRE. This means that the DESIRE fuel rods are two to three times as fast as the Dodewaard fuel rods.

Several transfer functions which are used are given in table 5.3.

	Model		DESIRE
G_r	prompt jump model	G_r^z	equation 5.19
$G_{F,p}$	$\frac{1}{1+s\tau_{f,p}}$	$G_{F,p}^z$	$\frac{1-e^{-T/\tau_{f,p}}}{1-e^{-T/\tau_{f,p}}z^{-1}}$
		$G_{F,d}^z$	$\frac{1-e^{-T/\tau_{f,d}}}{1-e^{-T/\tau_{f,d}}z^{-1}}$
		G_{rm}^z	Measured ARMA model
		G_{ps}^z	Measured ARMA model

Table 5.3 Transfer functions used in the simulation. T is the sample time and τ_x are fuel time constants. Subscripts: d = DESIRE and p = power reactor.

5.3.2 Implementation

Void-fraction measurement

The void-fraction is measured using the gamma-transmission method. The main criterion for the design of this system is speed. The measurement must be fast enough to allow the void-fraction to be measured without a large phase lag at the frequencies of interest. Thus a strong source is necessary and collimation should be minimized. A source emitting gammas of sufficient energy to penetrate the stainless steel assembly casing would be ideal. As seen in chapter 3 this requires a minimum gamma energy of roughly 300 keV. Unfortunately a strong source of this energy would require a large amount of shielding. An alternative is to use a lower energy source and to position the beam to pass through the viewing ports instead of through the stainless steel. This allows the use of a 310 mCi Americium source (60 keV) which requires no additional shielding. This source in combination with the efficient BGO detector that was also used for the experiments in chapter 3 resulted in a count rate varying from 15,000 to 40,000, depending on the void-fraction.

The counts coming from the detector are converted to a continuous signal by a ratemeter. This ratemeter averages the counts over a time interval that can be set to different values. A short time interval will give a signal with high uncorrelated noise due to the Poisson statistics of the radioactive source. A long time interval reduces this noise but also leads to a larger phase shift. Usually a time constant of 30 or 100 ms is used.

A more fundamental problem with this void-fraction measurement method is that it is local, while the void-reactivity depends on the axial void-fraction distribution. A partial work-around is to calculate the axial void-fraction profile from the measured void-fraction. This is done by assuming a linear thermodynamic equilibrium quality profile. In that case the quality over the whole assembly is completely determined by the quality at the inlet of the assembly (the subcooling) and the quality at the measurement point. The following calculational steps are performed:

- calculate the local void-fraction from the ratemeter signal using equation 3.4.
- calculate the local quality using the HEM model (equation 2.6).
- using the inlet quality and the measured local quality calculate the average quality over the two-phase region.
- from the average quality calculate the average void-fraction with:

$$\langle \alpha(t) \rangle = \frac{1}{2 \langle x(t) \rangle \left(1 - \frac{\rho_g}{\rho_l}\right)^2} \left(\left(1 - \frac{\rho_g}{\rho_l}\right) 2 \langle x(t) \rangle - \frac{\rho_g}{\rho_l} \ln \left(2 \langle x(t) \rangle \left(\frac{\rho_l}{\rho_g} - 1 \right) + 1 \right) \right) \quad (5.20)$$

which is obtained by integration of the void-quality relation over the length of the assembly assuming a linear quality profile (Stekelenburg, 1994).

The approximation of a linear quality profile is used twice in this procedure. The first time in the calculation of the average quality and the second time in the calculation of the average void-fraction from the average quality. This second approximation is fairly accurate, but the first approximation is only applicable if the measurement point is near the center or at the top of the assembly (at these two points the quality is the same for all symmetric quality profiles). The second and third viewing ports lie at approximately 40% and 60% of the assembly height, so the approximation is reasonable.

It is possible to take the power profile fully into account. However, the model against which the measurements will be compared uses the same approximation. There is a trade-off in matching the simulation as close as possible to the real nuclear reactor or to the model that will be used to analyze the results.

Digital controller

The digital controller implements the necessary transfer functions to simulate the void-reactivity feedback. It is implemented in a 486 PC and uses a sample time of 25 ms. The following parameters can be varied: void-reactivity coefficient, fuel time constant, delayed-neutron fraction and the decay constant of the delayed neutrons (one group). Besides the power fluctuations due to the void-reactivity, it is possible to induce random power fluctuations, which can be used to introduce noise into the system which is sometimes necessary for performing noise analysis.

5.3.3 Caveats and approximations

power supply

In the previous section it was shown that the transfer function of the power supplies is not acceptable. The problem was solved by implementing an inverse model of the measured power supply transfer function in the digital controller. A drawback of this method is that the inverted power supply model amplifies the higher frequencies. The input to this model contains noise resulting from the Poisson statistics of the gamma void-fraction measurement. The higher frequency components of this noise can saturate the output of the model, since the control signal to the power supplies is limited to the range of 0-10 Volts. Therefore it is necessary to attenuate the higher frequencies. This can be done by selecting a higher time-constant on the ratemeter, which has as a drawback that an extra phase lag is introduced into the feedback loop. A compromise between noise and phase lag must be made. To make sure that the output of the inverted power supply model does not saturate an overload warning is given during the simulation. If this happens regularly then a longer time constant for the ratemeter must be chosen.

Even using a noise-free measurement technique there is a limit to the amplitude of the oscillations that the power supplies can handle. If the loop becomes less stable the oscillations

can become so large that either the control signal to the power supply saturates or the power supply is no longer properly described by the ARMA(2,2) model. That is the reason we cannot do realistic measurements near the stability boundary, where the oscillations become large.

A final remark about the power supplies is that they produce an interference which is picked up by all the sensors of DESIRE. This interference is proportional to the power, sometimes creating an illusion of a high correlation between a signal (flow rate, temperature etc.) and the power. This only happens if the signal is very weak or has no other AC components in a particular frequency range.

gain and phase of void-fraction measurement

Our method of void-fraction measurement poses some other problems besides those mentioned above. To understand the problem consider the table below where three systems are categorized with respect to three phenomena (void formation and propagation, two-phase friction and void-reactivity).

	Dynamic (wave phenomena)	Quasi-static (no wave phenomena)
<i>Void formation and propagation</i>		
	Dodewaard DESIRE	analytical model
<i>two phase friction</i>		
	Dodewaard DESIRE	analytical model
<i>void-reactivity</i>		
global	Dodewaard	analytical model DESIRE
local	DESIRE	

Table 5.4 This table categorizes the analytical model, Dodewaard and DESIRE. Three physical processes (void formation and propagation, two-phase friction and void-reactivity) are treated either dynamic or quasi-static. In the void-reactivity a further distinction is made between global and local.

The void formation and propagation in DESIRE and in Dodewaard are fully dynamic, while in the model a quasi-static approximation is used. This also applies to the two-phase friction, since it is determined by the void-fraction.

For the third phenomena in table 5.4, the void-reactivity, a further distinction is made between local and global. This means that the void-reactivity is determined either by a local void-fraction or by the global void-fraction distribution. In a nuclear reactor the void-fraction over

the whole core affects the power. Also there is no quasi-static approximation. In the analytical model the void-fraction over the whole core affects the power, but it is calculated using a quasi-static approach.

Note that in a nuclear reactor it is not the average void-fraction which determines the void-reactivity. The reactivity effect of a bubble depends on the position in the core. In a first approximation the reactivity effect of a bubble scales with the square of the neutron flux. The neutron flux shape in the reactor depends among other things on the fuel burnup, control rod position and on the void-fraction distribution (Duderstadt and Hamilton, 1976). This makes the wave phenomena in a real reactor more important: as the void fluctuation travels along the assembly its contribution to the void-reactivity changes significantly.

In DESIRE the void-reactivity is a combination of local/dynamic and integral/quasi-static. In effect we have split the fuel assembly into two regions: below and above the measuring point. The wave-like propagation below the measuring point affects the void-fraction measurement. The detection of a void-change below the measuring point will be delayed by the travel time of the void perturbation to the measuring point. In contrast, when the change has been detected it instantaneously affects the calculated void-fraction for the *whole* assembly. Thus the calculated void change will precede the real change of void along the rest of the assembly. These two effects, the delay of the void perturbation detection and the instantaneous adjustment in the rest of the assembly, give the average void-fraction a phase lag respectively a phase gain compared to the local void-fraction. The net effect of these can be either negative or positive. There exists a point along the assembly where the local void-fraction is exactly in phase with the average void-fraction. Unfortunately the position of this point depends on the power, flow rate and subcooling. For DESIRE simulations were performed to determine which viewing port would be the best for the typical operating conditions. These simulations showed that the viewing port at 40% height showed a slight phase gain, while the viewing port at 60% generally had a significant larger phase lag. Also the phase shift at the viewing port at 40% was less sensitive to the operating conditions.

A final consideration for the choice of this viewing port is that a slight phase gain is in fact not so bad, since the ratemeter already introduces extra phase loss into the feedback loop. The phase shift of the ratemeter was determined experimentally. It was found that for short time constants (0.03s and 0.1s) and low frequencies (0-1Hz) the phase lag was an almost linear function of frequency. This corresponds to a simple time delay with the delay time equal to the time-constant of the ratemeter. So the ratemeter can be considered to respond to void-fraction fluctuations with a delay of 0.03 respectively 0.1 seconds. During this time and under typical operating conditions the void perturbation flows upwards between roughly 5 and 20 cm. This means that the real response of the ratemeter can be considered as an instantaneous local measurement somewhere between the second and third viewing port.

5.3.4 Improving the feedback simulation

When the measuring point of the void-fraction for the feedback simulation is taken to be rather low in the assembly, which may be desirable for the phase behaviour, the calculation of the average void-fraction from the local void-fraction becomes very sensitive to the subcooling. This can be seen as follows. The quality profile in the assembly is completely determined by the quality at two points, just as a line is defined by two points. The first point is the point where the void-fraction is being measured. The only other point where the quality is known is at the assembly inlet, where the subcooling is measured. If these two points lie closer together then the measurement errors in the quality at the two points will give a larger error in the average quality.

To demonstrate that the difference between local and average void-fraction fluctuations are not negligible we perform the following analysis. Since the reactivity is the product of the void-fraction fluctuations and the void-reactivity coefficient larger void-fraction fluctuations are equivalent to a system with a larger void-reactivity coefficient. Thus instead of calculating the average void-fraction in the simulation we can use the local void-fraction and compare this with the model using an effective void-reactivity coefficient. This effective void-reactivity coefficient is given by:

$$r'_\alpha = r_\alpha \frac{\partial \alpha_z}{\partial x_z} \frac{\partial x_z}{\partial \langle x \rangle} \frac{\partial \langle x \rangle}{\partial \langle \alpha \rangle} \quad (5.21)$$

The first partial derivative is given by the slope of the void-quality relation for the quality at height z in the assembly, which again depends on the subcooling. The second partial derivative depends only on the power profile and the height z . Finally, the third partial derivative can be found using equation 5.20.

The ratio between the effective void-reactivity coefficient and the void-reactivity coefficient is shown in figure 5.9 as a function of subcooling and measurement height. From this graph one can conclude that neglecting the difference between the local and the global quality profile (i.e. not performing the four steps described in section 5.3.2) can give totally wrong results.

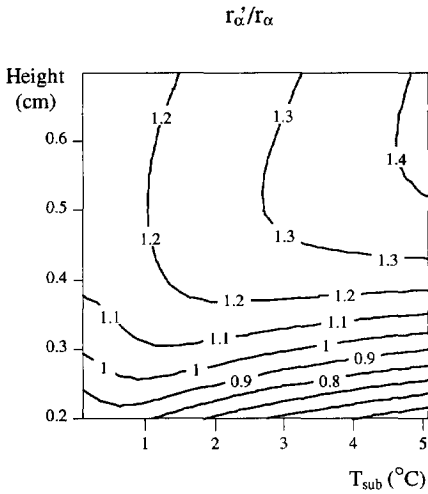


Figure 5.9 Contour plot of the ratio between r'_α and r_α as a function of subcooling and void-fraction measuring height.

As stated before, a different problem associated with the local void-fraction measurement is that the local void-fraction fluctuations result in a noisy signal. This is made even worse by the measurement method: the gamma attenuation technique, which adds the Poisson noise inherent to this technique. Although these higher frequency noise components should have little effect on the dynamics of the system they do pose a problem in the simulation, as they can saturate the signal driving the power supply. Since these superficial fluctuations are additive to the real power fluctuations, and the amplitude of the power oscillations is limited by the power supplies the amplitude of the real power fluctuations are limited by these higher frequency noise components. This limits the possibility to study DESIRE in less stable situations, and the possibility to investigate non-linear effects. In particular, if one wants to have any hope of finding a stable limit cycle in DESIRE there must be as little noise in the void-fraction signal as possible.

With regard to the problem of noise and the comparison of non-linear systems to linear models the following quotation from a paper by Achard, Drew and Lahey (1985) seems applicable:

"In spite of the inherent limitations of linear analysis, it is often compared with experimental stability thresholds measured in the presence of a fairly high level of noise. Any discrepancies between theoretical predictions and experimental results are usually attributed to simplifications in the analytical model used. While that possibility is always likely, other possibilities exist; indeed, in the case of a subcritical bifurcation, the linear-stability boundary may be quite far from the actual stability boundary for noisy flows."

The solution to all the problems mentioned above is to use a different void-fraction measurement technique. One promising technique is the capacitive measurement technique (Kok et al., 1995; Olsen, 1967; Heerens, 1991). In this technique two or more electrodes are inserted into the flow and the capacity between these electrodes is measured. The advantages of this technique are its speed, and the possibility of measuring the average void-fraction by using long electrodes. In fact there are many different ways one could implement this technique. One could use long electrodes to measure the average void-fraction, or shape the electrodes in such a way that the capacity is more sensitive to the void-fraction at certain

heights. In this way the capacity would depend on a weighted function of the void-fraction. One obvious possibility is to weight the void-fraction with the square of the fundamental mode of the neutron flux in a reactor.

The main difficulty will be the placement of the electrodes without disturbing the flow too much. A simple way would be to replace one of the fuel rods with an isolating hollow dummy rod. Cylindrical electrodes could be placed inside the rod over the whole length except at the positions of the spacers (which would cause a very large capacitance independent on the void-fraction). The surrounding grounded fuel rods would serve as the other electrode. Calibration of the capacitance of this system against the void-fraction could be performed with the gamma absorption technique presented in chapter 3.

Because this method measures the average void-fraction directly there are no problems with phase or amplitude differences as in the case of a local void-fraction measurement technique. Also both sources of noise in the presently used method, local void-fraction fluctuations and Poisson noise, are eliminated. This will make it easier to study larger amplitude oscillations and non-linear effects.

5.3.5 *Test measurement of a positive reactivity insertion*

To illustrate the operation of the void-reactivity feedback a measurement was performed of the effect of a positive reactivity insertion of 0.4 \$ (the reactivity expressed in dollars is defined as the reactivity divided by the delayed neutron fraction, so in this case $\rho = 0.4 \beta = 0.0026$). Four time signals were recorded: the power, void-fraction, flow rate and temperature at the inlet of the assembly. The result is shown in figure 5.10.

Directly after the reactivity insertion the power makes a jump. This is followed almost immediately by a jump in the void-fraction. Due to the negative void-reactivity coefficient this immediately negates a large part of the excess reactivity and the power makes a smaller, negative jump. Within a few seconds these oscillations damp out.

After the prompt jump of a reactivity insertion the power would normally start increasing exponentially. But in this case a gradual increase of the temperature at the inlet of the assembly gives rise to an increasing void-fraction during the first 15 seconds. This means that the reactivity is decreasing during this period. The net effect of the positive but decreasing reactivity is that the power remains almost constant. After this period the temperature at the inlet starts to fall. The growth of the void-fraction stops and the power starts rising again because the net reactivity is still positive. The rising power and the falling inlet temperature have an opposite effect on the void-fraction, so for a while the void-fraction changes only a little. When the inlet temperature drop decreases the void-fraction increases again and reaches an equilibrium value, as does the power.

The inlet temperature thus plays an important role in the long term response to a reactivity insertion. The response of the inlet temperature to the reactivity insertion is determined by the carry-under and feedwater dynamics. The following scenario explains the observed inlet temperature trends. Immediately after the reactivity insertion the inlet temperature rises by about 0.1 °C. Looking closely at the first few oscillations in the temperature we can see it follows the power directly. This is caused by the interference from the power supply. In reality the inlet temperature does not change until some 15 seconds after the reactivity insertion, which is the time it takes the flow to travel from the riser exit to the assembly inlet. The rise in the temperature is caused by an increasing carry-under due to the higher void-fraction and circulation flow rate. The increase of the cold feedwater flow rate gives a decrease in the inlet temperature. It is the exact timing of the feedwater flow rate increase that determines when the positive effect of the carry-under on the inlet temperature is negated by the negative effect of the increase of the cold feedwater flow rate. This timing is among others determined by the characteristics of the liquid level controller. When the void-fraction is suddenly increased in the assembly the liquid level in the riser section increases. The liquid level controller reacts by reducing the feedwater flow rate until the setpoint for the liquid level is reached.

The equilibrium value of the void-fraction before and after the reactivity insertion can be calculated. Since equilibrium is reached when the total reactivity equals zero we can write:

$$\rho_{ext} + \rho_{\alpha} \equiv 0.4\beta + r_{\alpha} \Delta\alpha = 0 \quad (5.22)$$

with $r_{\alpha} = -0.04$ and $\beta = 0.0065$ this gives $\Delta\alpha = 6.5\%$. This coincides with the void-fraction change from 26 % to 33%.

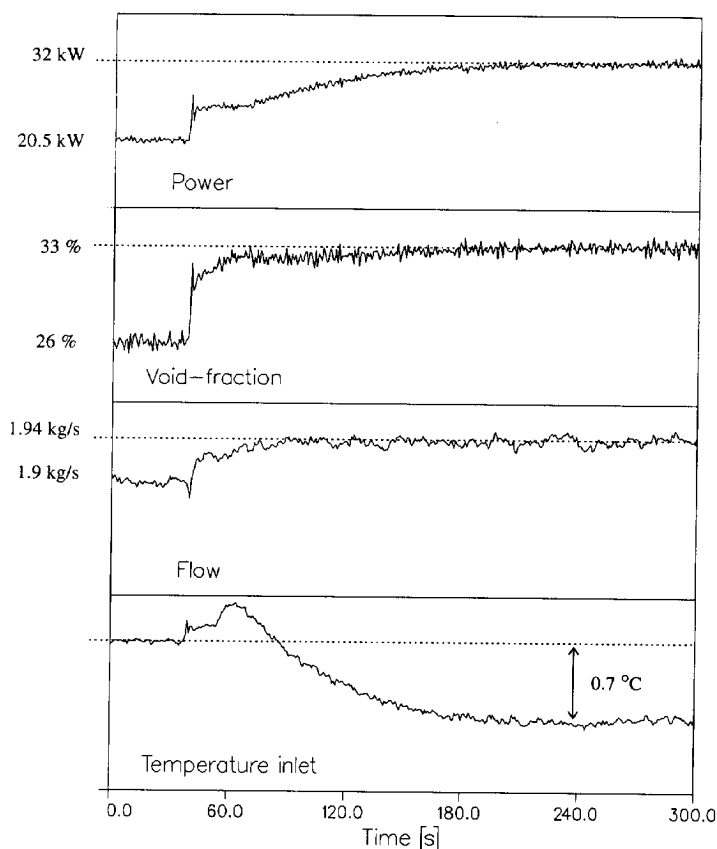


Figure 5.10 Result of a positive reactivity insertion of 0.4 \$.

5.4 Conclusions

In this chapter a model of the dynamics of a natural circulation boiling water reactor developed by Van Bragt was described. The model was adopted to DESIRE by changing the appropriate dimensions and parameters of the model. For the friction factors the values that were found in chapter 4 are used. The poles of the model were calculated as a function of the void-reactivity coefficient and the fuel time constant. The root-loci diagrams show that the second pole (from low to high frequency) is generally the least stable. This pole always becomes less stable for increasing void-reactivity coefficient. In contrast, there is a maximum in the decay ratio of this pole as a function of the fuel time constant. This maximum lies at $\tau_f = 0.25$ s, which is faster than the DESIRE fuel rods. So in the experiments with DESIRE increasing the fuel time constant should always have a stabilizing effect.

With respect to the model, only two dimensionless number are needed to characterize the thermal-hydraulics of a natural circulation system: the Zuber number and the subcooling number. The stability boundary in this plane shows the existence of two regions of instability: Type I and Type II. The position of the stability boundary depends strongly on the void-reactivity coefficient but also on the value of the inlet friction factor.

To be able to investigate nuclear-coupled thermal-hydraulic instabilities DESIRE was fitted with a simulated void-reactivity feedback. The implementation of this feedback has been described. The void-fraction is measured using the gamma-attenuation technique. This is a local measurement technique. In contrast, the model uses the average void-fraction in the neutronic feedback. To conform the experiments with the model the average void-fraction is calculated from the local void-fraction and the subcooling in the simulation.

The transfer functions of the power supply and ratemeter are accounted for in the simulation. The experimenter can input values for the void-reactivity coefficient and the fuel time constant as well as several other neutronic parameters. A noise source can be connected to the input of the inverse power supply transfer function in the model. With the void-reactivity turned off this allows the user to have the power supplies produce power fluctuations with a (banded) white noise spectrum. This can be useful for determining individual transfer functions in DESIRE.

Chapter 6

Experimental investigation of the dynamics

The dynamics of the DESIRE loop with and without simulation of the void-reactivity feedback is investigated and compared to the model presented in chapter 5. The response of the natural circulation loop is studied using noise analysis. This technique allows us to measure various transfer functions of DESIRE, and to characterize the stability of the system. In section 6.1 the noise analysis technique will be shortly outlined. Section 6.2 presents measurements where the power supply was driven by a white noise signal. These measurements reveal the purely thermal-hydraulic aspects of the dynamics. There is a reasonable agreement between the measured transfer functions and the dynamic model. The measurements where the void-reactivity feedback is included are given in section 6.3. There are large discrepancies between the predictions by the model and the measurements when the nuclear feedback is turned on. The approximations used in both the model and in the feedback simulation are too crude. In section 6.4 some recommendations will be given to improve the simulated feedback.

6.1 Noise analysis

Noise analysis can be used to extract information from a system without disturbing the system. Essential for this process is that the input signals have a noise component at all the frequencies where we wish to determine the transfer function. Often the input signals have sufficient intrinsic noise, otherwise noise must be added to the system in some way.

To demonstrate how the transfer function of a system can be determined consider a linear single-input, single-output system (see e.g. Priestley, 1981). In the frequency domain we can write:

$$Y(\omega) = G(\omega) X(\omega) \quad (6.1)$$

where $Y(\omega)$ and $X(\omega)$ are the Fourier transforms of the output signal and input signal respectively. $G(\omega)$ is the transfer function of the system. The auto power spectral density function (APSD) of, for example, the input signal is defined as:

$$APSD(\omega) = X^*(\omega) X(\omega) = |X(\omega)|^2 \quad (6.2)$$

and the cross power spectral density function (CPSD) between the input and the output signal is defined as:

$$CPSD(\omega) = X^*(\omega) Y(\omega) \quad (6.3)$$

The APSD and CPSD are related by the transfer function of the system:

$$G(\omega) = \frac{X^*(\omega) Y(\omega)}{|X(\omega)|^2} \quad (6.4)$$

From this equation it follows that the transfer function can be determined from the signals x and y , but only at those frequencies that are contained in the input signal x (otherwise $|X(\omega)|^2=0$).

The inverse Fourier transforms of the auto- and cross-power spectral density functions are the auto- and cross-correlation functions (ACF and CCF). These functions represent the data in the time domain rather than in the frequency domain and are often useful for understanding the physical processes taking place in a system. The ACF can also be derived from the time signals:

$$ACF(\tau) = \frac{\text{cov}(x(t), x(t+\tau))}{\text{var}(x(t))} \quad (6.5)$$

with the covariance given by:

$$\text{cov}(x(t), x(t+\tau)) = E[(x(t) - \mu)(x(t+\tau) - \mu)] \quad (6.6)$$

with E the expectation operator and μ the average of x . The auto-correlation function always lies between zero and one. The CCF can be derived in a similar manner.

The auto-correlation function can show the existence of 'memory' in the system. If the ACF is not equal to zero at some time delay τ it means that there is some physical mechanism present which causes a fluctuation of the variable to have an effect on the same variable a time τ later. This physical mechanism can of course be a complex combination of mechanisms and it may not be possible to separate these. Since white noise has no 'memory' (the value at each time instant does not in any way depend on the values at other times) the ACF of white noise is zero for every time shift τ except for $\tau=0$.

The decay-ratio (DR), which we will use to characterize the stability of the system, can be calculated from the auto-correlation function. For a second-order system the decay-ratio is defined as the ratio of two consecutive maxima of the auto-correlation function. In higher order systems one parameter cannot fully describe the stability of the system and the ratio between two consecutive maxima of the auto-correlation function will depend on exactly which maxima are chosen (Van der Hagen et al., 1994). In the derivation of the decay-ratio from DESIRE data we used the first two maxima and minima. For each pair of maxima (and minima) the ratio was taken and the decay-ratio was calculated as the average of these two ratios.

Another useful function is the coherence, which is given by:

$$coh(\omega) = \frac{|\overline{CPSD(\omega)}|^2}{|\overline{X(\omega)}|^2 |\overline{Y(\omega)}|^2} \quad (6.7)$$

where the CPSD and APSDs are averaged over a number of records. The coherence always lies between zero and one. It determines the extent to which the two random processes which generated x and y are linearly related (Priestley, 1981).

In principle the Fourier transform of a signal should consider the entire signal, from minus infinity to plus infinity. In practice we calculate the Fourier transform for each record, which is of finite length. This gives the same result as calculating the Fourier transform over the entire signal after multiplying it with a function that is equal to 1 inside the record and equal to zero outside the record (this is called a Boxcar window). This leads to a difference between the calculated and the theoretical Fourier transform. To alleviate this effect windowing methods are usually used. Besides the basic Boxcar window other well-known windows are the Hanning and Bartlett windows. In our calculations we use the Boxcar window. However, the effect of the windowing was found to be quite small because we used a relatively long record length (30-60 seconds) compared with the time constant of the dominant processes (1-2 seconds).

6.2 Measurements without feedback

Before we will study the effect of feedback on the dynamics of the natural circulation loop we will take a look at the dynamics of the loop without feedback. A measurement was performed where signals from various locations around the whole loop were recorded. The operating conditions are shown in table 6.1.

For the noise analysis technique to work the fluctuations in each signal must reflect a real fluctuation in the physical process. Random fluctuations, such as electronic noise, or as caused by the Poisson statistics of the gamma source are not useful. In principle the boiling of Freon is a stochastic process, and there will always be fluctuations in the void-fraction. But these

fluctuations are too small to be practical. Therefore we introduce fluctuations in the power of the assembly by driving the control lines to the power supply with a noise signal. These fluctuations in power will cause fluctuations in the void-fraction and in the other signals.

6.2.1 Results on various signals around the loop

Power	29 kW
Flow rate	1.1 kg/s
Subcooling	3.4 °C
K_{in}	-
Pressure	11.6 bar

Table 6.1 Operating conditions

In figure 6.1 the CCF between the power and the other signals is shown. The left column gives the CCF between power and various temperatures. At the bottom we start with the temperature at the assembly inlet. Since this is located upstream of the fuel assembly, the power cannot have a direct influence on this temperature. Only after the liquid has gone around the whole loop once can a power fluctuation influence the temperature. Thus there is a positive peak at a time delay of about 27 seconds. The main mechanism that is

responsible for this peak is the carry-under. A positive power fluctuation will cause an increase in the quality and flow rate (see the power-void CCF in the right column) which gives an increase of the carry-under (see chapter 4). In turn this carry-under will increase the temperature of the liquid below the feedwater sparger (this can be seen in the CCF of Td2, at $\tau=8$ s). The temperature fluctuation then travels through the downcomer loops until it reaches the assembly inlet.

The positive peak at $\tau=0$ is caused by interference of the power supplies with the thermocouple signals. This interference is proportional to the voltage applied by the power supplies to the fuel rods. If this interference is stronger than the temperature fluctuations this will result in a narrow positive peak at $t=0$. At the inlet of the fuel assembly the temperature fluctuations are very small because the liquid has had sufficient time to mix while flowing around the loop, so it has returned to thermal equilibrium.

The CCF for the first thermocouple inside the assembly, Tr2, has a large positive peak at a small delay of about 0.5 seconds. This thermocouple is located about 12 cm above the assembly inlet. In this region subcooled boiling takes place, and the power has a direct effect on the temperature. One important fact which we can conclude from this figure is that the time constant of the fuel rods cannot be much larger than 0.5 seconds, otherwise the delay from power to temperature would be larger. The positive peak at 27 seconds is the same as that peak in the CCF for Ti1.

A bit higher up the assembly, at 31 cm (Tr4), the flow is reaching thermodynamic equilibrium. The temperature is then simply the saturation temperature, and the power no longer will affect the temperature. The peak at 27 seconds has almost vanished. There is a large positive peak at a delay of 0.8 seconds, which could still partly be caused directly by the power fluctuations.

At the exit of the assembly the flow certainly has reached thermodynamic equilibrium. In that case the temperature only depends on the pressure. This is exactly what can be seen in the CCF for Tf1: it is exactly the same as the CCF for the pressure in the steam dome (P_v). The pressure in the steam dome is determined by the combination of void-fraction fluctuations and the characteristics of the pressure controller. There is a clear correlation between the power and the pressure. A positive power fluctuation gives an increase of the void-fraction. This increases the pressure with a delay of about 1 second. The pressure controller responds by opening and allowing the steam flow rate to increase. The dynamic characteristics of the pressure controller are probably responsible for the exact behaviour of the pressure, thus the pressure fluctuations are not really interesting from a physical point of view. Fortunately these pressure fluctuations are quite small and do not have much effect on the rest of the system.

The CCF between the power and the void-fraction is straightforward: a positive peak at about $\tau=1$ s. In these measurements the void-fraction was measured at the middle of the assembly. This delay is caused partly by heat transfer from fuel to coolant and partly by the transport of the flow from the bottom of the assembly to the measurement point.

Finally we look at the CCF between the power and the collapsed liquid level in the downcomer. The CCF first becomes positive. The increase of void-fraction in the assembly and riser forces liquid out of this region and raises the liquid level in the facility. When the void-fraction fluctuation has reached the exit of the riser the level drops again. However, an increase in carry-under caused by the higher void-fraction in the riser now decreases the collapsed level in the downcomer. The CCF crosses zero at a delay of about 3.5 seconds. At that point the void has left the riser and has entered the downcomer as carry-under. Not until a delay of 10 seconds does the CCF become zero again. Thus the carry-under persists for quite a long time in the downcomer.

It is also instructive to look at the coherence between the power and the various signals. Figure 6.2 gives the coherence for the same measurement as in figure 6.1. The effect of the interference between the power supplies and the signals can be seen in the temperature at the assembly inlet. The coherence becomes large for higher frequencies meaning that all the fluctuations in the thermocouple signal are caused by the power supplies at these frequencies. At low frequencies the coherence becomes very small. This means that there are other independent processes which cause temperature fluctuations at these low frequencies. One possibility for this are feedwater temperature fluctuations, which always have a low frequency. Another reason for the small coherence at low frequency is that the power fluctuations are smaller at these frequencies. As a reference the APSD of the power is shown at the top right in the figure.

The coherence for Tr2, the temperature at 11 cm height inside the assembly, is very different. For frequencies larger than 0.6 Hz it becomes very small. Higher along the assembly, at 31 cm, the coherence is larger. The coherence is also large for low frequencies, which means that the effects of the feedwater temperature are no longer seen.

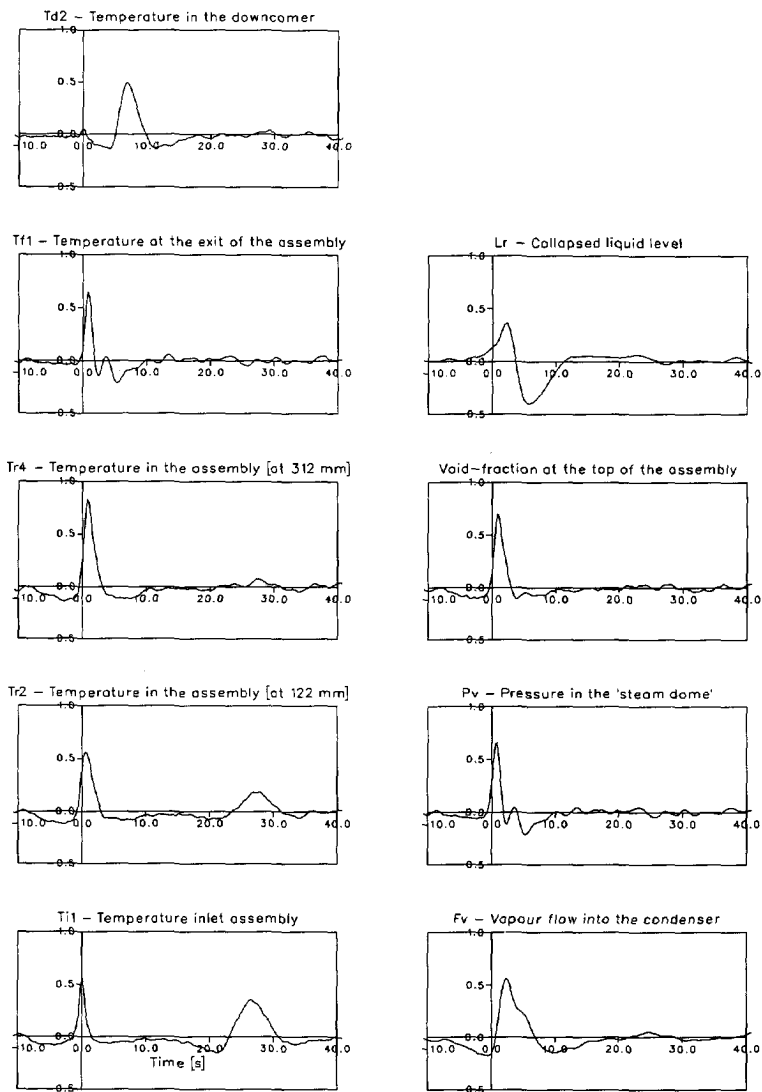


Figure 6.1 The cross-correlation function between the power and other signals. The power supplies were driven with a white noise signal.

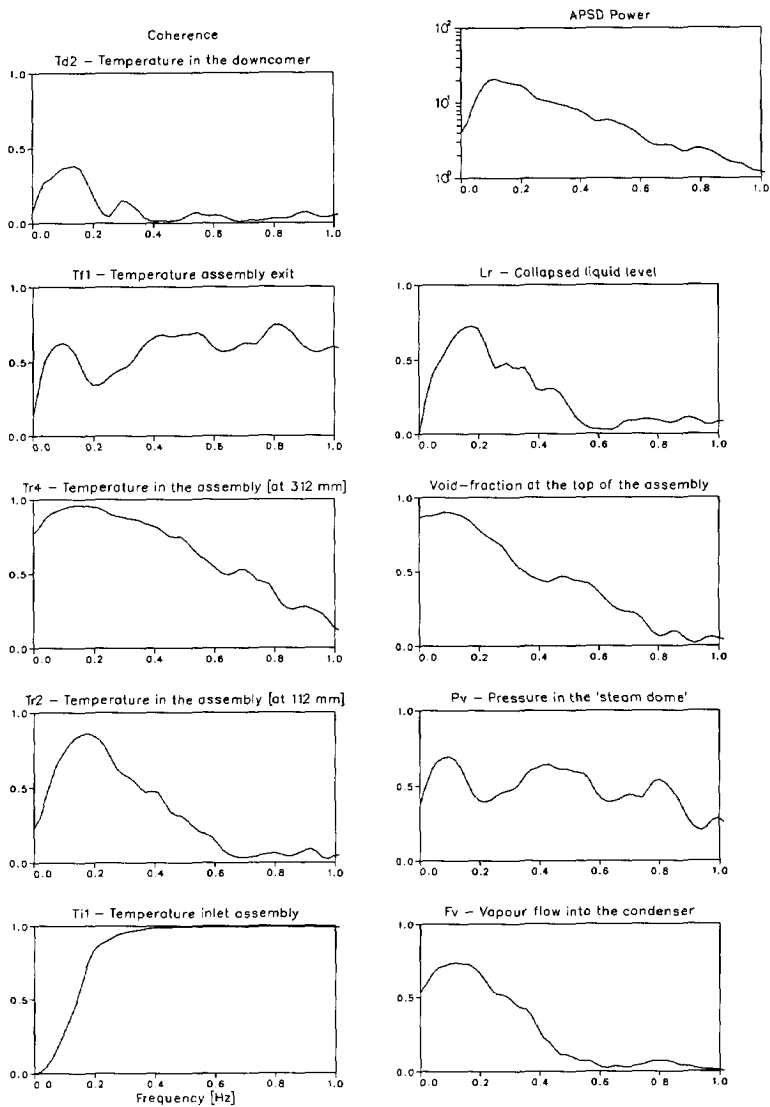


Figure 6.2 The coherence between the power and other signals.

In the downcomer the coherence of the temperature with the power is small. Only at low frequencies does the power still affect the temperature here. This can be understood when one considers that the temperature fluctuations here are caused only indirectly by the power fluctuations via the carry-under. Since the residence time of vapour in the downcomer above the feedwater sparger is quite large this will tend to filter out the higher frequencies.

6.2.2 Results for the natural circulation flow rate

We will now look somewhat closer at the dynamics of the natural circulation flow rate. For simplicity the inertia of the Freon in the loop will be neglected in the following discussion (this would give an additional phase shift between driving force and flow rate). To justify this simplification we need to consider the loop momentum balance (equation 4.1). The summation in the denominator in this equation is this approximately 2200 m^{-1} for DESIRE. The driving force can be estimated by considering the void-fraction and assembly plus riser height. This gives

$$\Delta p_{\text{driv}} = \langle \alpha \rangle H \Delta \rho g \quad (6.8)$$

with $\langle \alpha \rangle$ the average void-fraction over assembly+riser and H the length of the assembly+riser. Here the carry-under has been neglected. The frictional pressure drop is modeled as $\Delta p_{\text{loss}} = a \phi^2$. The parameter a follows from the requirement that $d\phi/dt=0$ at the operating point of $\phi_0=1.5 \text{ kg/s}$. Linearising the loop momentum balance

$$\begin{aligned} \phi(t) &= \phi_0 + \delta \phi \\ \langle \alpha \rangle(t) &= \langle \alpha \rangle_0 + \delta \langle \alpha \rangle(t) \\ a \phi_0^2 &= \langle \alpha \rangle_0 H \Delta \rho g \end{aligned} \quad (6.9)$$

and taking the Laplace transform gives us the following transfer function from void-fraction fluctuations to flow rate:

$$\frac{\delta \hat{\phi}}{\delta \hat{\alpha}} = \frac{\phi_0}{2 \langle \alpha \rangle_0} \frac{1}{1 + s \tau}; \quad \tau = \frac{\phi_0 \sum_i \frac{l_i}{A_i}}{2 \langle \alpha \rangle_0 H \Delta \rho g} \approx 0.1 \text{ s} \quad (6.10)$$

where $\hat{\phi}$ and $\hat{\alpha}$ are the Laplace transforms of ϕ and $\langle \alpha \rangle$ with s the Laplace variable. Typical values for $\langle \alpha \rangle_0$ and H are $\langle \alpha \rangle_0=0.5$ and $H=2.4 \text{ m}$. The time constant associated with this first-order response is 0.1 s . This is much shorter than the time constants of the processes which will be discussed in the following, so the flow can be considered to instantaneously adjust itself to changes in driving force and friction.

In figure 6.3 the results of two experiments are given. One measurement was performed at low power (15 kW) and one at high power (35 kW). Shown from top to bottom are CCF, the

CPSD, the phase and the coherence between void-fraction fluctuations and the flow rate fluctuations.

First we look at the CCF for positive τ . At $\tau=0$ the CCF is very small. This means that changes of the void-fraction in the assembly have little direct effect on the circulation. The reason for this is that both the driving force and the two-phase friction are increased by the larger void-fraction. The net effect is small. However, in the riser the friction is much smaller than in the fuel assembly. Thus after the vapour has traveled to the riser section the increase in driving force gives an increase in the natural circulation flow rate. This leads to the positive peak at $\tau \approx 0.8$ s.

The width of this positive peak in the CCF depends on the transit time of the void-fraction through the riser. The velocity of the two-phase flow through the riser was about 1.0 m/s at 15 kW and 1.6 m/s at 35 kW. With a riser length of 1.5 m this gives a transit time of 1.5 s at 15 kW and 0.94 s at 35 kW. The FWHM of the two peaks is 1.75 s at 15 kW and 1.16 s at 35 kW. The ratio between these two (1.5) is comparable to the ratio between the transit times (1.6).

Next we look at negative t . Here we see that the CCF exhibits a negative peak with a minimum at about -1 s. This means that an increase in the flow rate leads to a decrease in the void-fraction, which is exactly what can be expected.

Finally we look at the (negative) third peak, which occurs at $\tau \approx 3$. The origin of this peak is less straightforward to find than that of the other two so we will speculate. It could be the first indication of flow oscillations. The following scenario could be followed: a positive void-fraction fluctuation at $t=0$ gives a rise in the flow rate after about 0.8 seconds (positive peak at $t=0.8$ s). This in turn leads to a void-fraction decrease 1 second later (negative peak at $t=-1$ s) which will lead to a void-fraction decrease after a delay of again 0.8 seconds (positive peak at $t=0.8$ s). So a decrease takes place at a delay of $0.8+1+0.8=2.6$ seconds which corresponds to the delay of the negative third peak in the CCF. A second totally different explanation involves the carry-under. After the positive void-fraction fluctuation has traveled through the riser the carry-under will increase. This will lead to a higher void-fraction in the downcomer between the riser exit and the feedwater sparger thus decreasing the driving force. Of course one explanation does not exclude the other, and both mechanisms could contribute to this negative peak in the CCF.

At higher frequencies (>0.3 Hz) the CPSD for 35 kW is larger than the CPSD for 15 kW. This is caused by the higher velocity of the flow. In the coherence the largest difference between the two cases is at low frequencies (<0.3 Hz). This reflects the difference of the steady-state behaviour for the two cases. At 35 kW the low-frequency power fluctuations have less effect on the flow rate, because the slope of the power-flow curve (see figure 4.5) is smaller than at 15 kW.

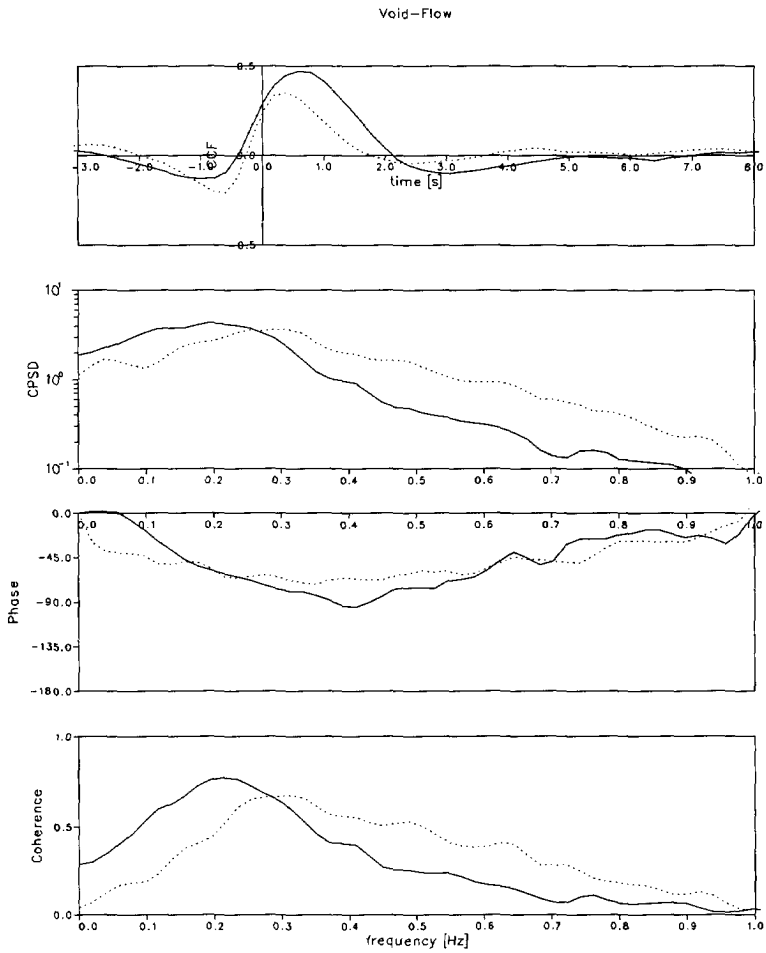


Figure 6.3 The CCF, CPSD, phase and coherence of void-fraction to flow rate for the measurements at 15 kW (solid line) and at 35 kW (dotted line).

6.2.3 Comparison of measurements with the model

In the previous sections a qualitative discussion of the dynamics of DESIRE was given. This allows us to get a feeling for the most important processes determining the dynamics. To get a better quantitative view of the dynamics the measurements are compared against the model. The model does not describe fluctuations of the coolant temperature, pressure or liquid level. The only two transfer functions which can be compared against the measurements are the power to void-fraction and the power to flow rate transfer functions. The measurement parameters are given in table 6.2.

Power	22 kW
Flow rate	1.8 kg/s
Subcooling	2.6
K_{in}	10
Pressure	11.6 bar

Table 6.2 Operating conditions

In figure 6.4 the gain and the phase of the measured and calculated transfer functions between the power and the void-fraction are plotted. The gain of the measured transfer function is normalized to coincide with the model at a frequency of 0 Hz.

The power-void transfer function is mainly determined by the fuel time constant and by the transport of the vapour along the assembly. We can use this to fit the model to the measured data using the fuel time constant as a parameter. Figure 6.4 shows that a fuel time constant of 0.5 seconds gives the best result, which agrees with calculations using the material properties and some assumptions on the boundary layer thickness and also with the observation made in section 6.2.1. With this fuel time constant the overall agreement of the measurements with the calculations is good, both for the gain and for the phase. The agreement of the phase is an indication that the quasi-static approximation used in the model is acceptable and that the void-fraction measured at the second viewing port is in-phase with the average void-fraction (which is used in the model). The transfer function between the power and the flow rate is shown in the bottom of figure 6.4. Considering all the approximations made in the model the agreement is excellent.

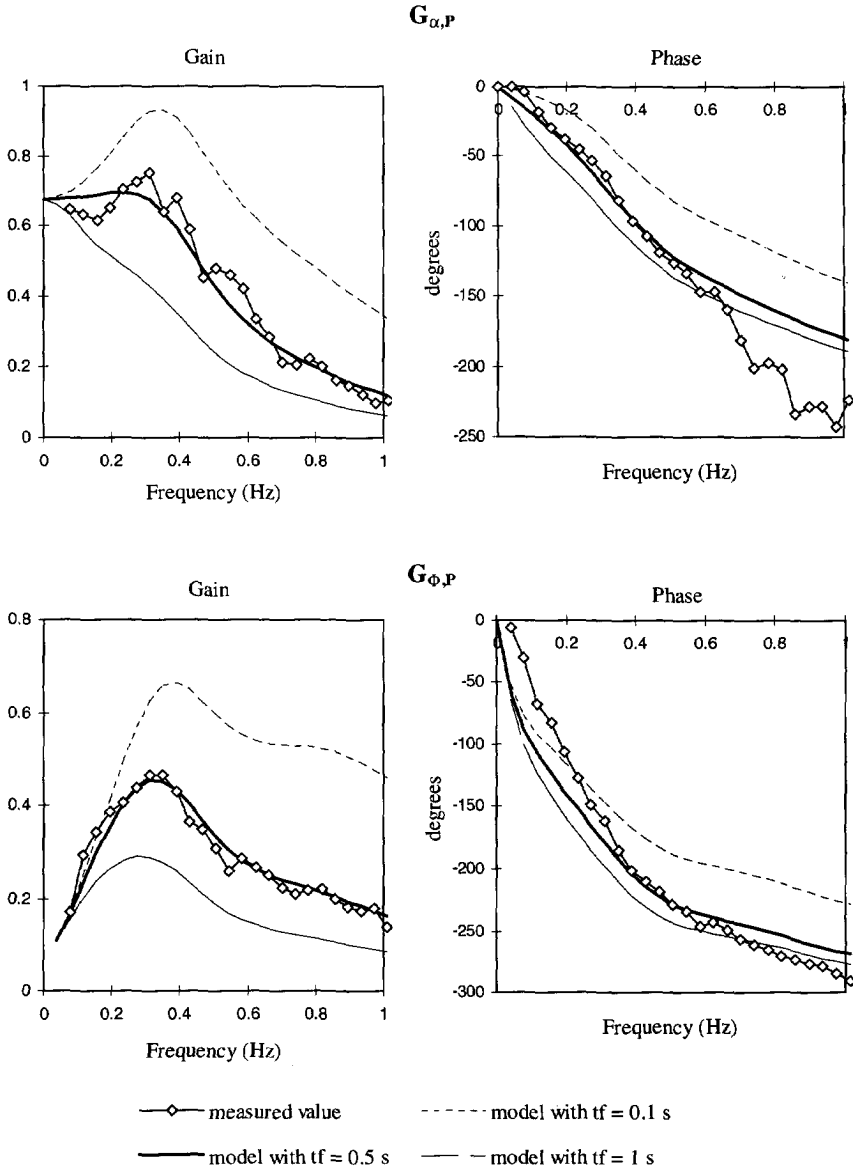


Figure 6.4 Gain and phase of the measured transfer function between power and void-fraction (top) and power and flow rate (bottom) compared with the model for several values of the fuel time constant: $\tau_f \approx 0.1, 0.5, 1$ s. From this comparison it is clear that the time constant of the DESIRE fuel rods is approximately 0.5 seconds.

These measurements were performed with the pressure controller turned off. When the pressure controller is used the transfer functions are affected, as can be seen in figure 6.5. A dip in the gain at 0.3 Hz appears. It is evident that the controlling action of the pressure controller can influence the dynamics of the loop, although at lower frequencies than at which the density wave oscillations will appear (see section 6.3.2). Unfortunately it is very cumbersome to perform measurements with the pressure controller turned off. Therefore the remaining measurements presented in this chapter were all performed with the pressure controller working. This means that any effects appearing around a frequency of 0.3 Hz are suspect.

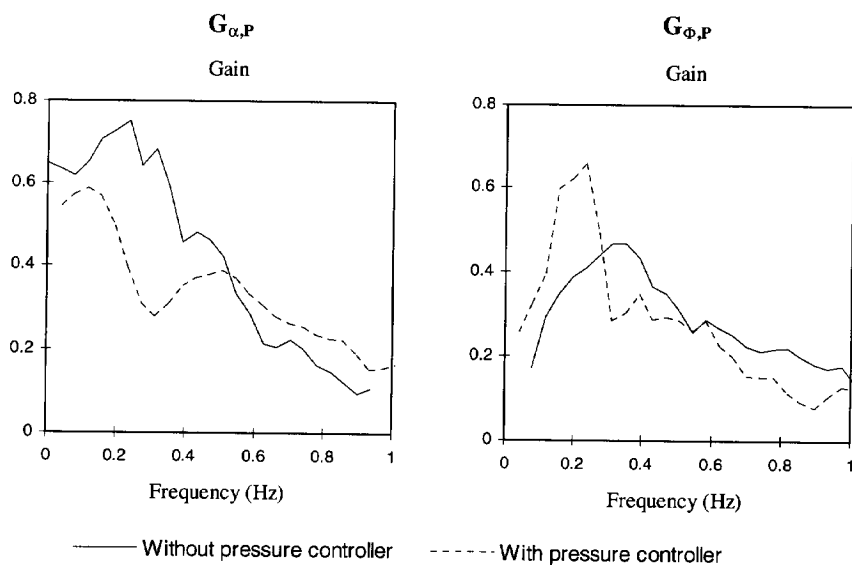


Figure 6.5 Effect of the pressure controller on the measured transfer functions from power to void-fraction and from power to flow.

6.3 *measurements with feedback*

6.3.1 *Turning on the feedback*

As soon as the simulated feedback is turned on a major change can be seen in the CCF and spectra between the power and the void-fraction. This can be seen in figure 6.6 where these have been plotted with the feedback off in the left column and with the feedback on in the right column. The operating conditions are given in table 6.3. Notice again the effect of the pressure controller at 0.3 Hz.

Power	22 kW
Flow rate	1.8 kg/s
Subcooling	2.6
K_{in}	10
Pressure	11.6 bar
r_{α}	-0.03
τ_f	0.5 s

Table 6.3 Operating conditions.

Without feedback there is a single peak in the CCF at a time delay of approximately 0.5 seconds (see also previous section). If the feedback is turned on the CCF equals -0.8 at $t=0$. This is due to the negative feedback, which reacts almost instantaneously to a void-fraction fluctuation (prompt-jump model of the reactor transfer function). So at a time delay of zero the CCF is dominated by the nuclear feedback mechanism. At time delays larger than zero the direct effect of the nuclear feedback is very small; only the delayed neutrons play a role here, and the thermal-hydraulic processes are dominant. The first positive

peak in the CCF has the same origin as the first peak in the case without feedback. This peak is of shorter duration because as soon as the void-fraction becomes larger than the equilibrium value the power decreases again and the void-fraction drops. After a few cycles the oscillations die out: the system is stable.

The CPSD also changes clearly when turning on the feedback. Low frequencies are attenuated and higher frequencies amplified. This is characteristic of negative feedback, as was also shown in chapter 5. The phase between power and void in the case of feedback is almost -180° for all frequencies, which again is a direct consequence of the negative feedback. The phase jumps from -180° to 180° have no physical meaning, they are the result of the representation of the phase in the range $\pm 180^\circ$.

The coherence also is directly affected by the feedback. Since the power is calculated purely from the void-fraction the coherence becomes 1.

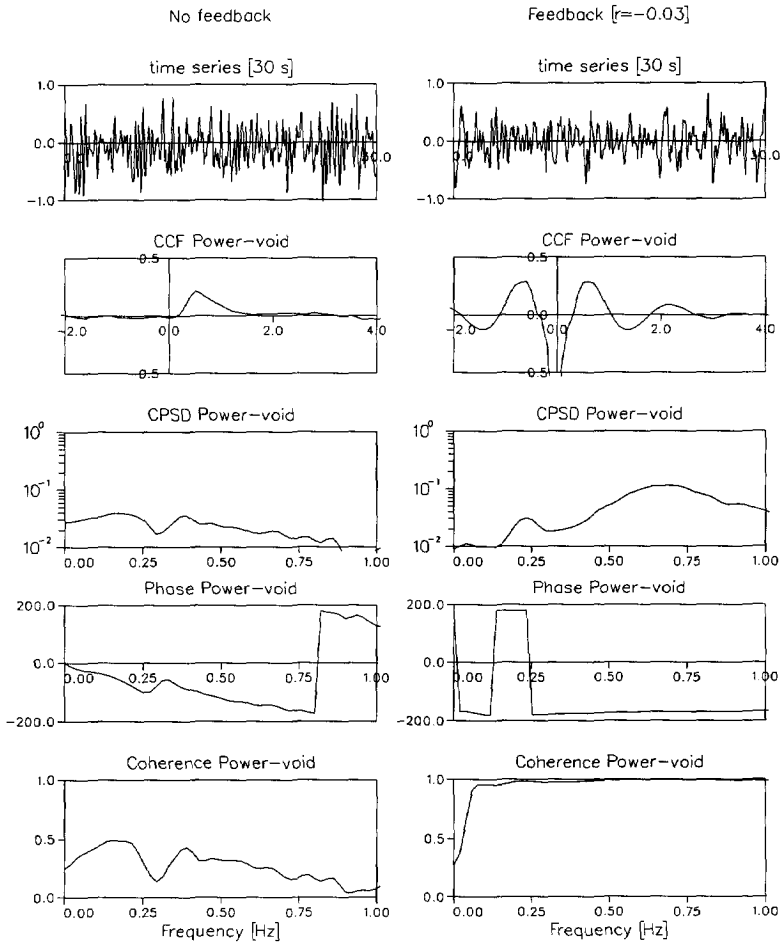


Figure 6.6 Comparison between noise measurements of the power to void-fraction transfer function taken without feedback in operation (left) and with the feedback in operation (right).

The natural circulation flow rate does not have such a strict dependence on the power as does the void-fraction when the feedback is turned on. Therefore the CCF and spectra between the power and flow rate signals are affected less by the feedback. These are shown in figure 6.7.

The CCF between the power and flow rate changes when the feedback is turned on. The change is comparable to the change in the CCF between the power and void-fraction except that the strong negative peak at $t=0$ is not present because there is not such a direct relationship between the two signals. The other changes to the CCF are comparable: the first positive peak lasts shorter and the CCF turns negative. A damped oscillation can be seen.

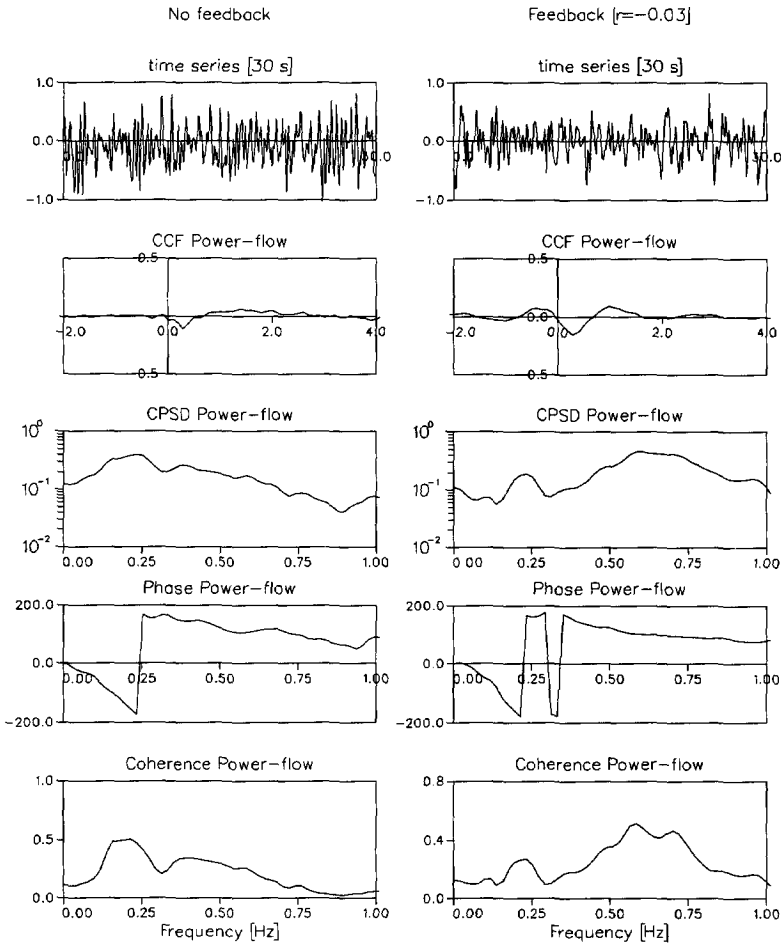


Figure 6.7 Comparison between noise measurements of the power to- flow rate transfer function taken without feedback in operation (left) and with the feedback in operation (right).

The CPSD between power and flow rate behaves much the same as the CPSD between the power and the void-fraction. The phase however is different in that it is not equal to -180 when the feedback is turned on. The same can be seen in the coherence: it is not equal to 1 with the feedback. Both the CPSD and the coherence become smaller at low frequencies and higher at high frequencies.

6.3.2 Effect of the feedback coefficient

When the feedback coefficient is increased several interesting things happen. Figure 6.8 shows a series of 6 measurements where the feedback coefficient was increased from 0 to -0.06. As the feedback coefficient is increased the oscillations become less damped. The oscillations can also be seen in time signal of the power. The operating conditions are the same as in the previous measurements.

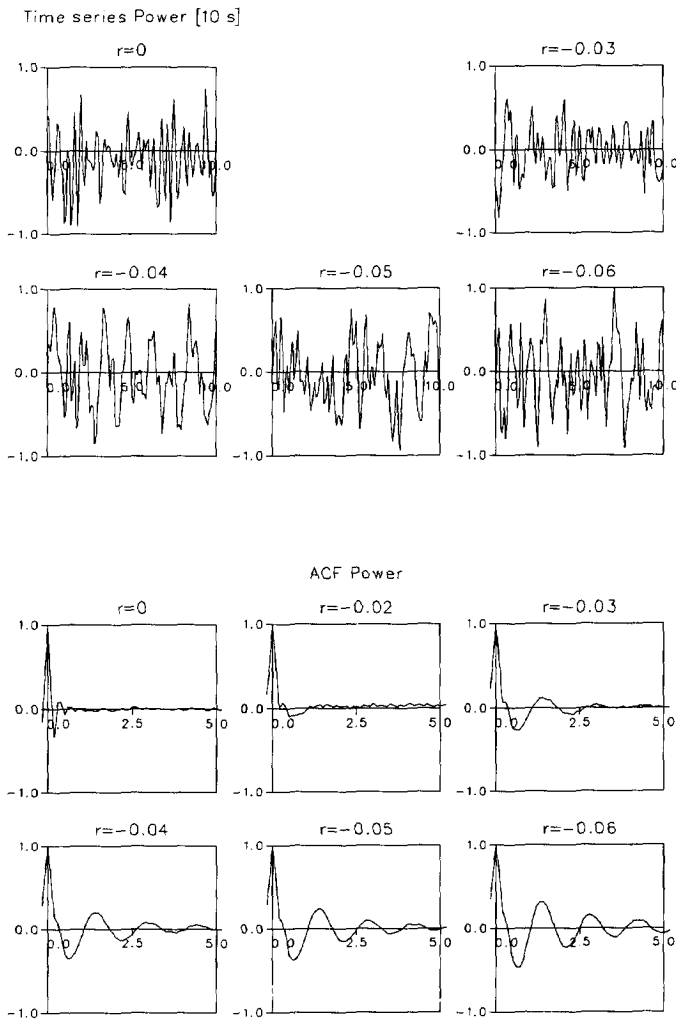


Figure 6.8 Time trace and auto-correlation function of the power with increasing values of the void-reactivity coefficient.

The increasing oscillations are also visible in the APSD of the void-fraction signal (figure 6.9). As the feedback coefficient is increased a peak becomes visible in the APSD at 0.7 Hz. (the peak at 0.25 Hz is probably caused by the pressure controller). This peak becomes higher as the feedback coefficient is increased. This can be compared with the root-loci diagrams in figure 5.5. In this diagram the second pole becomes less stable as r_a goes from -0.02 to -0.06. The frequency of the second pole increases slightly as the feedback coefficient is increased, which also happens with the second peak in the APSD. The frequency of the second pole (0.8 Hz) agrees with the position of the second peak (0.75 Hz).

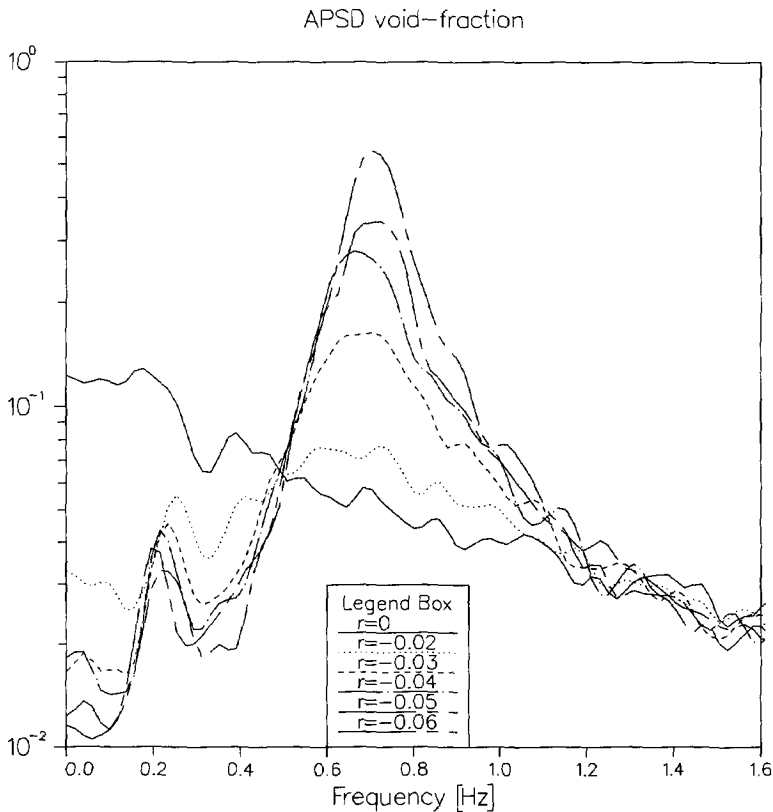


Figure 6.9 Spectrum of the void-fraction for increasing values of the void-reactivity coefficient (R_a).

6.3.3 Effect of the fuel time constant

In figure 6.10 the combined effect of the void-reactivity coefficient and the fuel time constant is shown. The void-reactivity coefficient increases from top to bottom and the fuel time constant increases from left to right. In general increasing the void-reactivity coefficient decreases the stability and increasing the fuel time constant increases the stability. The frequency of the oscillations hardly changes for higher fuel time constants. This can be compared with the movement of the poles as a function of the fuel time constant in figure 5.5. For $\tau_f > 0.5$ the second (dominant) pole moves almost perpendicular to the frequency axis.

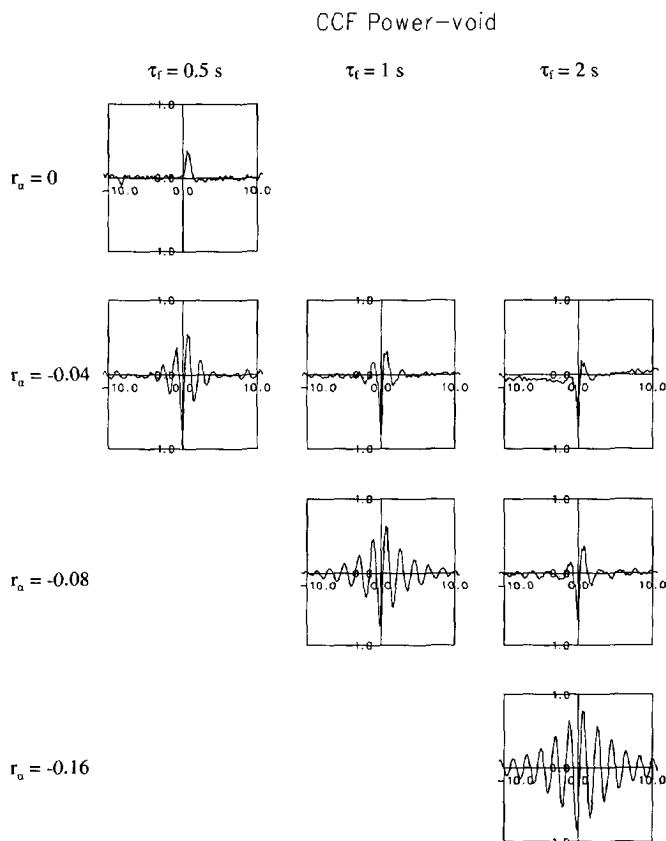


Figure 6.10 Effect of void-reactivity coefficient and fuel time constant on the power to void-fraction cross-correlation function.

6.3.4 *Measurement in the N_{Zu} - N_{sub} plane*

A direct comparison of measurements with the predicted stability map in the Zuber-subcooling plane is difficult because only a very limited region of this space can be reached with DESIRE. There are several reasons for this. First the average power must lie between 10-30 kW. This range is smaller than the range possible with static measurements to allow room for the power to oscillate. Secondly, the subcooling number is not an independent parameter. DESIRE has only three independent parameters: the power, the feedwater temperature and the control valve setting (see chapter 4). In the Zuber-subcooling plane this means that the subcooling depends on the Zuber number. In general the subcooling increases with the Zuber number. Variation of the feedwater temperature and the use of the heat-exchangers in the downcomer loops are used to control the subcooling. Changing the friction valve setting and thus the flow rate has a larger effect on the subcooling. However, this has a profound effect on the stability map, so measurements with varying friction valve settings cannot be compared within one single stability map.

Although the feedback coefficient can in principle be chosen to any value in practice its range is also limited. There is an upper limit above which the power fluctuations become too large for the power supplies to handle or above which the prompt-jump model is no longer valid. There is also a lower limit on the feedback coefficient which stems from the fact that it is not practical to determine the decay-ratio if it is too small, because then the second peak in the CCF vanishes in the noise. Thus for measurements of the DR to be possible it must lie between, say, 0.2 and 0.8.

Table 6.4 shows a set of ten measurements and compares the measured with the predicted values. In all measurements the void-reactivity coefficient was -0.05 and the fuel time constant was 0.5 s. There are rather large discrepancies between the predictions of the model and the measurements. In general the model strongly underpredicts the decay-ratio and overpredicts the frequency. In the table an error band is indicated for N_{sub} resulting from the uncertainty in the measured subcooling of 0.5 °C. This uncertainty is also taken into account in the calculated values of the decay-ratio and the frequency according to the model.

Four measurements were done at the nominal pressure of 11.6 bar. Both an increase of the power and of the subcooling have a destabilizing effect. The model in contrast predicts that the system should be more stable at higher power. The reason for this can be seen on the left of figure 6.11: the measurement points at 11.6 bar lie to the left of the maximum in the line where $DR = 0.2$.

At a pressure of 9 bar the measurements lie to the right of the maximum in the $DR = 0.2$ line. So the model predicts that increasing the power and subcooling is destabilizing. But the measurements seem to be insensitive to the operating conditions. There is only a slight increase of the decay-ratio for increasing subcooling, and a decrease of the decay-ratio for increasing power. At 6 bar the measured decay-ratio is the same for both measurement points.

The results are summarized in figure 6.11; in the middle the measured and calculated decay-ratios are compared and on the right the frequencies. The comparison of the decay-ratios shows a large scattering: the agreement is poor. The comparison of the frequencies is better: there is a clear correlation between measured and calculated frequencies, although the measured frequencies are less sensitive to the operating conditions than the calculated frequencies.

It seems there are too many approximations in the analytical model and in the simulated feedback to make a quantitative comparison successful. Another explanation for the discrepancies could be the effect of the pressure controller. Although the measured transfer functions with and without pressure controller operating are approximately the same at the oscillation frequency of 0.6-0.7 Hz they are very different at the lower frequency of 0.2-0.3 Hz (see figure 6.5). In a linear system this would not matter. However, DESIRE is not a linear system, so it is possible that the pressure controller affects the dynamics indirectly at higher frequencies.

Pressure	Operating conditions		Measured values		Calculated values	
	N _{Zu}	N _{sub}	DR	frequency (Hz)	DR	frequency (Hz)
11.6 bar	1.71	0.42 ± 0.07	0.35	0.65	0.127 ± 0.024	0.841 ± 0.015
	1.81	0.74 ± 0.07	0.47	0.57	0.242 ± 0.024	0.774 ± 0.011
	2.25	0.52 ± 0.07	0.47	0.64	0.107 ± 0.031	0.852 ± 0.018
	2.30	0.82 ± 0.07	0.63	0.62	0.214 ± 0.023	0.845 ± 0.004
9 bar	2.18	0.56 ± 0.10	0.71	0.63	0.117 ± 0.038	0.850 ± 0.008
	2.26	0.83 ± 0.10	0.73	0.60	0.219 ± 0.031	0.823 ± 0.007
	2.92	0.60 ± 0.10	0.65	0.66	0.203 ± 0.028	0.889 ± 0.001
	2.93	0.93 ± 0.10	0.65	0.63	0.288 ± 0.021	0.874 ± 0.006
6 bar	2.99	0.65 ± 0.14	0.74	0.63	0.212 ± 0.040	0.887 ± 0.001
	4.07	0.80 ± 0.14	0.74	0.66	0.379 ± 0.055	0.992 ± 0.011

Table 6.4 Measured and calculated frequency and decay-ratio. The uncertainty in N_{sub} results from the uncertainty in T_{sub} of ± 0.5 °C.

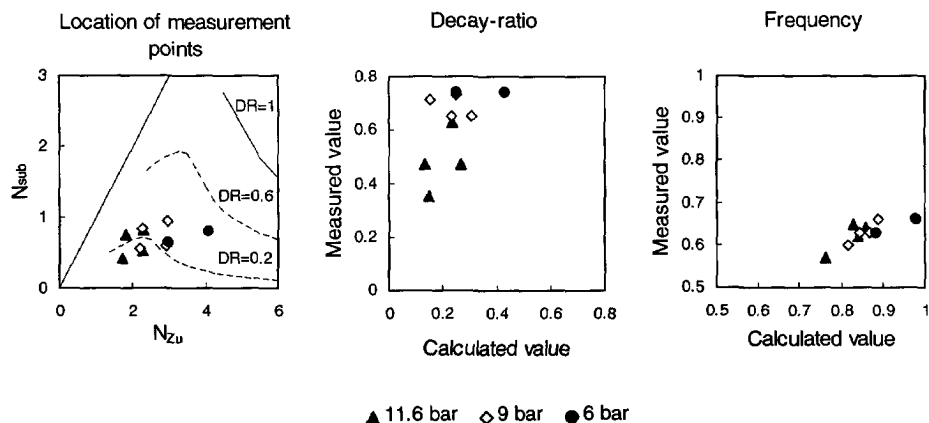


Figure 6.11 Location of the measurement points in the Zuber-subcooling plane on the left and scatter plots of the decay-ratio and frequency in the middle and on the right.

6.4 Discussion and recommendations for improvement

One recommendation for improving the feedback was already given in chapter 5. This concerned the measurement of the average void-fraction in the assembly using the capacitive measurement technique. A second recommendation concerns the measurement of the subcooling. In DESIRE this is done by comparing the temperature measured by a thermocouple at the inlet to the temperature measured by a thermocouple at the outlet of the assembly. This last temperature gives the saturation temperature, but at a pressure different from the inlet pressure. The difference in saturation temperature from the inlet to the outlet due to the pressure drop in the assembly is typically 0.2-0.3 °C which seems small but is still 10-15% of the subcooling at nominal conditions.

A problem arises when comparing the measurements to the model, which is very sensitive to the subcooling. The model assumes a constant saturation temperature over the whole loop, but at which location in the assembly does the subcooling coincide with the subcooling used in the model? The answer is that this location does not exist since the saturation temperature has an effect over the whole loop (consider flashing phenomena for example). The best location is that point where the effect of the saturation temperature is the largest. In the dynamic model this is probably the boiling boundary, which depends on the saturation temperature.

So for comparison with the model the saturation temperature at the boiling boundary should be used. For comparison with Dodewaard data the saturation temperature at the inlet should be used. At the moment we only have available the temperature at the inlet and the exit of the assembly. To get a better measurement of the subcooling we propose the following:

- Install accurate temperature sensors at the inlet and the outlet. Thermocouples have an error of up to 0.5 °C. This is much too high relative to the absolute value of the subcooling.
- Install a differential pressure sensors over the assembly. The pressure drop can directly be translated to a change in saturation temperature. The pressure at the boiling boundary can be assumed to be the same as at the bottom or it can quite easily be calculated from the flow rate (one-phase pressure drops only).

The differential pressure sensors over the assembly would also be useful for validating the friction factors used in the model.

Finally it is advised to install a different pressure controlling valve with a much slower response. It is probably possible to use a motor actuated valve with a PID controller or even a digital controller implemented in a PC to actuate the motor. This will allow the experimenter to choose the characteristics of the controller in such a way that it will not interfere with the measurements. The present mechanical pressure controller can be mounted parallel to this valve with the setpoint set to a higher pressure (so it is normally closed) to act as a kind of safety relief valve in case the electronics fails or the PC crashes.

6.4.1 Comparison with Dodewaard data

The ultimate goal of measurements on a scaled facility is to be able to make statements about the life-sized plant. This can be the reference plant, in this case the Dodewaard reactor, or a new plant design. Although the Dodewaard reactor is now shutdown there is a wide range of measurement data available with which measurements of the DESIRE facility could be compared. The difficulty with making a direct comparison is that despite the scaling analysis there are still large differences between DESIRE and Dodewaard. Two decisions made during the design of DESIRE are not favorable for studying the dynamics of the Dodewaard reactor:

- The downcomer loops were designed to get the same (scaled) loop residence time as in Dodewaard. A second consideration was the friction of the downcomer. However, for the dynamics the inertia of the liquid in the loop is of greater importance (although not very important, see section 6.2.2). This was not considered; the scaled inertia of the DESIRE downcomer is 3 times the inertia of the Dodewaard downcomer. The remedy is to change the design of the downcomer loops in DESIRE, making them shorter and using larger diameter tubing.
- Various components, such as the secondary cooling system and the heat exchangers in the downcomers were designed to reproduce the nominal Dodewaard operating conditions. However, at nominal operating conditions Dodewaard is very stable. The interesting measurements in Dodewaard were all performed during start-up and shut-down, at reduced pressure or with a higher subcooling. These conditions cannot be reached by DESIRE.

To make a direct comparison with Dodewaard data possible both the Zuber number and the subcooling number need to be increased. The power cannot be increased without major investments, changing both the fuel rods and the power supplies. The Zuber number can be increased by a factor of 1.5 by decreasing the pressure. The problem is that this will decrease the subcooling because the temperature difference between the feedwater (which is limited to $-15\text{ }^{\circ}\text{C}$) and the temperature in the loop (saturation temperature) decreases when the pressure is decreased.

Another difference between DESIRE and Dodewaard is the carry-under. The entrainment ratio in Dodewaard varies between 13 and 21 % depending on the pressure and the water level. In DESIRE the carry-under also depends on the operating conditions, but it cannot be controlled. So in general the carry-under in DESIRE and Dodewaard will be different. This can directly influence the dynamics of the loop, but the most important consequence is that the subcooling will be different. This is one of the reasons that the heat exchangers in the downcomer loops were installed. These give us control over the subcooling. However, the capacity of these heat exchangers is limited. Another recommendation is therefore to increase the capacity of the heat exchangers in the downcomer.

Instead of comparing the data directly with Dodewaard measurements we can use it to validate the model of the dynamics, which then can be applied to the Dodewaard reactor or to new reactor designs such as the SBWR. This route places much less stringent limitations on the operating range where measurements can be done, assuming that the model is equally valid for all operating conditions.

6.5 Conclusions

For the determination of transfer functions and the stability of the system from the measurements noise analysis techniques are ideal. In this work the (cross-)correlation function, the (cross-)power spectral density function and the coherence are used.

First a number of measurements were done without the void-reactivity feedback turned on. In that case the power supplies were driven with a white noise signal. The transit times through the loop can be seen in the CCF between the power and the thermocouples located around the loop. Various processes, such as the pressure controller dynamics and the effect of carry-under are visible. The response of the flow rate to the power fluctuations shows the different effects of the void-fraction in the assembly, in the riser and in the downcomer (as carry-under).

The measured transfer functions between the power and the void-fraction and between the power and the flow rate are compared to the same transfer functions in the dynamic model. From this comparison it can be concluded that the time constant of the DESIRE fuel rods is approximately 0.5 seconds, which agrees with the estimates obtained using a model of the heat transfer from fuel rod to coolant (chapter 5). The agreement between measurements and the model is good. This comparison was made with the pressure controller turned off. Comparison

of the transfer functions with the pressure controller turned on or off shows that the pressure controller affects the dynamics at frequencies around 0.3 Hz.

When the feedback is turned on the CCF and spectra between power and void-fraction change dramatically. The phase difference becomes -180° and the coherence becomes one. This is a direct result of the negative feedback. The transfer function between power and flow rate also changes. In general lower frequency components are suppressed and higher frequency components are amplified. As the feedback coefficient is increased the oscillations become larger and the stability decreases. In the APSD of the void-fraction (and the power) a peak appears at 0.75 Hz. This peak coincides with the second pole of the transfer function predicted by the model. It also has the same qualitative behaviour: the frequency increases slightly as the feedback coefficient is increased.

Comparison of the measurements with the model in the Zuber-subcooling plane were not very successful. There are a number of reasons for this. There are many approximations in the analytical model as well as in feedback simulation. The void-fraction measurement technique is not ideal. Also it appears that the pressure controller can affect the dynamics, which is not accounted for in the model. Finally a problem in making a comparison between model and experiment is that the DESIRE operating range is very limited. Some recommendations are given for improvement in all these areas.

Chapter 7

General conclusions and discussion

7.1 *Conclusions from this work*

Natural circulation boiling water reactors are an attractive candidate for the next generation of nuclear reactors. Even more than is the case with forced circulation boiling water reactors it is vital that all aspects of the thermal-hydraulic and the coupled neutronic- thermal-hydraulic behaviour are understood, because the coolant circulation flow rate, and therefore the cooling of the core, depends on these processes. In this work several aspects of the natural circulation boiling water reactor are studied using a scaled natural circulation loop called DESIRE. DESIRE comprises of one scaled copy of a Dodewaard fuel assembly together with a riser and a downcomer. It uses Freon-12 as a scaling liquid.

The driving force for the natural circulation originates in the boiling of the coolant in the reactor. The void-fraction is the all-important parameter which links the boiling of the coolant (and the extraction of heat from the core) to the natural circulation flow rate. In all boiling water reactors the void-fraction is important for the cooling of the fuel and the moderation of the neutrons. A measurement technique was developed for the measurement of the void-fraction on a subchannel basis (chapter 3). The technique is based on γ -attenuation and uses a tomographic reconstruction procedure to calculate the void-fraction in the subchannels from the measured chordal void-fractions.

The measurements are compared with two-phase flow models. General conclusions from this comparison are that the drift-flux model using Dix's correlation in combination with a subcooled boiling model gives a good description of the development of the average void-fraction as a function of height. From comparison of the development of the void-fraction in individual subchannels it was concluded that lateral void-drift, i.e. transport of vapour across

the subchannels, is negligible. Void-fraction measurements were also carried out in the riser and downcomer. Two-phase flow models were fitted to these measurements.

The results from the void-fraction measurements are used in the development of a static flow model. This flow model is described in chapter 4. The important processes that determine the natural circulation flow rate were identified and modeled. These include subcooled boiling and carry-under. A correlation for carry-under was derived on the basis of measurements.

The static flow model is in excellent agreement with measurements of the natural circulation flow rate over a wide range of operating conditions (at nominal pressure). This suggests that all the relevant physics are contained in the model. The most important conclusion we can make from the success of the model is that distribution of the friction factors between the one-phase region and the two-phase region is modeled correctly. This is of vital importance for the dynamics of the natural circulation flow. However, a more detailed breakdown of the distribution of the pressure drops could not be made. For this it is necessary to install differential pressure sensors at several locations.

In chapter 5 a model of the dynamics of a natural circulation boiling water reactor developed by Van Bragt is described. The model was adapted to DESIRE by changing the appropriate dimensions and parameters in the model. For the friction factors the values that were found in chapter 4 are used.

To be able to investigate nuclear-coupled thermal-hydraulic instabilities DESIRE was fitted with a simulated void-reactivity feedback. The void-fraction is measured using the γ -attenuation technique. This is a local measurement technique. In contrast, the model uses the average void-fraction in the neutronic feedback. To match the simulation with the model the simulation calculates the average void-fraction from the local void-fraction and the subcooling.

Noise analysis techniques were used to determine the transfer functions and the stability of the system. In this work the (cross-)correlation function, the (cross-)power spectral density function and the coherence are used. Measurements of the transfer function without the simulated feedback in operation give valuable information on several processes of the system. Some of these processes, such as the pressure and feedwater controller dynamics are not interesting from a physical point of view. These may interfere with the dynamics when the stability is investigated in the presence of void-reactivity feedback.

The measured transfer functions between power and void-fraction and between power and flow rate are compared to the same transfer functions in the dynamic model. The overall agreement between measurements and the model is good providing the pressure controller is not used.

When the feedback is turned on the correlation functions and spectra between power and flow rate change. In general lower frequency components are suppressed and higher frequency components are amplified. As the feedback coefficient is increased oscillations become larger

and the stability decreases. In the auto power spectral density function of the void-fraction (and the power) a peak appears at 0.75 Hz. This peak coincides with one of the poles of the transfer function predicted by the model. It also has the same qualitative behaviour: the frequency increases slightly as the feedback coefficient is increased.

Comparison of the measurements with the model in the Zuber-subcooling plane were not very successful. There are a number of reasons for this. There are many approximations in the analytical model as well as in feedback simulation. The void-fraction measurement technique is not ideal. Also it appears that the pressure controller can affect the dynamics, which is not accounted for in the model. Finally a problem in making a comparison between model and experiment is that the DESIRE operating range is very limited.

7.2 *Recommendations*

As demonstrated in chapter 6, the concept of the simulated void-reactivity feedback is successful. Comparison of some individual transfer functions with the model also show good agreement. However, a quantitative comparison between the measurements and the model fails. Both the model and the void-reactivity simulation contain too many approximations. The void-fraction measuring technique presently used for the simulation has two severe drawbacks: it is a local measurement and it is noisy. As discussed in chapter 6 it is necessary to adopt a different void-fraction measuring technique. For this the capacitive measurement technique is recommended, as it is noise free and can easily be adopted to measure the (weighted) average void-fraction.

It is also advised to install a different pressure controlling valve with a much slower response. It is probably possible to use a motor actuated valve with a PID controller or even a digital controller implemented in a PC to actuate the motor. This will allow the experimenter to choose the characteristics of the controller in such a way that it will not interfere with the measurements.

To increase the operating range of DESIRE the capacity of the heat exchangers in the downcomers should be increased. This will make both the comparison of the experimental data with the model and with available data from the Dodewaard reactor easier.

One last recommendation concerns the measurement of the subcooling. This was discussed in chapter 6. It is recommended that accurate temperature sensors are installed at the inlet and the outlet of the assembly and that a differential pressure sensor is installed over the assembly. This can be used to calculate the saturation temperature at the inlet.

7.3 *Concluding remarks*

A great deal of experience has been gained during this project. This experience can be used for improving DESIRE or in designing new facilities. Especially the adoption of simulated neutronics in a thermal-hydraulic facility is very promising for the future. To be able to get a good quantitative agreement between plant, facility and model great care should be given to the design of the facility and the implementation of the void-reactivity feedback. This work has recognized several key aspects that must be done correctly to get good results. It is my desire that future researchers can benefit from this knowledge.

Nomenclature

A	-	area	m^2
c	-	delayed neutron population	-
C_0	-	distribution parameter	-
c_l	-	heat capacity of liquid	$\text{kJ kg}^{-1} \text{K}^{-1}$
d	-	distance	m
D_h	-	hydraulic diameter	m
Δp	-	differential pressure	Pa
f	-	friction factor	-
g	-	gravitational acceleration	m s^{-2}
G	-	transfer function	-
h_l^{sat}	-	saturation enthalpy	kJ kg^{-1}
h	-	enthalpy	kJ kg^{-1}
H	-	length of fuel rod	m
I	-	count rate	s^{-1}
j	-	volumetric flux	m s^{-1}
K	-	friction factor	-
l	-	length	m
L_r	-	riser length	m
\dot{m}''	-	mass flux	$\text{kg s}^{-1} \text{m}^{-2}$
n	-	neutron population	-
P	-	Power	W
\dot{q}''	-	wall heat flux	W m^{-2}
r	-	heat of evaporation	kJ kg^{-1}
r_a	-	void-reactivity coefficient	-
T	-	temperature	K
t	-	time	s
v	-	velocity	m s^{-1}
V	-	volume	m^3
v_{gj}	-	drift velocity	m s^{-1}
x	-	flow quality	-
x_{eq}	-	equilibrium quality	-
$x_{eq,d}$	-	equilibrium quality at the departure point	-
z	-	axial position	m
z_{bb}	-	boiling boundary	m

Greek

α	-	void-fraction	-
α^*	-	chordal void-fraction	-
β	-	delayed neutron fraction	-

$\Delta\rho$	-	density difference between vapour and liquid	kg m^{-3}
Φ	-	flow rate	kg s^{-1}
ϕ	-	two-phase multiplier	-
ϕ_R	-	Romie multiplier	-
λ	-	delayed neutron time constant	s^{-1}
Λ	-	neutron generation time	s
λ_1	-	thermal conductivity	$\text{W m}^{-1} \text{K}^{-1}$
μ	-	gamma attenuation coefficient	cm^{-1}
ρ	-	density	kg m^{-3}
ρ	-	reactivity	-
ρ_α	-	void reactivity	-
σ	-	surface tension	N m^{-1}
τ	-	time delay	s
τ_f	-	fuel time constant	s
ω	-	angular frequency	rad s^{-1}
Ψ	-	entrainment ratio	-

Subscripts

1 ϕ	-	one-phase
2 ϕ	-	two-phase
acc	-	acceleration
as	-	assembly
cu	-	carry-under
d	-	downcomer
driv	-	driving force
e	-	assembly exit
eq	-	equilibrium
ext	-	external
f	-	feedwater
f,d	-	DESIRE fuel
f,p	-	plant fuel
g	-	gas, vapour
i	-	beam number
inl	-	assembly inlet
j	-	node number
l	-	liquid
loss	-	pressure loss
m	-	structural material
ncir	-	natural circulation
r	-	riser
sat	-	saturation
sub	-	subcooling
valve	-	friction valve
z	-	axial location

Dimensionless numbers

N_d	-	drift-flux number
N_{Fr}	-	Froude number
N_g	-	geometry number
N_ρ	-	density ratio
N_{pch}	-	phase change number
N_{Pe}	-	Péclet number
N_{sub}	-	subcooling number
N_{we}	-	Weber number
N_{Zu}	-	Zuber number
N_{Re}	-	Reynolds number
N_{St}	-	Stanton number

Abbreviations

ACF	-	auto correlation function
APSD	-	auto power spectral density function
ARMA	-	auto regressive moving average
BWR	-	boiling water reactor
CCF	-	cross correlation function
coh	-	coherence
CPSD	-	cross power spectral density function
DESIRE	-	delft simulated reactor
DR	-	decay ratio
FWHM	-	full width at half maximum
SBWR	-	simplified boiling water reactor
SIDAS	-	simulated delft assembly
ESBWR	-	European simplified boiling water reactor
var	-	variance

References

- Achard, A., Drew, D.A., Lahey, R.T. (1985) "The analysis of nonlinear density-wave oscillations in boiling channels," *J. Fluid. Mech.*, vol. 155, p. 213-232.
- Adams, B.T. (1997) "A scaling law verification of the Delft Simulated Reactor (DESIRE)," *Proc. of 20th nuclear simulation symposium*, September 7-9, 1997, Niagara-on-the-Lake, Ontario, Canada, Canadian Nuclear Society.
- Aritomi, A., Nakahashi, T., Chiang, J.H. (1990) "Transient behaviour of natural circulation for boiling two-phase flow", *1990 ANS winter meeting*, November 15, 1990.
- Arnold, H., Yadigaroglu, G., Stoop, P.M., Gonzalez, A., Rao, A. (1996) "From Dodewaard to a modern economic passive plant ESBWR", *Topnux '96 Int. Conf.*, September 30-October 2 1996, Paris.
- Bankoff, S.G. (1960), *J. of Heat Transfer*, 82, p. 265-272.
- Beckjord, E.S. (1960) "Dresden stability tests", *GEAP-3550*.
- Beckjord, E. (1995) "Turning points in reactor design," *Proc. of NURETH-7*, 10-15 September 1995, Saratoga Springs, New York.
- Billa, C., Bovalini, R., D'Auria, F., Mazzini, M. (1994) "Evaluation of a thermalhydraulic instability experiment performed in Piper-One apparatus," *Int. Conf. On New Trends in Nuclear Systems Thermohydraulics*, May 30- June 2 1994, Pisa, Italy, Vol. I, p. 373-380.
- Bouré, J.A. et al. (1973) "Review of two-phase flow instability," *Nucl. Eng. Des.*, 25, p. 165-192.
- Bovalini, R., D'Auria, F., Mazzini, M., Vigni, P. (1996) "Status and perspectives of Piper-OneE facility," *Proc. ENS Topical Meeting - Research facilities for the future of nuclear energy*, 4-6 June, Brussels, Belgium, 1996.
- Bueno de Mesquita, K.G. et al. (1991) "Results of a comparison study of advanced reactors," PINK report, NUCON, The Netherlands.
- Chexal, B., Lellouche, G., Horowitz, J., Healzer, J. (1992) "A void fraction correlation for generalized applications," *Progress in Nuclear Energy*, Vol. 27 (4), p. 255-295.
- D'Auria, F. et al. (1996) "OECD-NEA State of the art report on boiling water reactor stability, (Final Draft)."
- Dix, G.E. (1971) "Vapour void fractions for forced convection with subcooled boiling at low flow rates," *NEDO-10491*, General Electric Company.
- Duderstadt, J.J., Hamilton, L.J. (1976) "Nuclear Reactor Analysis," John Wiley & Sons, New York, USA.
- Fenech, H., (1981) "Heat transfer and fluid flow in nuclear systems," p.15, Pergamon Press, New York.

- Fukuda, K., Kobori, T. (1979) "Classification of two-phase flow instability by density wave oscillation model," *J. Nucl. Sci. Technol.*, Vol. 16, 95.
- Furuya, M., Inada, F., Yasuo, A. (1997) "Two-phase flow instability in a boiling natural circulation loop at relatively high pressure," *Proc. of NURETH-8*, September 30-October 4, Kyoto, Japan, Vol. 3, p. 1778-1784.
- GE, (1983) "Evaluation of Caorso scram 73", *NEDO-30112-1*, July 1983.
- Hashimoto, K. (1993) "Linear modal analysis of out-of-phase instability in boiling water reactor cores," *Ann. Nucl. Energy* 20, p. 789-797.
- Heerens, W.C. (1991) "Multi-terminal capacitor geometries: Concepts for designing sensors in a smart way," *J. Phys. E, Sci. Instrum.* 19, p 897-906.
- Hetrick, D.L. (1971) "Dynamics of Nuclear Reactors," The University of Chicago Press, Chicago, USA.
- Hidaka, M., Suzuki, H. (1990) "Experimental study on gas carry-under in down flow from two-phase mixture," *J. of Nuclear Science and Technology* 27, p. 1065-1067.
- IAEA, (1988) "Basic safety principles for nuclear power plants," IAEA safety series, No 75-INSAG-3, IAEA, Vienna.
- Inoue, A. et al. (1995) "Void-fraction distribution in a boiling water reactor fuel assembly and the evaluation of subchannel analysis codes," *Nuclear Technology* 112, p. 388-400.
- IRS, "Loss of recirculation pumps accompanied by severe power oscillations at LaSalle unit 2", 880309 IRS-887.0.
- Ishii, M. and Jones Jr., O. (1976) "Derivation and application of scaling criteria for two-phase flows," *Proc. Conf. Two-Phase Flows and Heat Transfer*, August 16-27, 1976, Istanbul, Turkey, vol. I, p. 163, Nato Advanced Study Institute.
- Ishii, M. (1977) "One dimensional drift-flux model and constitutive equations for relative motion between phases in various two-phase flow regimes," ANL-77-47, Argonne National Laboratory.
- Ishii, M. and Kataoka, I. (1984) "Scaling laws for thermalhydraulic system under single phase and two-phase natural circulation," *Nucl. Eng. Des.* 81.
- Jehee, J.N.T. et al. (1993) "Results of a study of innovative reactors," PINK report, ECN, The Netherlands.
- Kakac, S., Mayinger, F. (1977) "Two-phase Flows and Heat Transfer," vol. I, NATO Advanced study Institute, Hemisphere, Washington.
- Karve, A.A., Riswan-udding, Dorning, J.J. (1994) "On spatial Approximations for Liquid Enthalpy and Two-Phase Quality During Density-Wave Oscillations," *Trans. Am. Nucl. Soc.* 71, p. 533-535.
- Khorana, S.S. et al. (1997) "Technology basis for the ESBWR - An overview," *Proceeding of ICONE-5*, May 26-30, 1997, Nice, France, 1997.

- Kleiss, E.B.J. (1983) "On the determination of boiling water characteristics by noise analysis," PhD thesis, Delft University of Technology, Delft Universitaire Pers, Delft, The Netherlands.
- Kok, H.V., Heerens, W.C., Van der Hagen, T.H.J.J., Van Dam, H. (1995) "A new principle for designing optimal capacitive void fraction sensors applies to a rod-bundle geometry," *Measurement* 15, p. 119-131.
- Kok, H.V., Van der Hagen, T.H.J.J., Mudde, R.F. (1995) "Investigations on the thermal-hydraulics of a natural circulation cooled BWR fuel assembly," *Proc. of NURETH-7 Conference*, September 10-15, 1995, Saratoga Springs, New York, vol.4, p. 2884-2894.
- Kok, H.V., Van der Hagen, T.H.J.J. (1997) "An experimental study of the effect of void-reactivity feedback in natural circulation BWRs," *Proc. of NURETH-8 Conference*, 30 September - 4 Oktober, 1995, Kyoto, Japan, vol. 1, p. 367-374.
- Kok, H.V., Van der Hagen, T.H.J.J., Adams, B.T., Mudde, R.F. (1997) "Subchannel void-fraction measurement in a 6 by 6 rod tube bundle," *Proc. of NURETH-8 Conference*, 30 September - 4 Oktober, 1995, Kyoto, Japan, vol. 1, p. 239-246.
- Lahey, R.T. (1990) "The analysis of phase separation and phase distribution phenomena using two-fluid models," *Nucl. Eng. Des.*, 122, p. 17-40.
- Lahey, R.T., Moody, F.J. (1993) "The thermal-hydraulics of a boiling water nuclear reactor," American Nuclear Society.
- Lahey, R.T., Shiralkar, B.S., Radcliffe, D.W. and Polomik, E.E. (1972) "Out-of pile subchannel measurements in a nine-rod bundle for water at 1000 Psia," *Prog. Heat mass Transfer* 6, p. 345-363.
- Lahey, R.T., Shiralkar, B.S., Radcliffe, D.W. (1971) "Mass flux and enthalpy distribution in a rod bundle for single and two-phase flow conditions," *J. Heat Transfer*, Ser. C., 43, p. 197, Trans ASME.
- Lee, S.Y., Lee, D.W. (1991) "Linear analysis of flow instability in an open two-phase natural circulation loop," *Nucl. Eng. Des.*, 28, p. 317-330.
- Lewins, J. (1978) "Nuclear reactor kinetics and control," Pergamon press, Oxford, England.
- Lin, Y.N., Pan, C. (1994) "Non-linear analysis for a natural circulation boiling channel," *Nucl. Eng. Des.* 152, p. 349-360.
- Lützow, K., Stäck, D. (1987) "Experimentelle Untersuchungen zum Mitreißen von Dampfblasen in den Sinkschacht eines Kernheizreaktors mit Naturumlauf," *Kernenergie* 30, p. 114-117.
- Lützow, K., Wegner, D. (1987) "Ein einfaches Modell zur Berechnung des Mitreißen von Dampf in den Sinkschacht eines Kernheizreaktors," *Kernenergie* 30, p 442-449.
- Lützow, K., Wegner, D. (1990) "Verhalten der Zweiphasenströmung im oberen Umlenkbereich eines naturumlaufgekühlten Siedewasserreaktors in Integralbauweise," *Kernenergie* 33, p. 133-137.

- Maier, D., Coddington, P. (1997) "Review of wide range void correlations against an extensive database of rod bundle void measurements," *Proc. of ICONE 5*, May 26-30, 1997, Nice, France.
- McCandless, R.J. and Redding, J.R. (1989) "SBWR - Simplicity: the key to improved safety performance and economics," *Nuclear Engineering International*, November 1989.
- Meftah, K, Ruggles, A.E. (1997) "A low pressure scale model boiling water reactor with simulated void-reactivity feedback," *Proc. of NURETH-8*, September 30 - October 4, 1997, Kyoto, Japan, p. 405-412.
- Miida, J., Suda, N. (1963) "Derivation of transfer functions of natural circulation cooled boiling water reactors," JAERI Internal Report 1044.
- Natterer, F. (1982) "The mathematics of computerized tomography," Verlag B. G. Teubner, Stuttgart.
- Nylund, O. (1969) "Full-Scale Loop Studies of BHW and BWR Fuel Assemblies," ASEA Research Vol. 10, p. 63-125.
- Olsen, H. (1967) "Theoretical and experimental investigation of impedance voidmeters," Kjeller report KR-118, Kjeller Research Establishment, Norway.
- Priestley, M.B. (1981) "Spectral Analysis and Time Series," Academic Press Inc., London.
- Rao, A.S. (1993) "Simpler by design," *Atom* 430.
- Results of a comparison study of advanced reactors, A report by a working group of PINK programme I, June 1991.
- Results of a study of innovative reactors, A report by a working group of the PINK programme, July 1993.
- Rizwan-uddin (1994) "Physics of density-wave oscillations," *Proc. of Int. Conf. On New Trends in Nuclear System Thermohydraulics*, vol. 1, May 30 - June 2, 1994, Pisa, Italy, p. 195-204.
- Rizwan-uddin, Dorning, J.J. (1986) "Some nonlinear dynamics of a heated channel," *Nucl. Eng. Des.* 93, p. 1-14.
- Saha, P., Ischii, M., Zuber, N. (1971) "An experimental investigation of the thermally induced flow oscillations in two-phase systems," *Journal of heat transfer*, November 1976, p. 616-622.
- Saha, P., Zuber, N. (1974) "Point of net vapor generation and vapor void fraction in subcooled boiling," *Proc. 5th Int. Heat Transfer Conf.*, vol. 4, p. 157-179.
- Scandpower A/S, "MONA User's Manual," P.O. Box 3, N-2007 Kjeller, Norway.
- Schrock, V.E. (1969) "Radiation attenuation techniques in two-phase flow measurements," *Eleventh National ASME/AiChE Heat Transfer Conference*, Minneapolis, p. 24-35.
- Serizawa, A., Kataoka, I. (1987) "Phase distribution in two-phase flow," *Proc. ICHMT Conf. On Transfer Phenomena in Multiphase Flow*, 3, p. 327-343.

- Stekelenburg, A.J.C. (1984) "Statics and Dynamics of a Natural Circulation Cooled Boiling Water Reactor," *Phd Thesis*, Interfaculty Reactor Institute, Delft University of Technology, Delft, The Netherlands, 1994.
- Stekelenburg, A.J.C., Van der Hagen, T.H.J.J. (1994) "Low frequency dynamics of a natural circulation cooled boiling water reactor," *Int. Conf. On New Trends in Nuclear Systems Thermalhydraulics*, May 30 - June 2, 1994, Pisa, Italy, vol. 1, p. 205-217.
- Symolon, P.D. (1990) "Scaling of two-phase flow regimes in a rod bundle with freon," *Trans. Am. Nucl. Soc.* 62, p. 705-706.
- Takenaka, N., et al. (1996) "Three-dimensional void fraction measurement of two-phase flow in a rod bundle by neutron radiography," *Nuclear instruments & methods in physics research A*, 377, p. 115-118.
- Tanke, R.H.J., Japsers, J.E., Gaalman, P.A.M., Killian, D. (1991) "Application of tomography in nuclear research," *Kerntechnik* 56, No. 5.
- Todreas, N.E., Kazimi, M.S. (1990) "Nuclear Systems I - Thermal hydraulic fundamentals," Hemisphere publishing corporation, New York.
- Turso, J.A., Edwards, R.M., March-Leuba, J. (1995) "Hybrid simulation of boiling water reactor dynamics using a university research reactor," *Nuclear Technology*, vol. 110, p. 132-144.
- Van Bragt, D.D.B. (1995) "A theoretical model for coupled neutronic-thermal-hydraulic out-of-phase oscillations in Boiling Water Reactors," IRI report IRI-131-95-015.
- Van Bragt, D.D.B. (1996) "A theoretical and numerical study of the stability of a natural circulation Boiling Water reactor," IRI report IRI-131-96-006.
- Van Bragt, D.D.B., Van der Hagen, T.H.J.J. (1997) "Experimental validation of a low-dimensional physical model for coupled neutronic-thermohydraulic power oscillations in boiling water reactors," *Proc. of ICONE-5*, May 26-30, 1997, Nice, France.
- Van Bragt, D.D.B., Van der Hagen, T.H.J.J. (1998a) "Stability of natural circulation boiling water reactors: Part I - Description stability model and theoretical analysis in terms of dimensionless groups," *Nucl. Technology* 121.
- Van Bragt, D.D.B., Van der Hagen, T.H.J.J. (1998b) "Stability of natural circulation boiling water reactors: Part II - Parametric study of coupled neutronic-thermohydraulic stability," *Nucl. Technology* 121.
- Van Dam, H. (1982) "Physics of nuclear reactor safety," *Rep. Prog. Phys.* 7.
- Van Engen, W.R., Nissen, W.H.M. (1981) "Elongation measurements of fuel assemblies during irradiation in the Dodewaard boiling water reactor," *Proc. Enlarged Halden Program Group Mtg. Water Reactor Fuel Performance*, June 15-19, 1981, Hankö, Norway, HPR-286, No. 4, Institutt for Energiteknikk, OECD Halden Reactor Project.
- Van de Graaf, R., Van der Hagen, T.H.J.J., Mudde, R.F. (1994a) "Scaling laws and design aspects of a natural circulation cooled simulated boiling water reactor fuel assembly," *Nucl. Techn* 105, p. 190-200.

- Van de Graaf, R., Van der Hagen, T.H.J.J., Mudde, R.F. (1994b) "Two-Phase scaling laws for a simulated BWR assembly," *Nucl. Eng. Des.* 148, p. 455-462.
- Van de Graaf, R., Van der Hagen, T.H.J.J., Mudde, R.F. (1994c) "SIDAS: a scaled version of a natural circulation cooled BWR fuel assembly for thermal-hydraulic research," *Proc. Int. Conf. on new trends in nuclear system thermohydraulics*, May 30 - June 2, 1994, Pisa, Italy, vol I, p. 237-246.
- Van der Hagen, T.H.J.J. (1989) "Stability monitoring of a natural-circulation-cooled boiling water reactor," *PhD. Thesis*, Delft University of Technology, KEMA, Arnhem, The Netherlands, ISBN 90-353-1017-9.
- Van der Hagen, T.H.J.J., Nissen, W.H.M., Oosterkamp, W.J., Van Dam, H., Hoogenboom, J.E. (1988) "Application of noise analysis to stability determination of a natural circulation cooled BWR," *Prog. In Nuclear Energy* 21, p. 753-761.
- Van der Hagen, T.H.J.J., Stekelburg, A.J.C. (1995) "The low-power low-pressure flow resonance in a natural circulation boiling water reactor," *Proc. of NURETH-7*, September 10-15, 1995, Saratoga Springs, USA, vol. 4, p. 2785-2795.
- Van der Hagen, T.H.J.J., Pázsit, I., Thomson, O., Melkerson, B. (1994), "Methods for the determination of the in-phase and out-of phase stability characteristics of a boiling water reactor," *Nuclear Technology* 107, p. 193-214.
- Van der Hagen, T.H.J.J., Stekelenburg, A.J.C., Van Bragt, D.D.B. (1997) "Reactor experiments on Type-I and Type-II BWR stability," *Proc. of NURETH-8*, September 30-October 4, 1997, Kyoto, Japan, vol. 1, p. 397-404.
- Van der Hagen, T.H.J.J. (1988) "Experimental and theoretical evidence for a short effective fuel time constant in a boiling water reactor," *Nuclear Technology* 83, p. 171-181.
- Van der Hagen, T.H.J.J., Van der Kaa, F.J., Karuza, J., Nissen, W.H.M., Stekelenburg, A.J.C., Wouters, J.A.A. (1992) "Startup of the Dodewaard natural circulation boiling water reactor", report GKN-92-017/FY/R, GKN, Dodewaard, The Netherlands.
- Van der Hagen, T.H.J.J., Van der Kaa, F.J., Karuza, J., Nissen, W.H.M., Stekelenburg, A.J.C., Wouters, J.A.A. (1993) "Measurements at various pressures at the Dodewaard natural circulation boiling water reactor in cycle 23," report GKN-93-023/FY/R, GKN, Dodewaard, The Netherlands.
- Van der Hagen, T.H.J.J. et al. (1997) "Exploring the Dodewaard Type-I and Type-II stability; from start-up to shut-down, from stable to unstable," *Ann. Of Nuclear Energy* 24, 8, p. 659-669.
- Vijuk, R., Bruschi, H. (1988) "AP600 offers a simpler way to greater safety, operability and maintainability," *Nuclear Engineering International*, November 1988.
- Wang, F.S., Hu, L.W., Pan, C. (1994) "Thermal and stability analysis of a two-phase natural circulation loop," *Nucl. Science and Engineering* 177, p. 33-46.
- Wang, S.K., Lee, S.J., Jones Jr., O.C. and Lahey Jr., R.T. (1987) "3-D turbulence structure and phase distribution measurements in bubbly two-phase flows," *Int. J. Multiphase Flows* 3, p. 327-343.

- Wouters, J.A.A., Van der Kaa, F.J., Oppentocht, P., Nissen, W.H.M. (1992) "Data and analysis of two identical water level experiments at the Dodewaard natural circulation BWR," report 14573-TFO 92-3012, KEMA, Arnhem, The Netherlands.
- Wouters, J.A.A., Van der Kaa, F.J., Oppentocht, P., Nissen, W.H.M. (1992) "The effect of water level on the behavior of the Dodewaard natural circulation BWR," *proc. Int. Conf. On the Design and Safety of Advanced Nuclear Power Plants*, 25-29 October, 1992, Tokyo, Japan.
- Yadigaroglu, G., Maganas, A. (1995) "Equilibrium quality and mass flux distribution in BWR fuel assembly and evaluation of subchannel analysis codes," *Nuclear Technology* 122.
- Yagi, M., Mitsutake, T., Morooka, S. (1992) "Void-fraction distribution in BWR fuel assembly and evaluation of subchannel analysis codes," *Proc. Int. Sem. Subchannel Analysis*, October 30, 1992, Tokyo, Japan, The Institute of Applied Energy.
- Yano, T., Mitsutake, T., Moro-oka, S. (1997) "Simple estimation method for BWR fuel spacer performance with liquid film measurements under ambient air-water condition," *Proc. of NURETH-8*, September 30 - October 4, 1997, Kyoto, Japan.
- Zuber, N., Findlay, J.A. (1965) "Average Volumetric Concentration in Two-Phase flow Systems," *Trans. ASME. J. Heat Transfer*, Series C, 87, p. 453-468.
- Zuber, N., Staub, F.W. (1967) "An analytical investigation of the transient response of the volumetric concentration in a boiling forced-flow system," *Nuclear Science and Engineering* 30, p. 268-278.

Appendix - Void-fraction data

A1

Height 16 cm							Height 28 cm							Height 40 cm						
3.5	11.9	13.5	12.8	4.3	13.2	13.0	24.8	17.6	19.1	21.8	16.1	23.9	21.4	18.7	47.6	34.6	31.7	38.0	45.1	32.4
16.3	7.9	12.1	11.9	10.2	14.3	9.3	21.2	21.3	22.4	22.3	18.6	20.2	15.9	48.1	49.5	51.9	50.3	48.6	47.1	38.6
12.9	8.5	9.0	9.3	8.2	6.5	17.0	19.5	17.0	17.3	18.7	18.7	21.2	22.6	43.5	51.7	52.8	51.2	46.9	48.5	36.6
12.5	13.3	11.0	9.0	12.6	13.5	7.8	17.8	21.1	16.3	14.6	16.7	19.4	19.6	33.7	52.1	40.1	34.7	44.5	47.2	37.1
16.1	8.9	10.0	8.4	11.8	5.4	21.8	28.0	23.3	13.6	14.6	17.9	21.8	16.9	45.9	50.8	29.3	39.5	51.6	48.9	34.4
15.6	10.6	11.5	10.6	14.1	14.9	9.5	24.1	21.5	23.0	18.3	19.3	28.3	23.9	34.5	47.3	49.9	46.2	45.0	52.3	38.7
13.0	10.3	9.9	11.4	9.8	14.5	11.4	23.6	26.9	17.6	18.3	21.6	20.2	18.3	45.6	44.4	34.2	34.4	30.5	38.4	48.4

Height 52 cm							Height 64 cm							Height 76 cm						
31.1	30.1	36.3	31.6	35.7	45.2	41.5	30.9	39.2	35.0	36.8	37.2	40.5	29.1	35.1	38.4	36.3	31.3	42.9	46.3	32.5
41.3	40.6	40.8	41.1	36.6	41.5	31.5	41.3	45.8	42.4	43.6	45.2	47.6	35.8	43.0	53.9	51.1	48.2	49.7	55.0	35.3
33.8	42.9	40.2	38.6	39.1	37.7	39.6	33.0	45.4	42.9	42.8	42.3	43.6	37.4	41.6	49.9	44.6	43.9	47.8	45.9	34.3
27.4	40.5	30.3	36.4	35.1	40.2	30.6	29.4	43.6	38.9	39.6	40.6	42.3	39.4	29.4	52.9	49.5	46.2	42.3	57.4	43.3
32.1	42.0	24.9	30.3	39.0	42.3	38.1	44.9	44.6	29.3	36.4	42.3	48.5	36.0	38.9	46.5	33.1	36.9	44.9	50.9	46.3
36.8	44.7	36.0	42.5	37.9	44.0	31.7	39.3	47.0	39.9	43.1	44.2	50.6	43.8	42.0	50.1	48.3	50.6	51.9	56.7	44.0
37.4	40.7	33.1	31.0	30.9	45.4	15.7	26.4	46.3	44.5	33.0	34.5	45.7	21.3	41.0	43.9	44.1	37.2	42.2	42.7	25.7

A2

Height 16 cm							Height 28 cm							Height 40 cm						
18.0	19.2	17.1	14.1	18.3	20.7	28.4	37.5	31.1	33.6	28.9	33.5	34.9	47.3	18.7	47.6	34.6	31.7	38.0	45.1	32.4
19.7	20.0	19.9	20.9	16.7	24.0	14.2	39.9	40.2	36.5	42.5	34.5	37.5	26.9	48.1	49.5	51.9	50.3	48.6	47.1	38.6
16.0	27.1	19.7	23.2	23.8	22.1	22.6	34.6	40.1	35.0	40.9	31.5	40.8	38.9	43.5	51.7	52.8	51.2	46.9	48.5	36.6
17.6	19.1	17.1	21.0	19.9	18.0	9.8	31.9	36.1	32.5	31.5	35.8	34.4	38.6	33.7	52.1	40.1	34.7	44.5	47.2	37.1
20.1	28.8	18.6	14.9	22.9	20.9	17.7	39.1	40.9	26.3	30.3	37.9	40.3	29.6	45.9	50.8	29.3	39.5	51.6	48.9	34.4
26.7	21.6	23.4	20.1	23.6	29.5	19.0	30.6	38.5	41.2	38.2	35.4	47.6	41.3	34.5	47.3	49.9	46.2	45.0	52.3	38.7
23.0	16.3	17.5	21.9	18.4	24.8	27.9	50.6	37.4	33.7	29.3	28.6	33.8	33.3	45.6	44.4	34.2	34.4	30.5	38.4	48.4

Height 52 cm							Height 64 cm							Height 76 cm						
65.2	51.9	46.4	50.8	53.1	53.8	61.4	58.4	51.8	57.0	52.2	54.0	62.4	56.3	62.2	62.8	55.7	56.0	61.3	63.3	52.1
57.9	58.6	62.5	63.8	59.8	63.3	54.7	60.4	68.3	61.7	68.6	65.6	67.8	54.6	63.3	69.4	70.4	71.9	70.9	72.7	57.8
48.7	64.9	63.2	59.1	60.0	56.0	53.0	58.9	64.9	66.2	62.6	64.6	61.4	57.6	58.6	68.2	66.8	67.4	65.3	70.0	56.5
45.4	64.0	57.4	57.3	57.5	61.8	52.0	53.6	66.2	62.5	61.2	62.9	64.9	57.8	54.6	67.5	71.1	66.9	67.9	68.1	59.7
56.6	62.9	42.1	51.0	60.2	62.6	54.2	62.9	66.4	49.7	61.8	66.5	69.3	56.6	66.7	66.1	56.5	63.7	69.2	69.4	64.3
56.8	66.4	57.7	63.2	61.2	66.6	57.0	61.5	70.3	67.2	61.8	68.0	69.0	59.2	62.4	70.3	68.6	70.1	69.4	71.4	65.2
50.2	57.2	53.8	44.5	48.5	68.5	34.5	47.8	62.2	51.7	50.6	55.6	62.7	46.0	66.4	58.4	61.4	53.8	57.7	62.5	49.6

A3

Height 16 cm							Height 28 cm							Height 40 cm						
24.8	19.9	17.9	15.7	21.6	25.2	21.4	46.4	39.3	24.4	36.8	36.5	38.8	53.9	22.4	46.8	37.1	38.1	47.6	43.9	42.7
26.8	19.0	21.5	23.7	20.1	29.5	11.1	43.9	41.4	43.5	47.4	38.7	43.8	31.3	55.2	52.5	51.1	57.4	54.4	53.0	41.4
21.7	24.4	21.3	22.6	24.1	21.7	32.5	41.2	45.3	42.9	46.4	42.0	45.1	43.6	48.9	56.3	53.6	53.5	49.0	53.6	43.1
17.9	23.5	21.8	20.9	15.3	22.0	15.5	32.7	41.7	33.6	31.8	43.8	40.7	38.7	37.3	53.1	43.4	42.9	46.2	49.3	42.9
5.3	28.9	16.9	20.5	24.2	22.8	32.5	37.4	50.7	29.8	29.4	48.4	44.9	35.0	40.9	56.1	32.5	41.3	55.1	54.1	43.9
28.7	23.6	25.7	21.8	25.2	25.6	23.5	31.4	45.3	48.4	37.7	39.0	54.3	40.2	34.8	53.2	53.3	52.1	51.1	52.9	39.4
17.7	22.3	20.5	15.8	25.1	26.7	24.0	48.4	41.1	37.2	39.9	37.6	36.6	40.9	52.9	49.3	42.1	30.9	30.4	42.3	67.2
Height 52 cm							Height 64 cm							Height 76 cm						
57.1	60.2	47.1	51.5	53.2	59.3	51.4	60.9	63.6	59.3	59.9	58.9	62.2	64.3	63.5	61.5	63.5	60.9	65.3	68.0	58.3
72.8	62.7	67.7	69.8	66.4	71.6	54.9	68.5	68.1	70.6	70.2	70.6	71.2	60.7	67.2	74.2	75.3	68.6	73.7	77.5	62.8
60.6	69.0	65.3	59.3	63.6	68.4	57.2	57.5	68.8	66.3	74.4	68.2	68.0	60.3	58.9	69.8	71.9	68.2	74.0	70.7	59.1
57.5	65.4	60.3	60.1	62.3	69.8	63.1	62.3	69.3	64.2	64.8	68.4	70.3	59.7	57.1	74.1	71.5	70.0	71.5	71.1	71.9
58.2	63.4	44.3	55.0	63.7	69.5	66.5	66.0	72.0	59.7	64.1	66.6	70.7	67.1	64.4	69.4	65.7	68.5	70.3	73.9	68.5
61.4	72.0	66.2	71.1	66.4	72.1	66.4	61.4	71.1	66.9	66.0	69.5	75.7	65.6	65.4	71.3	70.4	74.6	69.5	80.2	69.8
60.8	56.4	63.2	43.9	44.5	64.9	46.2	63.0	67.4	60.5	50.6	56.0	63.9	43.0	72.0	67.0	69.0	58.4	62.1	72.9	62.3

B

Height 16 cm							Height 28 cm							Height 40 cm						
15.4	18.0	11.5	10.5	15.3	14.9	6.4	39.4	27.7	29.0	26.5	31.6	29.9	34.0	14.0	46.8	28.6	34.8	29.6	37.9	26.3
22.5	11.0	18.4	18.0	18.3	19.3	14.2	31.4	30.1	31.4	36.4	25.1	32.5	24.8	40.5	40.0	42.4	45.5	41.3	45.6	38.3
15.8	16.6	15.6	15.1	13.7	17.3	13.9	22.0	33.5	27.5	34.3	29.0	34.0	30.9	37.4	44.7	41.9	37.9	46.3	37.9	37.1
11.1	16.9	16.3	17.0	9.8	15.1	8.6	22.1	28.5	25.5	24.1	27.3	33.9	30.3	36.9	45.1	29.9	32.2	38.1	38.4	34.6
13.4	19.1	12.6	11.3	19.5	13.9	18.3	34.7	35.8	23.0	18.6	31.0	29.6	35.4	34.9	45.2	23.6	35.2	43.8	39.1	30.2
20.8	17.1	15.1	17.3	12.6	22.4	8.4	21.1	32.4	36.0	30.4	27.1	38.4	35.8	30.1	43.4	41.7	37.9	40.1	44.5	26.6
11.3	16.9	14.6	15.0	14.5	14.2	23.6	41.4	25.4	24.0	23.2	29.7	30.4	32.1	32.4	36.8	38.7	28.6	24.0	28.1	68.8
Height 52 cm							Height 64 cm							Height 76 cm						
45.5	50.9	42.1	45.1	53.5	49.5	44.7	45.4	50.9	54.1	43.2	51.2	53.9	47.3	44.4	52.2	54.1	49.7	56.2	54.6	51.8
59.3	56.0	57.8	59.3	53.3	61.6	45.1	54.9	66.0	61.8	64.1	62.3	64.9	49.8	57.2	69.9	67.9	65.7	67.1	72.8	53.2
45.5	56.1	55.6	55.1	52.4	57.7	49.3	48.1	57.9	62.6	59.5	57.9	60.0	56.1	54.1	59.4	64.8	60.4	61.1	63.7	52.4
44.0	61.2	51.6	56.2	52.3	58.7	44.8	48.1	60.2	56.6	56.0	57.1	60.6	52.1	48.0	69.4	64.0	62.8	62.1	64.8	57.5
44.2	58.5	37.9	45.6	54.0	56.5	50.4	56.7	64.8	52.6	50.0	62.1	64.4	55.3	53.7	63.7	54.7	58.2	67.5	65.7	59.5
54.0	59.4	59.7	59.7	55.8	62.2	52.4	51.6	64.5	60.8	60.5	63.5	69.3	58.6	58.3	65.5	66.5	64.8	65.3	69.9	60.3
37.0	53.3	46.6	43.6	37.9	55.0	35.3	37.2	56.1	49.4	45.7	48.2	52.4	42.7	55.9	52.2	54.4	53.8	54.9	52.6	37.8

C1

Height 16 cm							Height 28 cm							Height 40 cm						
14.0	14.8	12.5	21.1	18.7	13.6	14.9	29.8	25.5	26.2	29.6	31.4	27.2	34.9	21.1	40.5	26.8	34.6	31.8	29.7	36.4
20.2	21.6	23.2	19.7	18.2	21.0	15.5	34.3	29.7	30.7	32.7	28.1	29.1	30.8	35.1	45.3	38.5	41.5	43.8	38.4	29.5
17.9	24.2	16.9	18.7	21.1	23.0	24.3	34.7	33.2	30.1	35.3	30.3	35.4	29.9	36.2	42.4	45.0	50.2	39.5	41.0	35.3
19.0	18.0	25.5	20.7	19.8	19.7	11.7	29.9	28.6	26.1	27.8	30.2	27.0	27.4	31.6	44.4	30.6	25.6	38.6	39.6	32.5
21.3	25.6	15.8	15.6	25.5	18.9	19.7	35.7	37.4	23.2	25.9	34.0	35.2	30.8	38.8	43.0	26.9	32.6	38.1	44.7	26.5
22.2	22.8	20.1	20.4	22.2	18.8	17.7	29.1	31.8	33.1	30.9	31.2	36.9	30.2	28.5	38.8	37.0	41.3	39.7	42.2	30.1
18.6	16.9	19.8	16.7	21.8	21.5	20.9	36.2	30.2	34.3	25.1	26.2	30.2	24.1	37.0	33.1	33.0	31.1	27.8	37.3	38.7
Height 52 cm							Height 64 cm							Height 76 cm						
52.6	45.2	43.6	44.8	42.4	49.2	45.7	44.4	52.2	49.0	46.3	46.9	54.0	52.0	52.3	56.0	53.3	49.8	52.4	54.9	51.2
53.4	56.3	53.1	55.1	51.1	60.5	42.5	48.6	64.1	56.7	57.5	60.9	60.9	47.6	62.1	66.4	65.6	67.2	65.3	68.8	54.8
47.9	56.2	57.7	52.7	56.4	55.8	43.8	49.8	58.1	58.4	59.8	58.5	58.8	51.7	56.0	63.2	62.5	62.4	62.6	66.0	52.4
43.2	57.0	47.6	47.9	53.1	54.7	40.4	45.2	61.7	52.8	52.7	55.8	60.8	45.9	52.2	66.8	65.2	63.3	62.9	65.1	58.9
43.6	56.3	38.3	46.8	53.2	59.9	49.0	50.3	60.9	40.6	51.7	58.4	59.0	55.0	60.1	60.9	48.8	54.7	65.4	65.9	55.8
52.1	60.1	51.8	55.9	54.8	59.0	51.3	53.3	60.7	58.8	56.7	60.4	62.7	52.2	52.1	67.3	68.9	68.8	61.7	71.0	61.5
53.5	51.2	46.4	40.5	42.6	51.9	43.8	37.7	52.8	48.6	46.7	45.0	55.5	38.6	57.2	56.9	57.6	50.3	56.7	58.6	45.6

C2

Height 16 cm							Height 28 cm							Height 40 cm						
11.1	14.8	20.5	22.3	15.4	15.7	15.2	34.1	31.4	27.6	22.8	27.4	25.0	33.8	29.4	39.8	27.4	25.8	36.5	26.6	31.1
20.4	17.4	21.2	16.2	17.4	19.7	12.0	32.9	34.1	32.6	33.5	25.3	27.1	23.1	40.2	39.7	41.9	46.3	37.9	35.8	23.5
19.3	18.3	16.6	18.0	15.9	18.2	21.6	26.7	34.4	30.0	32.7	25.9	32.3	23.8	38.2	43.9	45.5	42.2	37.0	38.6	27.3
18.9	21.0	19.9	17.8	19.0	16.9	15.5	31.1	31.0	23.8	29.0	26.2	25.0	26.9	29.9	45.5	31.8	30.6	35.3	34.3	30.6
18.0	21.5	17.1	15.2	18.8	16.1	11.1	34.8	39.7	23.7	24.8	28.4	27.9	24.9	34.4	16.6	24.7	34.8	41.2	43.2	28.9
22.6	21.7	20.2	19.2	19.0	17.7	12.0	28.4	33.7	36.4	26.9	27.6	36.1	21.9	30.4	38.6	45.4	37.5	32.0	35.5	29.4
26.4	17.5	18.8	14.6	16.5	19.4	17.7	42.3	32.1	29.1	24.5	25.8	27.0	34.4	43.0	37.0	34.0	28.6	20.7	35.6	36.8
Height 52 cm							Height 64 cm							Height 76 cm						
51.4	45.4	43.7	43.1	44.8	48.4	48.7	48.3	57.0	51.4	46.1	44.6	52.7	48.0	54.1	56.7	54.7	47.2	47.9	52.8	39.5
58.1	57.3	53.5	57.6	47.0	56.4	37.1	56.7	62.4	59.8	59.8	57.7	57.7	43.1	58.1	68.4	64.7	66.6	61.7	65.1	49.6
45.3	59.4	56.9	52.9	53.7	49.8	42.8	52.7	61.9	61.8	60.8	54.6	55.8	51.3	55.0	63.2	65.0	57.3	58.4	60.6	47.3
46.0	60.1	48.4	43.6	48.9	46.8	39.6	48.7	64.3	51.9	50.4	50.6	55.2	47.8	52.2	67.5	61.2	57.9	57.1	61.0	47.6
47.4	60.7	36.7	42.5	48.5	54.1	43.2	55.9	62.2	42.9	50.8	56.0	61.9	47.4	55.8	63.1	51.5	56.0	61.9	62.9	55.4
52.8	59.8	53.4	57.4	51.7	57.8	47.0	54.3	63.4	58.7	57.1	60.8	60.1	51.2	56.6	67.0	65.9	63.0	61.9	67.4	54.7
63.7	53.7	52.8	38.8	39.5	48.3	23.3	48.6	57.1	54.1	48.5	38.9	49.6	43.9	63.4	60.3	55.1	50.7	47.9	50.7	34.3

C3

Height 16 cm							Height 28 cm							Height 40 cm						
6.3	21.2	11.0	18.8	11.6	12.8	12.5	30.4	30.4	19.8	25.1	23.0	26.1	34.9	26.0	40.2	33.4	26.0	30.1	23.7	27.4
21.0	18.5	21.2	17.8	19.4	16.4	12.1	40.3	35.4	34.0	27.8	25.6	19.0	19.2	47.7	49.9	42.7	40.6	34.5	31.1	21.0
23.3	20.8	20.2	14.7	14.0	11.2	17.4	34.9	38.5	31.7	39.7	23.7	26.6	27.5	43.2	48.5	44.6	44.5	35.9	35.1	24.9
14.2	23.4	19.9	16.6	14.2	15.5	8.9	29.7	37.5	28.7	23.3	25.4	18.4	17.6	34.5	48.3	30.0	28.6	34.8	28.7	23.6
19.3	26.7	14.5	12.5	16.6	12.5	15.7	36.5	39.8	21.6	18.9	28.3	25.4	21.5	34.7	47.4	25.5	35.5	39.9	36.6	22.8
24.9	21.2	18.7	16.8	18.0	17.3	13.6	31.0	40.5	35.9	30.2	24.2	30.2	13.6	37.4	46.1	44.2	38.1	37.4	35.6	22.8
22.9	14.6	22.8	13.2	16.5	15.9	18.9	45.0	34.0	30.0	25.8	26.5	25.3	27.6	43.3	39.7	38.1	28.6	20.6	22.2	41.5
Height 52 cm							Height 64 cm							Height 76 cm						
42.3	53.5	40.7	44.5	45.0	41.4	35.8	64.6	51.8	54.3	45.3	38.0	42.8	44.9	53.0	59.5	57.2	46.2	49.8	45.7	28.6
59.3	56.1	56.9	56.2	46.1	46.7	33.6	61.8	66.0	59.7	60.6	58.6	54.2	33.8	66.8	69.6	65.6	63.9	61.4	60.1	40.2
48.9	61.2	55.0	53.4	48.4	44.8	39.8	50.8	61.5	62.7	55.5	52.5	48.9	41.6	55.8	62.4	66.9	60.0	54.0	56.7	41.4
48.0	64.2	50.9	44.2	45.3	45.8	35.0	52.0	66.6	54.7	51.7	53.2	49.8	38.6	55.7	73.0	61.4	58.7	59.5	55.5	42.4
50.5	58.1	36.3	41.6	45.7	49.0	38.3	57.5	63.4	44.4	52.5	53.3	56.1	42.2	60.1	64.4	52.4	52.9	59.9	60.8	45.3
60.4	66.1	54.1	57.4	51.3	54.1	40.4	58.1	68.1	62.7	59.0	57.4	60.0	47.0	60.0	67.4	62.2	64.3	59.7	66.6	44.9
53.6	51.1	44.1	39.5	37.8	42.2	34.4	37.7	52.3	48.8	37.5	33.0	41.4	16.9	69.7	58.7	54.8	50.3	46.2	46.7	24.7

C4

Height 16 cm							Height 28 cm							Height 40 cm						
12.8	19.2	16.0	16.7	11.8	14.2	19.6	38.2	34.3	27.8	27.6	24.7	17.4	16.9	20.5	47.9	32.8	29.5	20.8	21.7	19.4
24.9	24.9	20.3	15.5	14.9	11.3	10.6	42.3	40.0	35.3	30.4	21.4	15.8	11.5	54.7	46.8	46.3	43.0	34.9	27.3	10.4
24.8	24.4	14.8	19.8	18.2	8.4	19.7	37.4	40.8	36.2	32.5	22.2	18.4	25.2	43.9	49.1	48.8	42.0	35.2	31.1	18.8
18.4	22.9	21.8	14.4	14.3	11.6	10.7	35.1	40.1	27.3	22.8	21.9	17.0	15.6	41.4	50.4	33.3	28.4	31.3	20.5	12.7
20.6	25.7	15.7	17.5	15.6	11.6	16.0	43.4	44.9	24.5	19.2	24.2	26.7	18.6	40.7	51.2	32.8	30.1	35.2	32.7	17.9
25.6	25.4	21.0	18.1	14.5	16.3	11.9	35.1	38.3	36.4	28.5	22.1	28.2	20.2	40.4	50.1	44.6	39.2	32.9	31.1	18.6
19.2	19.5	21.9	17.3	18.3	15.7	8.9	49.7	37.2	32.3	25.1	23.6	17.2	19.5	43.9	44.2	34.6	26.7	19.4	15.4	50.9
Height 52 cm							Height 64 cm							Height 76 cm						
59.6	50.9	45.3	46.5	41.6	43.1	41.6	59.8	57.3	53.4	47.4	39.0	43.8	34.6	62.2	61.2	57.3	48.3	42.0	46.5	38.2
66.3	63.2	58.5	53.2	41.8	42.4	23.9	63.0	70.1	61.2	58.6	51.6	50.1	24.5	70.4	73.9	65.9	65.9	54.9	57.7	30.0
54.0	59.3	59.5	51.3	49.6	39.2	35.0	55.4	66.1	62.7	60.3	52.8	45.6	36.7	59.8	64.0	71.2	54.8	55.0	48.6	35.0
52.8	67.5	48.9	45.2	40.0	38.4	31.3	57.2	64.2	59.7	50.5	51.4	43.2	32.0	60.6	72.6	62.1	58.2	53.4	49.0	39.9
51.2	60.4	39.9	41.2	46.4	45.9	34.3	60.7	66.6	46.6	51.6	51.2	49.7	37.7	65.9	65.0	54.5	53.8	61.3	52.7	40.3
64.1	66.1	55.4	58.8	46.2	43.6	29.8	59.1	69.5	61.0	57.4	52.8	52.5	37.1	59.5	71.1	62.7	63.2	59.4	60.6	43.1
49.9	56.5	51.7	43.8	37.8	43.5	24.1	60.4	62.9	57.6	47.1	42.5	41.5	24.4	56.8	65.4	64.5	51.7	41.4	41.9	22.7

C5

Height 16 cm							Height 28 cm							Height 40 cm						
13.3	17.0	15.4	16.5	9.0	10.4	15.6	37.1	37.6	27.2	23.6	19.8	11.6	23.0	20.8	44.5	26.3	30.8	26.4	13.4	14.7
20.9	25.9	22.2	14.4	9.1	11.6	6.0	42.7	42.3	34.0	28.8	19.3	11.1	19.6	59.4	50.8	43.4	38.4	31.3	20.3	13.3
23.6	25.5	20.3	16.7	13.9	6.4	10.9	40.5	44.3	38.0	34.5	18.8	19.0	19.8	50.5	52.7	45.6	40.7	35.2	18.8	10.2
18.6	24.7	17.8	16.5	10.3	12.9	7.5	33.7	43.5	27.1	19.5	20.5	16.9	15.1	43.6	54.1	39.7	24.7	25.2	14.5	13.9
25.8	27.1	16.9	12.3	16.2	9.9	16.7	37.1	42.6	24.7	24.1	20.9	19.7	10.5	43.9	52.2	28.6	34.1	31.9	25.6	9.9
25.5	22.5	18.8	20.6	15.5	10.6	6.2	29.0	44.7	40.6	26.2	24.4	23.8	15.9	46.2	50.2	46.1	36.6	29.8	23.8	5.5
15.0	24.2	23.7	17.4	12.8	12.2	12.7	45.2	41.2	34.3	32.0	25.2	17.1	18.1	42.1	46.2	42.8	29.2	15.9	18.2	43.7
Height 52 cm							Height 64 cm							Height 76 cm						
54.0	58.3	47.7	43.5	37.6	33.5	39.1	60.2	60.8	56.3	48.2	38.1	37.2	32.6	61.2	63.8	58.4	48.2	44.0	35.3	33.1
66.4	66.1	58.2	53.4	46.1	36.2	18.9	67.8	66.5	64.2	57.0	52.7	38.8	24.7	67.8	74.6	68.3	64.3	50.9	46.9	27.0
56.7	63.0	60.0	55.2	42.4	32.3	20.7	64.3	66.5	63.9	58.5	45.2	37.3	35.3	60.3	66.8	66.6	55.1	50.3	46.5	25.1
54.0	67.9	49.7	41.0	41.0	29.5	22.8	61.4	69.7	56.1	47.0	45.5	39.0	26.2	63.7	73.3	66.2	57.8	55.7	42.1	30.7
57.3	60.8	41.9	37.9	44.3	37.6	26.8	62.5	67.6	44.4	51.3	49.6	45.1	27.3	56.8	67.3	56.7	54.3	52.2	48.0	28.0
64.4	68.5	55.7	59.5	47.3	41.8	20.6	67.4	70.7	66.0	53.1	52.7	46.3	28.5	60.5	69.4	68.1	61.5	55.9	54.9	31.9
54.3	60.8	50.2	39.6	35.6	37.8	24.2	53.8	65.9	51.9	49.8	37.0	34.7	17.5	68.5	61.1	70.3	57.9	45.1	40.0	25.5

Summary

In the new advanced and innovative nuclear reactor designs currently being developed, natural circulation is a concept which is often used. Boiling water reactors (BWRs) are particularly suitable for the application of natural circulation to the coolant circulation flow because the boiling of water in the reactor core can be used to drive this flow completely, without the use of recirculation pumps. This makes natural circulation BWRs potentially more safe and economical. However, to prove this point all aspects of the application of natural circulation in these reactors must be considered in detail. This thesis looks at a number of these aspects using the experimental facility *DESIRE* (Delft Simulated Reactor). They can be summarized as: the void-fraction distribution in the fuel assembly, the steady-state natural circulation flow rate and the dynamic behaviour of the natural circulation flow.

The *DESIRE* facility is basically a thermodynamic loop comprising of one scaled copy of a fuel assembly of the Dodewaard nuclear reactor, a riser and a downcomer. As a scaling liquid Freon-12 is used. The scaling laws used in the design of the facility have put the emphasis on the correct scaling of the void-fraction (fraction of space occupied by vapour).

The void-fraction is essential for three important processes in a natural circulation BWR: it removes the heat from the fuel, it provides the driving force for the circulation and it affects the moderation of neutrons. To measure the void-fraction distribution in the simulated fuel assembly in *DESIRE* a gamma-transmission measurement technique is used in combination with a tomographic reconstruction procedure. This enables us to measure the void-fraction on a subchannel basis as a function of height. Measurements using this technique are compared to simple two-phase flow models. The drift-flux model using Dix's correlation gives good results. It is also shown that void drift from one subchannel to the other is negligible.

The results of the void-fraction measurements are used in the development of a steady-state model of the natural circulation flow. This model describes the driving forces and the pressure losses along the loop. It accounts for the effects of subcooled boiling and carry-under. Comparison of the model with measurements show that the model can correctly predict the flow rate for a wide range of operating conditions (at nominal pressure), which means that all the relevant physics is contained in the model. Specifically, the distribution of the pressure drops over the single-phase region and over the two-phase region of the flow is modeled correctly. This is important as it has a large effect on the dynamics of the natural circulation flow.

A frequency-domain model describing the dynamics of natural circulation BWRs is applied to DESIRE. Within the DESIRE operating range the most important mechanism for instabilities is the so-called density-wave oscillation. These can occur in a purely thermal-hydraulic system, but in a nuclear reactor an interaction with the neutronics takes place via the so-called void-reactivity feedback. To study the effect of the void-reactivity feedback on the dynamics of the natural circulation flow the model is used to calculate stability boundaries for a coupled thermal-hydraulic/neutronic system. To make comparison with measurements possible DESIRE is fitted with a simulated void-reactivity feedback. In this simulated feedback the void-fraction in DESIRE is measured, its effect on the power is calculated and the result is used to drive the power supplies of DESIRE.

Noise analysis techniques are applied to the measurements of the dynamics performed on DESIRE. They are used to determine various transfer functions of DESIRE, for example the transfer function from the power to the void-fraction or from the power to the flow rate. Comparison of these transfer functions to the transfer functions predicted by the model give good results. Measurements of the stability of the natural circulation flow in DESIRE are also compared to the model. In general there are quite large discrepancies between the measured and predicted decay-ratios (a measure for stability). The agreement between the measured and predicted oscillation frequencies is somewhat better. Suggestions are made on ways to improve the void-reactivity feedback and ways to extend the operating range of DESIRE.

Samenvatting

Het concept van natuurlijke circulatie wordt veel toegepast in de nieuwe generatie van geavanceerde en innovatieve reactorontwerpen die thans in ontwikkeling zijn. Kokendwaterreactoren zijn bij uitstek geschikt voor de toepassing van natuurlijke circulatie op de stroming van het koelmiddel door de reactorkern omdat het koken van het water in de kern direct de drijvende kracht levert voor deze circulatie, zodat koelmiddelpompen overbodig worden. Hiermee kan zowel een veiligheidswinst als een economische winst gehaald worden. Echter, om te bewijzen dat deze nieuwe reactorontwerpen werkelijk veiliger en economischer zijn moeten alle aspecten van de toepassing van natuurlijke circulatie in deze reactoren beschouwd worden. In dit proefschrift worden een aantal van deze aspecten bestudeerd met behulp van de experimentele faciliteit DESIRE. De drie hoofdonderwerpen zijn: de dampfractieverdeling in het splijtstofelement, de berekening van het circulatiedebiet en het dynamisch gedrag van de natuurlijke circulatie.

De DESIRE (*Delft Simulated Reactor*) faciliteit bestaat uit een elektrisch verhitte geschaalde kopie van een splijtstofelement van de Dodewaard reactor, een schoorsteen en een valkanaal die tezamen een gesloten lus vormen. Door deze lus stroomt de schaalvloeistof Freon-12. Met de keuze van de schalingsregels tijdens het ontwerp van de opstelling is de nadruk gelegd op de juiste schaling van de dampfractie (het volumepercentage damp van de stroming).

De vorming van damp is essentieel voor drie belangrijke processen in een natuurlijke circulatie kokendwaterreactor: het transporteert de warmte die bij de splijting vrijkomt, het zorgt voor de drijvende kracht voor de circulatie en het beïnvloedt de moderatie van neutronen. Ten behoeve van de meting van de dampfractieverdeling in het (DESIRE-) splijtstofelement wordt een gammatransmissie meettechniek gebruikt, gecombineerd met een tomografische reconstructietechniek. Dit stelt ons in staat de dampfractie te meten van elk afzonderlijk

'subchannel' in het element als functie van de hoogte. Metingen van de dampfractieverdeling worden vergeleken met eenvoudige tweefasenstromingsmodellen. Het drift-flux model gecombineerd met de correlaties van Dix geeft goede resultaten. Het wordt ook aangetoond dat het netto laterale transport van damp tussen de subchannels verwaarloosbaar is.

De resultaten van de dampfractiemetingen worden gebruikt ten behoeve van de ontwikkeling van een model van het natuurlijke circulatiedebiet. Dit model beschrijft de drijvende krachten en de drukvallen die optreden in de lus. Onderkoeld koken en 'carry-under' zijn meegenomen in het model. Vergelijking van het model met metingen geeft aan dat het model in staat is het debiet te berekenen voor een groot bereik van bedrijfstoestanden (bij nominale druk). Dit houdt in dat alle relevante fysica in het model zit. In het bijzonder is de verdeling van de drukval over het een-fase en twee-fase gebied juist gemodelleerd. Dit is van belang omdat deze verdeling een grote invloed heeft op de dynamica van de natuurlijke circulatie stroming.

Een model dat de dynamica van natuurlijke circulatie kokendwaterreactoren beschrijft is toegepast op DESIRE. Binnen het bereik van de bedrijfstoestanden van DESIRE is het belangrijkste mechanisme voor instabiliteiten de zogeheten density-wave oscillatie. Deze kan plaatsvinden in een thermohydraulisch systeem, maar in een kernreactor vindt er ook een interactie plaats met de neutronica via de zogeheten void-reactiviteits terugkoppeling. Om de invloed van de void-reactiviteits terugkoppeling op de dynamica van de natuurlijke circulatie stroming te bestuderen wordt het model gebruikt om stabiliteitsgrenzen te berekenen voor een gekoppeld thermohydraulisch/neutronisch systeem. Om deze te kunnen vergelijken met metingen is DESIRE uitgerust met een gesimuleerde void-reactiviteits terugkoppeling. Deze gesimuleerde terugkoppeling meet de dampfractie, berekent het effect op het vermogen en stuurt het resultaat naar de sturing van de elektrische voedingen van DESIRE.

Ruis-analysetechnieken worden gebruikt om verscheidene overdrachtsfuncties van DESIRE experimenteel te bepalen, bijvoorbeeld de overdrachtsfunctie van vermogen naar dampfractie of van vermogen naar het circulatiedebiet. Deze gemeten overdrachtsfuncties zijn goed vergelijkbaar met de overdrachtsfuncties die door het model worden voorspeld. Metingen van de stabiliteit van DESIRE worden ook met het model vergeleken. In het algemeen zijn er flinke verschillen tussen de gemeten en voorspelde 'decay-ratios' (een maat voor de stabiliteit). De vergelijking van de gemeten en voorspelde frequentie van de oscillatie is iets beter. Er worden aanbevelingen gedaan om de void-reactiviteits terugkoppeling te verbeteren en het bereik van de bedrijfstoestanden van DESIRE te vergroten.

Dankwoord

Eigenlijk moet op deze pagina doorschemeren niet zozeer dat ik de laatste vier jaar goed ben doorgekomen maar op welke wijze dat is gebeurd. En daarvoor spelen anderen de hoofdrol, die ik op deze plaats dan ook wil bedanken.

Ten eerste zijn dat mijn ouders die mij gedurende bijna drie decennia geholpen en gestimuleerd hebben. Dank zij hen heb ik meer dan een derde van de bij mijn geboorte toegekende levensverwachting onderwijs kunnen genieten. Bovendien hebben zij direct bijgedragen aan dit proefschrift door mij de Engelse taal op de meest efficiënte manier te laten leren.

De dank die ik verschuldigd ben aan Hugo van Dam stamt eigenlijk al van de periode van vlak voor mijn AIO-schap. De waardering die hij gaf aan mijn afstudeerwerk, maar vooral de moeite die hij genomen heeft om deze waardering te concretiseren in twee afstudeerprijzen hebben mij goed geholpen. In een iets breder kader wil ik de 'vakgroep' bedanken. In ieder geval die mensen die het mogelijk maken dat AIO's binnen deze vakgroep veel mogelijkheden krijgen om cursussen en 'summerschools' te volgen en om congressen te bezoeken. Ik heb deze altijd als zeer motiverend ervaren (dit geldt eigenlijk ook voor de RF-dagen, de DYG activiteiten enz.). Ten slotte wil ik alle andere AIO's, studenten en studentes bedanken voor de vele kleinere activiteiten, en Riny Purmer en Sonja Jobse voor de vakgroepuitjes.

Onder de vage term 'vakgroep' in de vorige alinea valt ook zeker Tim van der Hagen. Hij heeft meer dan wie ook bijgedragen aan de inhoud van dit proefschrift. Bovendien is hij de initiator van veel van de gebeurtenissen die in de vorige alinea zijn genoemd. Zijn laatste wapenfeit is het recent ingestelde koffiekwartiertje, het wordt steeds beter! Anderen aan wie ik dank verschuldigd ben zijn Rob Mudde voor zijn kennis op het gebied van de tweefasenstroming en David van Bragt voor zijn hulp bij de toepassing van zijn dynamisch model.

Zonder Jelle Schut zouden mijn experimentele activiteiten al snel tot nul zijn afgenomen. Hem wil ik vooral bedanken voor de snelheid en kwaliteit waarmee al mijn ideeën gerealiseerd en al mijn (experimentele) problemen opgelost zijn. En dan heeft hij ook nog tijd om elk jaar een IRI-wintersportvakantie te organiseren.

Zonder elektronica en computers draait niets meer tegenwoordig. Ook mijn opstelling niet en daarom ben ik dank verschuldigd aan Dick de Haas voor zijn hulp met de elektronica en aan Addy Hersman dank zij wie ik al jaren de meest bruikbare PC van de vakgroep heb.

En tenslotte het thuisfront. Deze bestaat in mijn geval uit 3+4 (ex-) studenten/AIO/werkende jongeren dank zij wie ik mij nu thuis voel in Delft. In huize 't Rietgorsje vond ik menigmaal (ongeveer 1000 maal) een maaltijd gereed als ik terugkwam van een dag hard werken op het IRI.

Curriculum vitae

Born on 26th of July, 1969, in Beloit, United States of America

1982-1985 : High school 'Jacob van Liesveld' in Hellevoetsluis.

1985-1988 : High school 'Blaise Pascal' in Spijkenisse.

1988-1993 : MSc study of applied physics at the Delft University of Technology. Graduation project performed at the department of reactor physics.

- Graduation subject: design of a capacitive measurement technique for void-fraction measurements in a rod-bundle geometry.
- Graduation reward from the faculty of applied physics.
- Graduation reward from the Netherlands Nuclear Society/KIVI kerntechniek.

1993-1997 : PhD study as described in this thesis.

